

Critical dynamics in a chain of integrator units with adaptive thresholds

Mario Martinez-Saito*

Institute of Cognitive Neuroscience,

HSE University, Russian Federation and

Department of Psychology, National University of Singapore

(Dated: January 20, 2022)

arXiv:2201.07075v2 [q-bio.NC] 19 Jan 2022

Abstract

We describe a chain of pulse-coupled excitable elements driven by a stochastic process from one end and open at the other end, as a toy model for unresolved irreducible uncertainty in a system performing inference through a hierarchical model. Threshold potentials fluctuate slowly to ensure sensitivity without being wasteful. Activity is released as power-law avalanche of pulses with density largely independent from the exogenous input form. Subthreshold activities and threshold potentials exhibit Lorentzian temporal spectra, with a power-law range determined by position in the chain. Subthreshold bistability closely resembles intracellular membrane potential measurements from other studies. We suggest that critical cortical dynamics emerge from a trade-off between metabolic power consumption and performance requirements, and that the temporal scaling patterns of electrophysiological recordings can be explained as weighted linear combinations of subthreshold activities and pulses from different hierarchy levels.

I. INTRODUCTION

Nature proliferates with complex structures spontaneously brought into being by a sustained energy flow [1]. For example, the radiant energy from the Sun causes Earth's atmospheric circulation, and sustains life on its surface. Many such structures are typically open systems involving many nonlinear interacting subunits driven by a slow exogenous force which evolve into a non-equilibrium steady state (NESS) characterized by self-organized criticality (SOC). Critical phenomena entail spatio-temporally correlated fluctuations over several orders of magnitude, power-law distributed quantities, and scaling invariance with exponents that are universal across a large class of systems. Critical phenomena are typically poised near phase transitions and occur for a narrow range of parameters, but SOC systems evolve naturally toward criticality without requiring parameter tuning. These phenomena are characterized by driven excitable media with a wide separation between the driving and relaxation temporal scales [2]. The first SOC system devised was a sandpile model [3]. Since then, many studies have put forward models suggesting that SOC explains many of the power-laws empirically found in natural phenomena. Some of these models describe earthquake seismic moments and stick-slip processes [4–6], traffic jams [7], forest fires [8],

* mmartinezsaito@gmail.com

epidemics [9], neuronal avalanches [10–12], chemical oscillators, and solar flares [13].

It has been proposed that the cerebral cortex operates near a critical regime [14] that affords optimal computational properties, viz. optimal dynamic range (e.g. quick reconfiguration in response to inputs), information transmission and information capacity [15, 16]. We conjecture that criticality in the brain ensues from three related preconditions: (1) any living creature, insofar as it comprises a regulator (nervous system) selected to enhance survival odds, must have a good enough model of its environment or external milieu [17, 18], (2) the multilayered architecture of the brain is a reflection of the multiple spatio-temporal scales of its environment, and (3) the subtle balance between performance in terms of representational accuracy and metabolic power consumption, which is characteristic of life and indispensable not to overstep the limited homeostatic range compatible with survival. We surmise that these preconditions entail the empirically observed power-law distributed neuronal avalanches [14] and temporal long-range dependencies in behavior and neural oscillations [19–23]. There are few theories that lay down organic principles of general cortical circuitry operation. Some of the most promising theories posit that the brain incorporates a generative model of the world [24, 25] instantiated as a hierarchy of layers where neural processing accomplishes inversion of the causes of sensory input [26–28]. The hierarchical nature of the brain [29] and its role in implementing contextual invariance [30] are well substantiated. Although it has been proposed that the hierarchical structure of the brain recapitulates the temporal hierarchy of its environment [31] and that SOC is a necessary attribute of any (living) system that persists as a corollary of its proclivity to resolve uncertainty through exploration [32], mechanistic accounts of how uncertainty suppression is expressed as neural dynamics are scant.

Here we put forward a link between the critical dynamics and the hierarchical architecture of the cerebral cortex, where these are manifestations of the idiosyncratic spatio-temporal scales of the world’s causal structure. We model the behavior of a hierarchical system that checks the estimated surprisal about the state of the environment at multiple temporal scales, by ignoring most of the machinery implementing its internal generative model, while bringing to focus the flow of surprisal between levels and the tolerance to surprisal determined by the threshold adaptation rule. Unlike previous studies linking avalanche dynamics of threshold units to the long range dependencies of brain dynamics [33–37], which focused on networks of recurrent connections on a complete graphs, 2D lattices, or partially connected random

network configurations, here we simply use excitable elements embedded in a single directed chain, characterized by a separation of time scales.

II. THE PERFUSIVE CASCADE MODEL

The perfusive cascade model (PC, from “diffuse through”) simulates the behavior of a good regulator [17] that incorporates a dynamical model of its environment. Let there be $l = 1..n_l$ threshold integrator units or levels, coupled in a linear daisy chain topology. The first and fastest unit, which we will denote as sensory unit, is driven by an exogenous input at discrete time steps $t = 1, \dots, n_t$. The (square of) exogenous input and unit activities can be for now roughly interpreted as a measure of uncertainty about the state of the world, that emanates from the diffusive nature of the environment. We will assume the driving input to be distributed as a discrete white standard Gaussian noise process $I \sim \mathcal{N}(0, 1)$. This is justified by the homeostatic equilibrium (in the NESS sense) in which living creatures coexist with their environment [32, 38]. This assumes that the system can track environmental states to the extent that the uncertainty of the exogenous input is on average just irreducible noise resulting from the added contribution of many sources —modeled as Gaussian random effects. In other words, the system should entertain a reasonably accurate internal representation of its environment.

The system operates in a stop-and-go manner: exogenous input drives the sensory unit only after the chain has reached quiescency. This corresponds to an infinite separation between the temporal scales of driving and relaxation [39]. At each time step or iteration t , the exogenous input drives the sensory unit ($l = 1$), and in general any unit l may receive a signal ε_{l-1} from its subordinate neighbor $l - 1$ and add to its sub-threshold activity $a_l \in \mathbf{R}$, yielding the post-pulse activity

$$\tilde{a}_l^{(t)} = a_l^{(t)} + \varepsilon_{l-1}^{(t)}. \quad (1)$$

The unit then fires and resets, or stays unchanged according to the firing rule

$$a_l^{(t+1)} = \begin{cases} \tilde{a}_l^{(t)} & \text{if } |\tilde{a}_l^{(t)}| < \theta_l^{(t)} \text{ (stay)} \\ \alpha \tilde{a}_l^{(t)} & \text{else. (fire, reset)} \end{cases} \quad (2)$$

where $\varepsilon_l \in \mathbf{R}$ is the error signal or pulse, which is propagated forward between consecutive units whenever activity reaches the threshold $\theta_l \in \mathbf{R}^+$ (for the sensory unit the error signal

is the exogenous input $\varepsilon_0 = I$). Error signals, pertaining to the subsequent iteration $t + 1$, are computed after updating the activities

$$\varepsilon_l^{(t+1)} = \begin{cases} I & \text{if } l = 0 \\ 0 & \text{if } l > 0 \text{ and } \tilde{a}_l^{(t)} < \theta_l^{(t)} \\ \tilde{a}_l^{(t)} & \text{if } l > 0 \text{ and } \tilde{a}_l^{(t)} \geq \theta_l^{(t)}. \end{cases} \quad (3)$$

As soon as it reaches the threshold, a unit transfers all its activity to its supraordinate (next) unit, in the same way an open sluice gate dumps stored water in a canal or a sōzu [40] tilts to dump water. This is also similar to the Olami-Feder-Christensen stick-slip (OFC) model of earthquake dynamics in the conservative regime, where plates undergo mechanical stress similar to how unit activities index surprisal [6]. This choice is important, because minutes details about how surprisal is transferred at the local scale determine the emergent dynamics [10, 11, 41]. However, the OFC model differs in that slipping plates spill the stored stress energy through faults shared with four neighbors in a square lattice.

The thresholds θ_l are gates that set the value of $|a_l|$ beyond which pulses are emitted. Crucially, this mimics the trade-off between metabolic power consumption and performance by setting how much surprisal can be tolerated without (costly) updating the internal representation. Note this plasticity rule is fundamentally different from Hebbian learning [35] and short-term synaptic plasticity [36, 42] rules used previously to model dynamic synaptic efficacies. Shifting relaxation thresholds has an additive, as opposed to multiplicative, effect on the excitability of units:

$$\theta_l^{(t+1)} = \begin{cases} \theta_l^{(t)}(1 - w^-) + |\tilde{a}_l^{(t)}|w^- & \text{if } |\tilde{a}_l^{(t)}| < \theta_l^{(t)} \\ \theta_l^{(t)}(1 - w^+) + |\tilde{a}_l^{(t)}|w^+ & \text{if } |\tilde{a}_l^{(t)}| \geq \theta_l^{(t)}. \end{cases} \quad (4)$$

The threshold is shifted as a function of the concurrent activities and error signals (stochastic gradient descent or delta rule), thus emulating perceptual inference and sensory adaptation with a learning rate $0 < w < 1$ (we will assume $w = w^+ = w^-$).

Sensory adaptation is modeled via threshold fluctuations. Increasing the threshold upon discharging also emulates a metabolic energy saving scheme. Decreasing the threshold of stimulated yet quiescent units is motivated by the tendency of living creatures to explore and learn—which in turn is an evolutionary imperative to prevent death in the long-term—which pushing them toward uncertain situations or the edge of failure [32, 43, 44]. In neurons, sensory adaptation induces changes in responsiveness to input [45, 46], which has the effect

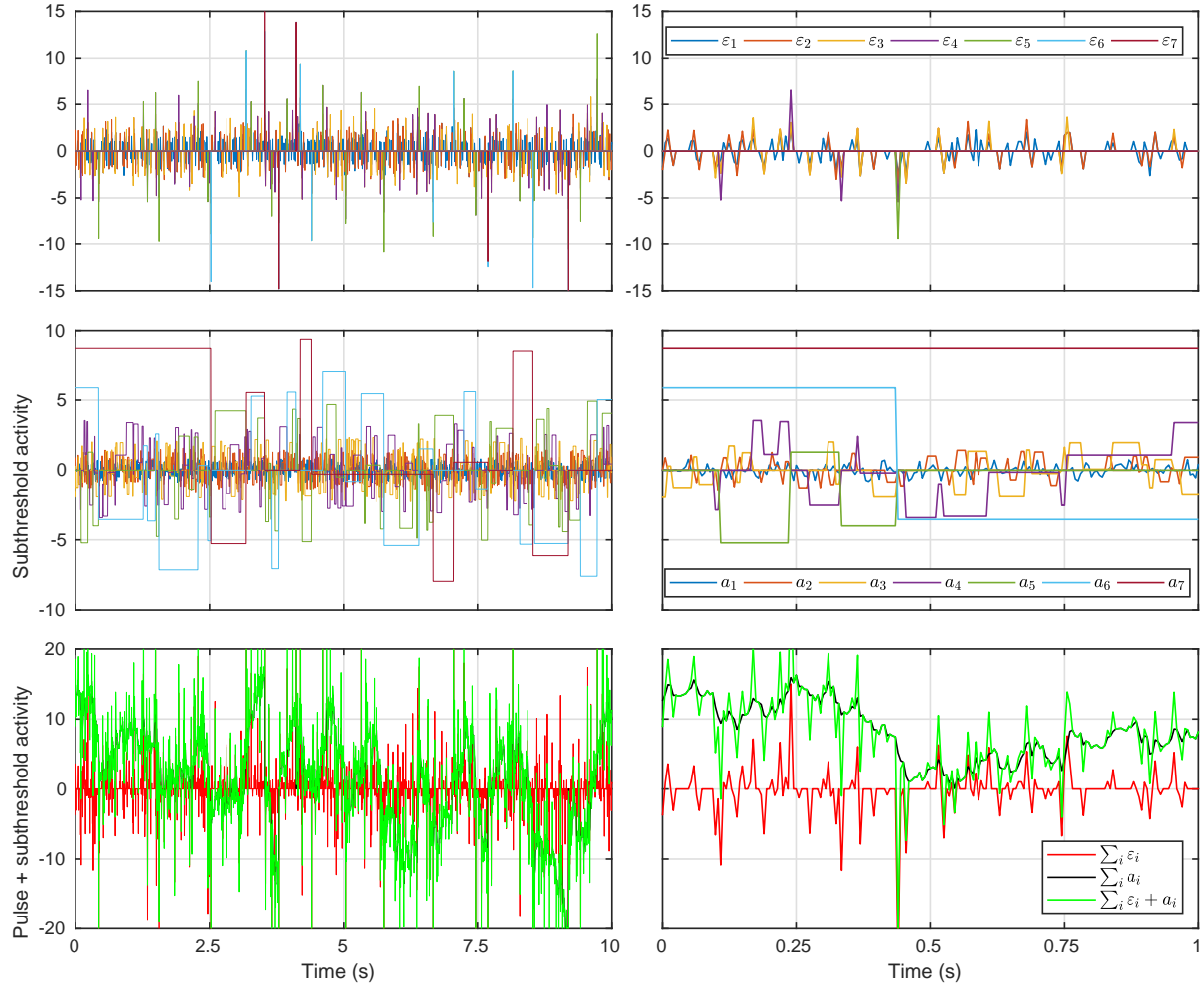


FIG. 1. Time series of pulses (top) and subthreshold activities (center) for each level $l = 1..7$, and their sum (bottom), in steady state regime. Left: interval of 2000 iterations (10 s). Right: as in left, but for 200 time steps (1 s). Exogenous driving input: white Gaussian noise. Refractory period (stepsize): $T_0 = 5$ ms.

of whitening the steady-state distribution of incoming signals. At least for some modeled causal structures, synaptic plasticity can lead to approximate Bayesian inference through Expectation-Maximization [47], and synaptic plasticity in conjunction with activity-dependent changes in the responsiveness of neurons can induce the required empirical Bayesian priors to perform Bayesian inference [48]. Importantly, the adaptability of synaptic efficacies can be interpreted as perceptual inference by assuming the generative model has been shaped by selective pressure [18] within the realm of complexity afforded by NESS structures [49].

After the cascade stops somewhere in the chain, the activities of suprathreshold nodes are

suppressed by a constant fraction $\alpha \in [0, 1]$ (we will use full suppression, $\alpha = 1$). Activity and threshold updates are triggered only by incoming signals —subthreshold quiescent units remain unchanged. A time series instantiation of pulses, activities, and their sum are shown in Fig. 1. The total absolute activity stored in the chain is $A = \sum_{l=1}^L |a_l|$, whereas $E = \sum_{l=1}^L |\varepsilon_l|$ represents the total absolute activity that is being transferred. The terminal node L has a special status because it has no node to whom relay pulses. The resetting of a_L upon relaxing or discharging is the only way to dissipate activity in the system; in other words, L is an open boundary or sink of activity.

III. MODEL PROPERTIES

Eqs. 1 – 4 constitute a stochastic discrete-time nonlinear dynamical system or map. The walk step of the sensory unit \mathcal{E}_0 is a random variable sampled from $\mathcal{N}(0, 1)$, unless otherwise stated. By symmetry, subthreshold activities evolve as one-dimensional reflected random walks. For $l > 0$, walk steps are distributed as $\mathcal{E}_l \sim |\tilde{A}_l|_{\geq \theta_l}$ restricted to $[-\infty, -\theta_l] \cup [\theta_l, \infty]$. For each level l , these random variables converge in distribution in the limit $t \rightarrow \infty$. The probability density function (density) of pulses is conditioned on activities hitting the threshold:

$$f_{\mathcal{E}_l} \equiv f_{\tilde{A}_l | |\tilde{A}_l| > \Theta_l}. \quad (5)$$

Hence, \mathcal{E}_l depends jointly on A_l , \mathcal{E}_{l-1} , and Θ_l , through the probability that unit l fires after receiving a signal from $l - 1$. The zero value is excluded from the image of \mathcal{E} , unlike for A .

A. Simulations with white Gaussian noise as exogenous driving input

Using white Gaussian noise as driving input, numerical evaluation with $L = 7$, $n_t = 9 \cdot 10^6$, and $w = .01$, we obtain the empirical distributions for A_l and Θ_l in Fig. 2. As implied by Eq. 4, $\langle \Theta_l \rangle \approx \langle |\tilde{A}_l| \rangle$. To see this, note that by definition the profiles of f_{A_l} and $f_{\mathcal{E}_l}$ result from the truncation of $f_{\tilde{A}_l}$ (Eq. 2, also Eqs. 15, 16) at Θ_l , which is close to $\langle |\tilde{A}_l| \rangle$. The sensory unit threshold is $\langle \Theta_1 \rangle = .8464$, and its mean probability of firing is $g_1 = P(\mathcal{E}_1 \neq 0) = .4251$ (see Fig. 2 and Table II). The gating or thresholding rule (Eq. 2) sets the system behavior apart from random walks by dynamically conditioning the accumulation process on the location of the threshold.

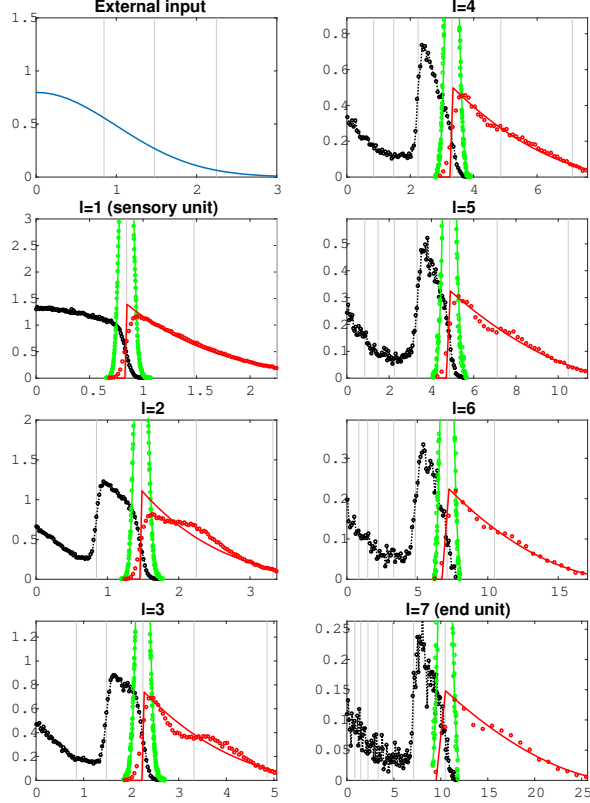


FIG. 2. Threshold (green), subthreshold activity (black), and pulse (red) empirical distributions for $l = 1..7$, and white Gaussian noise exogenous input (blue). All distributions are symmetric with respect to the origin. Only the positive half of the (symmetric) densities is shown. The subthreshold activity A_l^+ is shown excluding the rest state $A_l = 0$, instead of the original A_l ; their densities are related by $f_{A_l} = g_l \delta(0) + (1 - g_l) f_{A_l^+}$. $P(A_l = 0) = g_l$ are included in Table II. Vertical gray lines indicate the location of $\langle \Theta_l \rangle$. Number of iterations $n_t = 9 \cdot 10^6$.

The positive half of subthreshold activity $|A_l^+|$ densities is bimodal, with one peak at zero and other close to $\langle \Theta_{l-1} \rangle$. The pulse \mathcal{E}_l densities are the smoothly truncated tails of \tilde{A}_l , roughly similar to the generalized Pareto distribution (Appendix F). In the vicinity of the origin, A_l^+ is well approximated by a constant slope graph, as in systems governed by continuous diffusion with resetting beyond a fixed threshold [50]. The stationary densities f_{Θ_l} , $f_{\tilde{A}_l}$ and $f_{\mathcal{E}_l}$ for each unit $l > 1$ are scaled by $k_l \approx 1.5$ with respect to the preceding unit (Fig. 2, Table I). The scaling factors k_l are related to the properties of one-dimensional driftless random walks. By construction, consecutive unit thresholds cannot be scaled by a factor larger than 2: the fluctuating thresholds are attracted to the expected value of

TABLE I. Numerically estimated between-level scaling factors, gains and discharge rates. The gain is the probability of discharging after receiving a signal $g_l \equiv P(\mathcal{E}_l \neq 0 | \mathcal{E}_{l-1} \neq 0)$, with $P(\mathcal{E}_0 \neq 0) = 1$ (only the sensory unit is driven at each iteration; note that unit l discharging is tantamount to $\mathcal{E}_l \neq 0$). The last digit is the least significant; the expected variability in round brackets is in s.e. units. Probabilities are modeled as binomial proportions and their standard uncertainties are estimated using a normal approximation. Burn-in draws (10^5) were discarded; all values are averaged across $9 \cdot 10^6$ time steps. Only significant digits are displayed. *For convenience, $\langle \Theta_0 \rangle$ is arbitrarily set to 1, so this cell value equals $\langle \Theta_1 \rangle$. g_l : gain; $200\nu_l$: firing rate of unit l , thus roughly assuming a 200Hz firing rate for the sensory unit.

l	$k_l \equiv \frac{\langle \Theta_l \rangle}{\langle \Theta_{l-1} \rangle}$	$k_{\theta,l} \equiv \frac{\langle \Theta_l \rangle}{\langle \mathcal{E}_{l-1} \rangle}$	$k_{\varepsilon,l} \equiv \frac{\langle \mathcal{E}_l \rangle}{\langle \Theta_l \rangle}$	g_l	$200\nu_l$
1	0.8470*	1.0615	1.7100	.4252	85
2	1.7404	1.0178	1.5044	.4503	38
3	1.5241	1.0131	1.4605	.4602	17
4	1.4748	1.0119	1.4482	.4697	8.2
5	1.4660	1.0123	1.4570	.4620	3.7
6	1.4749	1.0123	1.4494	.4672	1.7
7	1.4662	1.0116	1.4552	.461	0.8

post-pulse activities $\langle \tilde{A}_l \rangle$, which cannot be larger than $2\langle \Theta_{l-1} \rangle = 2\langle \tilde{A}_{l-1} \rangle$ (cf. section). On the other hand, a subsequent unit has larger threshold than a preceding unit because the sequence of accumulating inputs is a (diffusive) random walk that eventually reaches any (finite) threshold $\theta_l > \theta_{l-1}$ almost surely. Hence, $k_l \in [1, 2]$.

Table I displays, for each level, numerical estimates of scaling factors between successive levels between average thresholds and error signals, the firing rate $\nu_l = P(\mathcal{E}_l \neq 0)$, and the gain or probability of firing after an input

$$g_l \equiv 1 - \int_0^{\Theta_l} f_{\tilde{A}_l} = 1 - F_{\tilde{A}_l}(\Theta_l) = P(\tilde{A}_l > \Theta_l), \quad (6)$$

where $F_{\tilde{A}_l}$ is the cumulative distribution function of A_l . The firing frequency ν_l is the accumulated product of the current and subordinate levels' gains

$$\nu_l = \prod_{i=1}^l g_i. \quad (7)$$

We assumed a relative refractory period of $T_0 = 5\text{ms}$ (or equivalently a sensory input rate of $\nu_0 = 200\text{Hz}$), which is typical of neurons [51] and in neural network simulations [52]; this is also a rough estimate of the firing rate expected at each level under continuous exogenous driving. See Table II for estimates of average thresholds and subthreshold activities for each level.

For $\langle\Theta_1\rangle = .8464$ (Table II), the probability that the sensory unit discharges at any time $g_1 = P(\mathcal{E}_1 \neq 0)$ is lower bounded by the firing rate of a memoryless process where subthreshold activities are reset at every iteration (white Gaussian noise activity, $P(\tilde{A}_{\mathcal{N}(0,1)} = 0) = .3973$), and upper bounded by the firing rate of a process where the size of time step approaches zero (Wiener process, $P(\tilde{A}_{B(t)} = 0) = .5158$). This is because, conditioned on not having reached the threshold, the subthreshold activity $a_1^{(t)}$ follows a Gaussian random walk with unit variance within $[-\theta_1, \theta_1]$, so the quadratic mean of its translation distance after t steps is distributed normally with variance t . This means that the variance of the stochastic process $A_1^{(t)}$ is larger than for white Gaussian noise, but smaller than for a Wiener process (see appendix B). Therefore, the refractory period explains that the gain is lower than if each unit behaved as a continuous-time accumulator —a “Brownian neuron” (Appendix B).

The addition of subthreshold activity A_l to \mathcal{E}_{l-1} causes a threshold expansion: for the sensory unit $\langle\Theta_1\rangle > \langle|\mathcal{E}_0|\rangle = \langle|\mathcal{N}(0,1)|\rangle = \sqrt{2/\pi} = .7979$, which evinces that $\langle\Theta_1\rangle$ is larger than what it would be if A_1 were memoryless (i.e. if it were reset to zero after each iteration). Leftover subthreshold activity leads to $k_{\theta,l} \equiv \frac{\langle\Theta_l\rangle}{\langle|\mathcal{E}_{l-1}|\rangle} > 1$ because the addition of random sign signals diffuses bilaterally toward the thresholds (eventually triggering a discharge almost surely, and thus perfusing or diffusing through to the following level). Numerical simulations show that $\frac{\langle\Theta_l\rangle}{\langle|\mathcal{E}_{l-1}|\rangle} = 1.000$ if activities are reset after each iteration. But even for memoryless units, if we let the threshold adapt, the gain of an element driven by white Gaussian noise $P(\tilde{A}_{\mathcal{N}(0,1)} = 0)$ (or most stationary process) would be less than .5. The reason lies in the asymmetry of $f_{|\mathcal{E}_l|}$. The probability of firing is the proportion of post-pulse activities lying above threshold; therefore a gain of .5 corresponds to a threshold equal to the *median* of the pulse $\text{md}(\mathcal{E}_l)$. However, the statistic that governs threshold location according to Eq. 4 is the mean of the pulse $\langle|\mathcal{E}_l|\rangle$, and $\langle|\mathcal{E}_l|\rangle > \text{md}|\mathcal{E}_l|$ because $|\mathcal{E}_l|$ is right-skewed. In summary, $\frac{\langle\Theta_l\rangle}{\langle|\mathcal{E}_{l-1}|\rangle} > 1$ is caused by the diffusive effect of leftover subthreshold activity, and gains are less than .5 because $f_{|\mathcal{E}_l|}$ is right-skewed.

B. Spectral densities in the steady state

Θ_l , A_l and \mathcal{E}_l are stochastic processes indexed by t . From Eq. 4, it follows that Θ_l is characterized by an autoregressive model of order one or AR(1) with constant parameter $w\langle\Theta_l\rangle$, regressor parameter $1-w$ and white noise $w(|\tilde{a}_l^{(t)}| - \langle\Theta_l\rangle)$ with variance $w^2 \text{var} |\tilde{A}|$. This can also be construed (in the limit $T_0 \rightarrow 0$) as a continuous-time Ornstein-Uhlenbeck process (OUP) with mean $\langle\Theta_l\rangle$, mean reversal term $-w$, and the same noise variance $w^2 \text{var} |\tilde{A}|$ (see appendix C):

$$S_{\theta,\theta}(\nu|l) \approx \text{var} |\tilde{A}| \frac{T_l \gamma_\theta^2}{\gamma_\theta^2 + \nu^2}, \quad (8)$$

which is a Lorentzian function, with maximum $S_{\theta,\theta}(0) = T_l \text{var} |\tilde{A}|$ at $\nu = 0$ and corner frequency $\gamma_\theta = \frac{w}{2\pi T_l}$. The corner frequencies for each unit firing period are shown in Table III. The T_l , for each level $l = 1..7$, correspond to the discharge rate of immediately preceding units $T_l = \nu_{l-1}^{-1}$, with $\nu_0^{-1} = T_0$. The power spectral density estimate of threshold numerical time series $\theta_l^{(t)}$ agrees with the spectral function of its corresponding AR(1) process (Fig. 3). The discrepancies at the high and low frequency ends are caused by the power spectrum estimation method bias (i.e. spectral leakage, see appendix C). Power spectra coincide for frequencies above $\approx 0.5\text{Hz}$ (assuming a sampling rate of $T_0 = 5\text{ms}$) for all units except for the sensory unit (see blown up inset of Fig. 3), which is slightly larger; this difference is due to the sensory unit being the only one that receives arbitrarily small input signals, as can be seen in Fig. 2. The corner frequencies $\nu_{\theta,l}$ are smaller than $\approx 0.3\text{Hz}$ (Table III), which indicates for each l the largest frequency at which the dynamics departs from white noise.

The pulses derive their temporal structure from the exogenous input: the auto-correlation of discharges for any unit is directly inherited from the auto-correlation of its input. Therefore, with white noise as exogenous input, \mathcal{E}_l also becomes white noise, albeit in general it is not distributed as the input. This is reflected in the flat PSD of ε_l (Fig. 4), which coincides with the PSD of the (standard Gaussian process) input distribution \mathcal{E}_0 . Pulses from all units bear the same power because, as one ascends the hierarchy of units, increasing signal activity is offset by sparser firing. The sum of pulses from all units has larger power for low frequencies because the pulses are pairwise coherent and in phase only at low frequencies (see Fig. 18), which implies that the PSD of the sum of pulses is larger than the sum of their PSDs only at low frequencies.

The dynamics of the activity variables $a_l^{(t)}$ is defined by Eq. 2, which describes a random

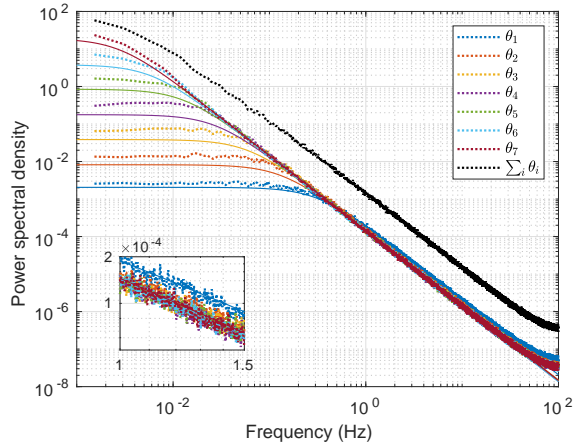


FIG. 3. Power spectral density estimate of the numerical time series of threshold fluctuations $\theta_l^{(t)}$ (dotted curves), and their corresponding AR(1) expressions (solid curves), for each level $l = 1..7$, and for their sum $\sum_{l=1}^7 \theta_l^{(t)}$. Sampling rate $T_0 = 5\text{ms}$. Number of iterations $n_t = 9 \cdot 10^6$. Estimated using Welch's method with Hamming windows of size $9 \cdot 10^4$ and 50% overlap.

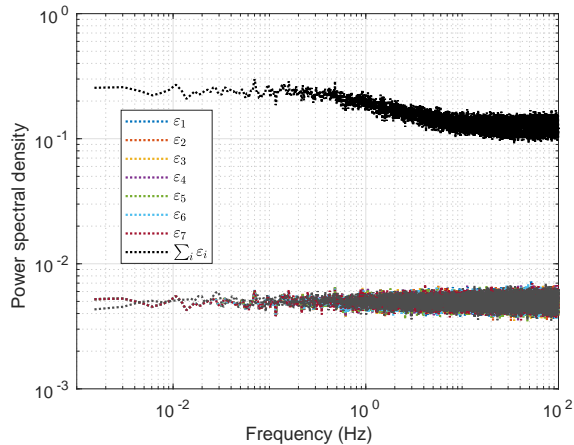


FIG. 4. Power spectral density estimate of the numerical time series of pulses $\varepsilon_l^{(t)}$. The PSD for each $\varepsilon_i^{(t)}$ is equal to that of the exogenous input, which is white Gaussian noise with unit variance, $S_{\varepsilon_0, \varepsilon_0} = T_0 = 5\text{ms}$. Note that white noise signals are not affected by spectral leakage. Estimation parameters as in Fig. 3.

walk with stationary and independent increments distributed as \mathcal{E}_l (Fig. 2, in red) that resets to zero upon leaving $[-\theta_l, \theta_l]$. Crucially, the stochastic resetting implicit in Eq. 2 alone brings about a NESS (with non-Gaussian fluctuations) because the combination of reset and diffusion constitutes a globally transition probability current-carrying loop between any

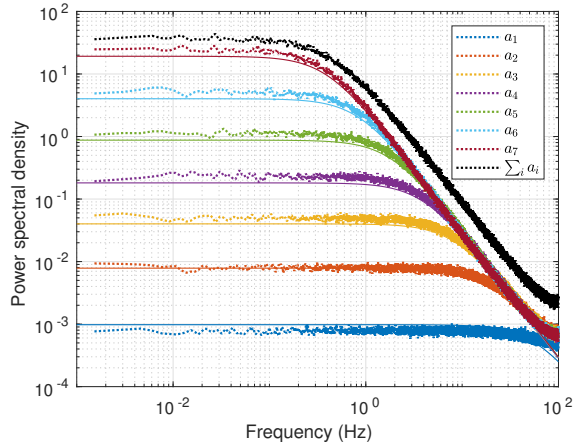


FIG. 5. Power spectral density estimate of the numerical time series of activities $a_l^{(t)}$. Estimation parameters as in Fig. 3.

activity value outside $[-\theta_l, \theta_l]$ and zero (the reset point), thus violating detailed balance [50]. This feature endows the system with complex and critical dynamics.

Although at first sight subthreshold activities behave unlike thresholds, it turns out that their covariances and power spectra do. As done with thresholds, we can use a continuous-time approximation, whereby in the limit $T_0 \rightarrow 0$ they are effectively rendered an instance of OUP, where the mean-reverting force replaces the zero-resetting rule. Knowing the probability that a unit resets at time t since the last reset is the hitting time distribution $f_{\tau_{\pm\theta}}(t)$ (appendix A), we can estimate the covariance function $a_l^{(t)}$ by taking the limit $T_0 \rightarrow 0$ and making other suitable approximations, and thence derive the PSD by Fourier transformation (see appendix C):

$$S_{a,a}(\nu|l) \approx \frac{\sigma_{\varepsilon_0}^2 \theta_l^2 (1 - g_l)^2 \gamma_a}{\pi(\nu^2 + \gamma_a^2)}, \quad (9)$$

where $\gamma_a = (2\pi \frac{3}{4} \theta_l^2 T_0)^{-1}$ is the corner frequency and the maximum is $S_{a,a}(0) = 2\sigma_{\varepsilon_0}^2 T_0 (\frac{3}{4})^2 \theta_l^4$. Importantly, the frequency spectrum of activities time series bears the same Lorentzian shape as thresholds do, so —barring approximations— activity resetting is effectively a restoring force of the same sort of the OUP.

The cross-power spectral density plot of pulses versus activities (Fig. 6) shows that some power is linearly transferred from pulses to subthreshold activities (cells above the diagonal, blue), and that the cross-spectral phase is positive, which evinces a delay of subthreshold activity phase with respect to preceding pulses (cells above the main diagonal, green), which

is a reflection of the causal effect of pulses on subthreshold activities of subsequent units. The phase response is nonlinear outside the main diagonal. Negative cross-spectral phases in and below the main diagonal evince the reversal of causality: subthreshold activities causally induce pulses in units of the same or higher levels.

Unlike pulses, subthreshold activities are pair-wise incoherent over the whole frequency range (section C, cf. Figs. 18 and 19). This reflects that subthreshold activities exert a negligible effect on firing probabilities compared to pulses. In the steady state, the probability of firing given the preceding unit pulse $P(\mathcal{E}_l \neq 0 \mid \varepsilon_{l-1})$ is a monotonic increasing function of $|\varepsilon_{l-1}|$ because $P(\mathcal{E}_l \neq 0) = P(|A_l + \mathcal{E}_{l-1}| > \Theta_l)$, so ε_{l-1} is the amount of activity that the density of $|A_l + \mathcal{E}_{l-1}|$ is shifted positively, thus increasing the probability measure that exceeds the threshold Θ_l . In opposition, the probability of firing given the current unit subthreshold activity $P(\mathcal{E}_l \neq 0 \mid A_l)$ is approximately independent of A_l (Fig. 10), which follows from the unbiasedness of Brownian fluctuations.

In summary, subthreshold activity and threshold dynamics can be modeled as continuous OUP or its associated discrete AR(1) model. These processes can be construed as a weighted combination of the white noise injected at the sensory unit and a mean-reverting process effected by the adaptive threshold and subthreshold activity gating rules. Although activity power spectra plateau at low frequencies, the corner frequencies marking the end of the plateau at different levels span two orders of magnitude (Table III). Their temporal covariance functions are exponentially decaying, with a decay constant that at each level is proportional to the discharge period (Appendix C). In general, integrator unit dynamics can be construed as a Markov renewal process with discrete discharge times t , inter-event times ν_{l-1} , subthreshold activity as a continuously valued state A_l , and jumps \mathcal{E}_{l-1} (Appendix C). The inter-event times are distributed as the first hit time (of subthreshold activity with respect to its corresponding threshold), which has an exponentially decaying tail (Appendix C, Eqs. B3, B5), and the PSD of subthreshold activities (Eq. 9) and thresholds (Eq. 8) bear a Lorentzian form. This is analogous to shot noise, a process that explains flicker noise in electronic devices where the sum of events in a Poisson process —with exponentially decaying inter-event times— has a PSD with Lorentzian form [53]. Although it is also possible to construct fractal shot noise or fractal Markov renewal models that display a power law PSD with exponents in $[0, 2]$ over an arbitrarily wide range of frequencies by setting power law decaying inter-event times [54], in our system PSD are always Lorentzian-like, and power

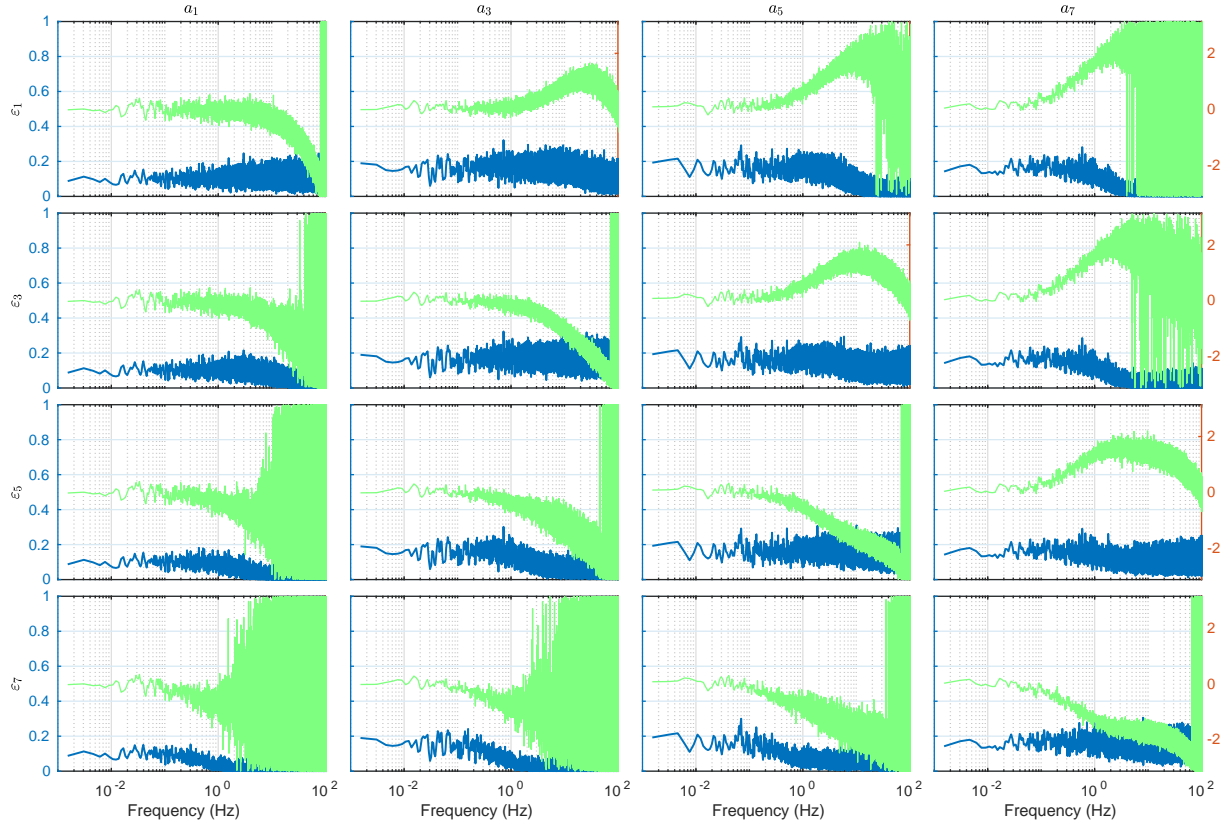


FIG. 6. Cross-spectral phase (green, in radians) and magnitude-squared coherence (blue) pair-wise estimates between pulses $\varepsilon_l^{(t)}$ (in rows) and subthreshold activities $a_l^{(t)}$ (in columns) for $l = 1, 3, 5, 7$. Cells above the main diagonal are populated by causal interactions pulse-subthreshold activity, i.e. combinations of $\varepsilon_m^{(t)}$ and $a_n^{(t)}$ with $m < n$, whereas cells in or below the diagonal display causality in the opposite direction. The smeared bands of some phase plots indicate that estimation is unreliable due to low or null coherence. Estimation parameters as in Fig. 3.

law behavior of subthreshold activities occurs for a restricted frequency span above a value $\gamma_{a,l}$ (corner frequency) that depends on the level l . Ultimately, the power-law frequency range of subthreshold activities stems from the intermittent integration of the driving input at each level. This is similar to how power law PSD noise can be generated by fractionally integrating white noise [55, 56].

C. Pulse avalanche power laws

As activities (or their square, as we will see in the next section) percolate through the chain, pulses become rarer by a factor of g_l and larger by a factor of k_l at each level l . The shape of the densities \mathcal{E}_l , Θ_l , A_l evinces some degree of self-similarity across levels (Fig. 2). If we assume self-similarity, we can approximate the pulse densities (probability density functions) at successive levels as

$$f_{\mathcal{E}_{l-1}}(x) = k_l f_{\mathcal{E}_l}(k_l x), \quad (10)$$

where we made the change of variables $\mathcal{E}_l = k_l \mathcal{E}_{l-1}$, which induces a factor k_l to ensure probabilities sum to 1. Likewise for the frequency-weighted pulse size densities (defined as $\nu_{\mathcal{E}_l} \equiv \nu_l f_{|\mathcal{E}_l|}$): $\nu_{\mathcal{E}_{l-1}}(x) = \frac{k_l}{g_l} \nu_{\mathcal{E}_l}(k_l x)$. The area under $\nu_{\mathcal{E}_l}$ for a range of pulse sizes can be interpreted as the frequency at which unit l emits pulses within that range. Analogously to Eq. 10, subthreshold activities and threshold size densities are scaled by k_l :

$$f_{\Theta_{l-1}}(x) = k_l f_{\Theta_l}(k_l x), \quad (11)$$

$$f_{A_{l-1}}(x) = k_l f_{A_l}(k_l x). \quad (12)$$

In general, we might be interested in the mixture distribution of pulses, which can be expressed as the mixture density

$$f_{\mathcal{E}_{mix}}(x) \propto \sum_{i=1}^{n_l} \nu_i f_{|\mathcal{E}_i|}(x) = \sum_{i=1}^{n_l} \nu_{\mathcal{E}_i}(x) \propto x^{-3}, \quad (13)$$

where the contribution of each level would be proportional to its discharge rate ν_l , and the r.h.s. becomes a density by dividing by $\sum_{i=1}^{n_l} \nu_i$. The envelope of the mixture density of pulse sizes (absolute values) rolls off as $f_{|\mathcal{E}|}(x) \propto x^{-3}$ (Fig. 7) because $\nu_l \propto l^{-2}$ holds in good approximation (Table I) —the reason for this will be examined in the next section—, and $\langle |\mathcal{E}_l| \rangle \propto l$, which entails that densities are spread over larger domains in inverse proportion to l as expressed in Eq. 10). In particular, the exponent 3 comes from —in logarithmic scale— adding the exponents -2 and -1 that describe respectively how ν_l and $f_{\mathcal{E}_l}$ are scaled down with respect to l (cf. Eq. 13), and dividing by the expected pulse size scaling exponent 1.

If all the activity pulses in the chain that are triggered by each driving input were added together instead of weighing pulse sizes at each level by their frequency, then the sum of

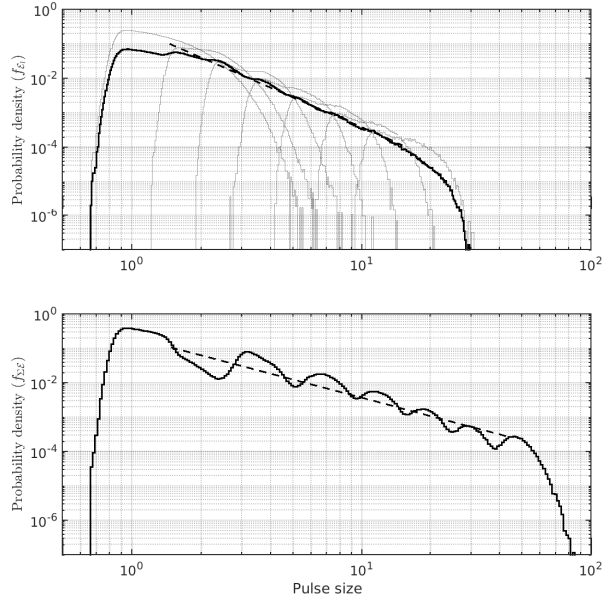


FIG. 7. Density estimates of pulse sizes (absolute values) for $n_l = 7$ levels. Upper: mixture density $f_{\mathcal{E}_{mix}}$ (black), and pulse size density $f_{\mathcal{E}_l}$ for each level $l = 1 \dots 7$ (light grey). Lower: density of the sum of pulse sizes $f_{\Sigma\mathcal{E}}$. Slopes (dashed line) were fitted in the least squares sense in a range that excluded finite-size effects: $[\langle|\mathcal{E}_1|\rangle, \langle|\mathcal{E}_7|\rangle]$ for $f_{\mathcal{E}_{mix}}$ and $[\langle|\mathcal{E}_1|\rangle, \sum_{i=1}^7 \langle|\mathcal{E}_i|\rangle]$ for $f_{\Sigma\mathcal{E}}$.

pulse densities (weighted by their frequencies) $f_{\Sigma\mathcal{E}}$ would be the relevant random variable. Using the correspondence between the sum of random variables and convolution of their densities, we get

$$f_{\Sigma\mathcal{E}}(x) = \nu_{\mathcal{E}_1}(x) * \dots * \nu_{\mathcal{E}_l}(x) \propto x^{-2}, \quad (14)$$

where the decay exponent is obtained similarly to above by noting that $\langle|\mathcal{E}_1|\rangle + \dots + \langle|\mathcal{E}_l|\rangle \propto \sum_l l \propto l^2$, where we have used Eq. 10. We have not specified up to this point whether we are considering the sum of the absolute value of pulses or the absolute value of the sum of pulses because they coincide, i.e. $\langle|\sum_0^7 \mathcal{E}_l|\rangle = \sum_0^7 k^l \langle|\mathcal{E}_0|\rangle = \frac{k^8-1}{k-1} \langle|\mathcal{E}_0|\rangle$. This is because, by construction (cf. Eqs. 2, 3, Fig. 10), incoming pulses cannot trigger outgoing pulses of opposite sign.

As shown in Fig. 7, the mixture and sum density exponents in the scaling range are in rough agreement with the numerical estimates of -2.90 and -1.77. The log-periodic oscillations evinced by the densities in Fig. 7 are reminiscent of discrete scale invariance [57]. For the mixture density, the logarithmic periods are $\Omega = k_l \approx 1.46$. As we will see later, $k_l \rightarrow k_*$

holds for large l ; thus from the properties of geometric series $\Omega = \frac{k_*^l - 1}{k_*^{l-1} - 1} \approx k_*$ becomes independent of l and $f_{\mathcal{E}}$ indeed displays discrete scale invariance with the same logarithmic period.

IV. STEADY STATE: FLOWS AND CONSERVATION

A. Diffusion and gating

Activity dynamics can be construed as an iterative process consisting of two alternating stages: diffusion and gating. The presence of flows —the signals transferring energy between units— implies that the system is in NESS. This precludes the existence of a Gibbs algorithm specifying a stationary distribution. Thus, the averages are not equilibrium averages, but steady state averages, which are less informative of the system dynamics. Nonetheless, in the steady state, Θ_l converges in distribution to a Gaussian $f_{\Theta_l} \xrightarrow{p} \mathcal{N}(\langle \Theta_l \rangle, \sigma_{\Theta_l})$ (cf. Fig. 2); this was confirmed for a small enough learning rate ($w < .1$) in simulations. Because the dynamics of A_l and Θ_l are interlocked, working out their stationary distributions requires calculating their joint distribution. Note that $f_{\tilde{A}_l}$, f_{A_l} , and $f_{\mathcal{E}_l}$ are conditioned on the thresholds $\Theta_{\leq l} = \Theta_1, \dots, \Theta_l$. The stationary distribution of activities f_{A_l} has no closed-form expression, but it can be computed as the (infinite) sum over t of the subthreshold activities resulting from t iterations after the last discharge, weighted by the probability of *not* having fired for t time steps (which is a function of Θ_l ; see Eq. A2).

The stationary distributions of A_l and \mathcal{E}_l are interlocked and recursively defined by the composition of an addition (with an incoming pulse) and a probability density truncation operation (the gating of activity caused by the thresholding rule):

$$f_{A_l}(x) = g_l \delta(x) + (1 - g_l) B_{\Theta_l} f_{\tilde{A}_l}(x) = g_l \delta(x) + f_{\tilde{A}_l | \tilde{A}_l < \Theta_l}(x) \quad (15)$$

$$f_{\mathcal{E}_l}(x) = \frac{1}{g_l} T_{\Theta_l} f_{\tilde{A}_l}(x) = \frac{1}{g_l} f_{\tilde{A}_l | \tilde{A}_l \geq \Theta_l}(x), \quad (16)$$

where δ is the Dirac delta, and $B_{\Theta} f$ and $T_{\Theta} f$ are respectively the normalized body and tails of a two-sided truncated f distribution, with support $[-\theta, \theta]$ and $[-\infty, -\theta] \cup [\theta, \infty]$ (notice that Θ is a random variable). The $g_l \delta(x)$ term indicates that the probability that the subthreshold activity A_l equals zero is $f_{A_l}(0) = g_l$. The learning rate w governs the variance of Θ —as $w \rightarrow 0$, the variance vanishes—, thereby determining the smoothness of f_{A_l} and

$f_{\mathcal{E}_i}$. Stationarity mandates that $f_{\tilde{A}_i}$ be invariant under the composition of convolution with $f_{\mathcal{E}_{i-1}}$ and truncation at Θ_i (Eq. 15).

B. Conservation of squared activity (energy)

The accumulating sequence of exogenous inputs can be construed as a one-dimensional activity random walk. In a continuum approximation, and in the absence of gating, the density of diffusing activity ϕ is specified by the heat equation $\frac{\partial \phi}{\partial t} = D \frac{\partial^2 \phi}{\partial x^2}$ with diffusion constant $D = \frac{\sigma_{\mathcal{E}_0}^2}{2T_0}$ (with $\sigma_{\mathcal{E}_0}^2 \equiv \text{var } \mathcal{E}_0 = \langle \mathcal{E}_0^2 \rangle$). Its fundamental solution is the heat kernel, which describes the evolution of a "unit" of activity placed at time $t = 0$ at $x = 0$ diffusing in $(-\infty, \infty)$ without boundary conditions (Green's function number X00): a time-varying Gaussian function with zero mean and variance $2Dt$, which is also the mean squared displacement $\text{MSD} = \langle (x(t) - 0)^2 \rangle$ in one dimension. The entropy of an exogenous input with Gaussian density is $\frac{1}{2}(\log 2\pi\sigma^2 + 1)$ (where σ^2 is variance), so the entropy of the heat kernel with $\text{MSD} = 2Dt$ that describes diffusion of activity resulting from accumulating input is $\frac{1}{2}(\log 4\pi Dt + 1) \sim \frac{1}{2} \log t$, and its derivative or entropy production rate is $\dot{S} \sim \frac{1}{2t}$. Since the inflow of exogenous input is proportional to time $\sim t$, and entropy is an extensive variable (proportional to input activity) it ensues that the entropy production rate of the system is a constant, as is characteristic of a steady state regime.

In the steady state, with appropriate boundary conditions for each level to model the threshold location, the heat equation would become stationary in the form of the Poisson equation. The driving input would be the only source term of activity at the sensory unit, and appropriate source terms modeling the shape of incoming pulses for the rest of units; activity destruction at the top (and slowest) unit would be the only sink. Because of symmetry, the solution at any level could also be obtained by solving for positive activities with a reflecting wall at zero. However, we have been sloppy in the wording because the quantity that is conserved is not activity but its square. This is because the Wiener process has independent increments, which implies that its quadratic variation or mean squared displacement equals the elapsed time; in other words, the variance of a sequence of inputs equals the sum of the variances of inputs. This is analogous to how, in classical mechanics, kinetic energy—which is proportional to squared velocity—is conserved, but not velocity. Under this view, the driving input is periodically (with period T_0) injecting into the system

energy chunks that are sequentially and stochastically relayed by each unit until reaching the end, from where they exit the system. This suggests that we refer to squared activity as "energy". Energy is conserved under addition of activities.

Since there is only one source of exogenous input with variance or energy $\sigma_{\mathcal{E}_0}^2$, assuming the system is devoid of activity at time zero, the total energy injected after time t must be $t\sigma_{\mathcal{E}_0}^2$. In the steady state, the power or energy flow that enters the system equals the energy flow leaving the system. Indeed, in one dimension the solution of the Poisson equation is just a linear function, in particular (accounting for boundary conditions) the constant $\sigma_{\mathcal{E}_0}^2$. Thus, in the steady state, the driving input intensity along with conservation principles determine the average flow of energy between successive levels: the rate of energy injected by the driving force equals the rate of energy transferred between any two successive levels, over long enough time spans.

Now we return to our system with gating, where changes in subthreshold activity are brought about by discharges. Although these are all-or-none events of activity transfer between units that result in jumps in the subthreshold activity, by local conservation of energy the average energy flow is constant and equal to the driving input $\langle \mathcal{E}_0^2 \rangle$ throughout the chain. Energy transfer, averaged over the discharges of all levels, occurs via diffusion [58]. In the steady state, the energy flux at any distance from zero is constant and equal to the driving input energy flux; this is because diffusion occurs in one dimension. So, although the dynamic profile of spreading activity is Gaussian, the steady state profile of average activity is flat. This is expressed by the continuity equation

$$\Phi = \nu_l \langle \mathcal{E}_l^2 \rangle \quad \forall l = 1 \dots n_l. \quad (17)$$

Here for simplicity we set $\nu_0 = P(\mathcal{E}_0 \neq 0) = 1$, so $\Phi = \sigma_{\mathcal{E}_0}^2$. Therefore, at each level the product of the discharge frequency and the energy relayed per discharge is constant on average, and equal to the energy flow injected into the sensory unit by the driving input Φ . This was confirmed in simulations. Hence it readily follows that

$$k_l = g_l^{-1/2} \quad \forall l = 1 \dots n_l. \quad (18)$$

With standard Gaussian driving input (Section III A), $\Phi = \sigma_{\mathcal{E}_0}^2 = 1$, which implies $D = 1/2$. Despite the vexing shape of subthreshold activity and pulse distributions (Fig. 2, in black and red) energy conservation entails that variances can be readily calculated.

By symmetry $\langle \mathcal{E}_l \rangle = 0$ so we can decompose the pulse variance into its absolute value raw and central components as $\sigma_{\mathcal{E}_l}^2 \equiv \text{var } \mathcal{E}_l = \langle \mathcal{E}_l^2 \rangle - \langle \mathcal{E}_l \rangle^2 = \langle \mathcal{E}_l^2 \rangle = \langle |\mathcal{E}_l|^2 \rangle = \text{var } |\mathcal{E}_l| + \langle |\mathcal{E}_l| \rangle^2$. Combining this with Eq. 17, we get

$$\sigma_{\mathcal{E}_l}^2 = \langle |\mathcal{E}_l|^2 \rangle = \text{var } |\mathcal{E}_l| + \langle |\mathcal{E}_l| \rangle^2 = \nu_l^{-1}. \quad (19)$$

Due to diffusion, subthreshold activities, pulses, and thresholds from coupled units are scaled by a factor equal to the inverse gain:

$$g_l^{-1} = \frac{\langle \mathcal{E}_l^2 \rangle}{\langle \mathcal{E}_{l-1}^2 \rangle} = \frac{\langle A_l^2 \rangle}{\langle A_{l-1}^2 \rangle} \quad \forall l = 1 \dots n_l; \quad (20)$$

this follows readily from conservation (Eq. 17) because pulse energy is inversely proportional to firing rate, and subthreshold activity is in turn proportional to the incoming pulse energy.

Since the discharge rate determines the variance of \mathcal{E} , it also determines indirectly some statistics of A and Θ . Using the law of total variance to split \tilde{A}_l into A_l^+ and \mathcal{E}_l at the threshold value Θ_l (Fig. 9) yields $\text{var } \tilde{A}_l = \langle \tilde{A}_l^2 \rangle = (1 - g_l) \text{var } A_l^+ + g_l \text{var } \mathcal{E}_l$, so

$$\langle \tilde{A}_l^2 \rangle = \langle A_l^2 \rangle + g_l \langle \mathcal{E}_l^2 \rangle, \quad (21)$$

where A_l^+ is the subthreshold activity excluding the rest state ($A_l = 0$), with $f_{A_l} = g_l \delta(0) + (1 - g_l) f_{A_l^+}$, and we used $\langle A_l^2 \rangle \equiv \sigma_{A_l}^2 = (1 - g_l) \sigma_{A_l^+}^2$. This is an approximation valid only for small w because this decomposition of \tilde{A} assumes a constant Θ_l .

Next, we seek the link between thresholds and activities. Here, the absolute value of activity comes forth as a fundamental variable due to the symmetry of the threshold updating rule (Eq. 4). Using the same approximation and the law of total expectation for $|\tilde{A}|$ at the threshold value we obtain

$$\langle |\tilde{A}_l| \rangle = \langle \Theta_l \rangle = \langle |A_l| \rangle + g_l \langle |\mathcal{E}_l| \rangle, \quad (22)$$

where we used again the law of total expectation (on $|A_l|$) to derive $\langle |A_l| \rangle = (1 - g_l) \langle |A_l^+| \rangle$ by noting that the pulse frequency ν_l (Table I) is also the fraction of firing trials, which set subthreshold activity to zero. Similarly, applying the law of total variance to $|\tilde{A}_l|$ yields

$$\text{var } |\tilde{A}_l| = g_l \text{var } \mathcal{E}_l + (1 - g_l) \text{var } |A_l^+| + g_l(1 - g_l)(\langle |\mathcal{E}_l| \rangle - \langle |A_l^+| \rangle)^2.$$

Despite the expressions obtained, the relationship between expected thresholds and pulse energies remains underdetermined. Thus, we now seek relationships between threshold expectation $\langle \Theta_l \rangle = \langle |\tilde{A}_l| \rangle$ and pulse size expectation $\langle |\mathcal{E}_l| \rangle$. If the subthreshold activity were

reset after each iteration, $\langle |\tilde{A}_l| \rangle$ would equal $\langle |\mathcal{E}_{l-1}| \rangle$ because $\tilde{A}_l = A_l + \mathcal{E}_{l-1}$. But in our system the presence of subthreshold activity has the effect of increasing $\langle |\tilde{A}_l| \rangle$ by a factor of k_ε . In the steady state

$$\langle \Theta_l \rangle = \langle |\tilde{A}_l| \rangle = k_{\theta,l} \langle |\mathcal{E}_{l-1}| \rangle \quad (23)$$

$$\langle |\mathcal{E}_{l-1}| \rangle = k_{\varepsilon,l} \langle \Theta_{l-1} \rangle \quad (24)$$

for $l = 2..L$, where $k_l = k_{\theta,l}k_{\varepsilon,l} \in [1, 2]$ and $k_{\theta,l}, k_{\varepsilon,l} > 1$. Although all these variables are functions of l , they converge (separately) as the chain becomes infinitely long ($l \rightarrow \infty$), as we will see in the next section.

C. Edge cases

To better understand our setup, it is instructive to probe a few limiting cases. From here, we will drop the subscript l for clarity, whenever an expression involves variables pertaining to the same level (Fig. 9). A smaller g entails lower discharge frequency, more energy accumulated, and a larger scaling factor k ; and vice versa. In the limit $g \rightarrow 0$, we would get $\langle |\mathcal{E}| \rangle^2 = \langle \mathcal{E}^2 \rangle = \Theta^2$ and $k \rightarrow \infty$. Conversely, in the limit $g \rightarrow 1$, subthreshold activity A would vanish along with scaling ($k = 1$). However, these limit expressions are incompatible with the threshold setting rule (Eq. 4): $\langle |\tilde{A}| \rangle \equiv \langle |A + \mathcal{E}/k| \rangle \approx \Theta$ cannot be located at an extreme, except in the degenerate case $\text{var } |\tilde{A}| = 0$. It can be observed that the threshold expands with respect to pulse size mean as $\langle |\mathcal{E}| \rangle / k < \Theta$ (Table I); now let us examine the implications of $\langle |\mathcal{E}| \rangle / k = \Theta = \langle |\tilde{A}| \rangle$, namely the equality of pulse size expectation before and after addition to subthreshold activity. This would hold if $|\mathcal{E}/k| + A \geq 0$ because the sum of the expectation of random variables equals the expectation of their sum, so $\langle |\mathcal{E}/k + A| \rangle = \langle |\mathcal{E}/k| + A \rangle = \langle |\mathcal{E}| \rangle / k + \langle A \rangle = \langle |\mathcal{E}| \rangle / k$, since A is symmetric about zero. But $|\mathcal{E}/k| + A \geq 0$ is unfeasible because it would entail $\max |A| = \Theta \leq \Theta/k = \min |\mathcal{E}/k|$ (see Fig. 9), which would be achievable only in the limit $g \rightarrow 1$, where A vanishes. However, by briefly indulging in this unfeasibility we can find an upper bound for the discharge rate: if $\langle |\mathcal{E}| \rangle / k = \Theta$ were true while somehow retaining multiplicative scaling, we can assume that —with frequency g_u — diffusive scaling should be counterpoised by the probability mass g_u released by each discharge (cf. 9, area below \mathcal{E}) as

$$g_u^{-1/2} = 1 + g_u, \quad (25)$$

which after reshuffling becomes $g_u^3 + 2g_u^2 + g_u - 1 = 0$, which can be solved using Cardan's cumbersome formula or numerically, and has a single real root $g_u \approx .46557$.

D. Fixed threshold approximation

For driving input distributions symmetric about the origin, the key to work out the expected values of A and \mathcal{E} is noting that squared activity or energy is conserved (Eq. 17) in perfusing the chain, while the threshold location is also derived indirectly from energy. To simplify the subsequent analysis, we fix the threshold to $\theta_* \equiv \langle \Theta \rangle$, corresponding to the limit of vanishing threshold fluctuations $w \rightarrow 0$ (so $\text{var } \Theta = 0$). Swapping the square of the expectation with the expectation of the square $\langle \Theta^2 \rangle = \langle \Theta \rangle^2$ is a form of mean field approximation: it neglects correlations. This is justified because w should be typically a small value for an adaptive system that learns the structure of its environment by iterative exposure to stimuli —then typically the time scales of threshold and activity dynamics are widely separated [2]. Since A and \mathcal{E} are necessarily linked to $\Theta = \langle \tilde{A}^2 \rangle$ and $g = k^{-2}$, we need to write down four equations or constraints.

The steady state discharge frequency $g_* = k_*^{-2}$ must be such that the scaling induced by expanding diffusive forces from energy accumulation $\sim g^{-1}$, which monotonically decreases with g , matches the increase in energy discharged $\sigma_{\mathcal{E}}^2 \equiv \langle \mathcal{E}^2 \rangle$; this is expressed by Eq. 21. Hence, a constraint among subthreshold activity, pulse, and threshold energies can be derived from a continuity equation integrated over one cycle of input signalling —so the discharge frequency of the current unit is g . Taking the interval $[\theta_*, \max \mathcal{E}]$ corresponding to the support of $f_{|\mathcal{E}|}$ (Fig. 9), in the steady state the inward and outward flows of energy must cancel out (by local conservation), so

$$g\sigma_{\mathcal{E}}^2 = g(g\sigma_{\mathcal{E}}^2 + \sigma_A^2) + \theta_*^4, \quad (26)$$

where the left hand side is the averaged pulse energy as outward energy flow integrated over one cycle and $\sigma_A^2 \equiv \langle A^2 \rangle$. In the right hand side, the first term corresponds to the direct inflow of energy from post-pulse activity — $\langle \tilde{A} \rangle = g\langle \mathcal{E}^2 \rangle + \langle A^2 \rangle$ weighted by the probability $P(\tilde{A} > \theta_*) = g$ — and the second term quantifies the diffusive transfer of energy from A to \mathcal{E} . The rationale for the latter rests on Brownian motion properties: the energy flux through θ_* for a "packet" of activity concentrated at the threshold (the "energy of the threshold")

is θ_*^2 per time unit, and the duration of a discharge cycle is the expected hitting time for reflected Brownian motion (which embodies the symmetry of the densities) is also $\tau_{\pm\theta_*} = \theta_*^2$ (see Appendix B, Eq. B1). Thus, the expected total energy transported across the threshold over one cycle with a continuous exogenous driving input energy flux $\Phi = 1$ (see section IV B) by purely diffusive effects would be $\theta_*^2\theta_*^2 = \theta_*^4$.

Another equation can be obtained by considering that discharge frequency is inversely proportional to the between-level scaling of energy. The average energy remaining in the form of (squared) subthreshold activity immediately after a discharge A^+ divided by the squared threshold should equal the discharge frequency $\frac{\sigma_A^2}{\theta_*^2} = g$. This is because, by conservation, the accumulated squared subthreshold activity as a fraction of the squared threshold establishes the discharge frequency. Equivalently,

$$\frac{\sigma_A^2}{\theta_*^2} = g(1 - g), \quad (27)$$

which is in good agreement with the simulations (Table I). Note that $g(1 - g) \approx 1/4$ holds for a relatively broad range of $g \approx 0.5$ values.

To spot a relationship between threshold and pulse energies, an essential ingredient is the effect of diffusion on the density of absolute post-pulse activity $|\tilde{A}|$. Heuristically, the average pulse energy transmitted, over one cycle, as a multiple of squared threshold $\frac{g\langle\mathcal{E}^2\rangle}{\theta_*^2}$, should follow from an analogous ratio between the threshold energy and the incoming pulse size energy $\left(\frac{\langle|\tilde{A}|\rangle}{\sqrt{g}\langle|\mathcal{E}|\rangle}\right)^2 = \frac{\theta_*^2}{g\langle|\mathcal{E}|\rangle^2}$. This ratio is larger than 1 and reflects that the addition of incoming pulses to subthreshold activity has the diffusive effect of "bumping up" the mean absolute value. By design, the threshold is set to the post-pulse *absolute* activity mean (Eq. 4), so increasing the mean absolute value from $\sqrt{g}\langle|\mathcal{E}|\rangle$ to θ_* (which equals $\langle|\tilde{A}|\rangle$ and the infimum of $|\mathcal{E}|$) necessarily affects the ratio of pulse energy discharged to threshold energy, such that energy conservation is satisfied. Bringing these expressions together, $\frac{\theta_*^2}{g\langle|\mathcal{E}|\rangle^2} = \frac{g\langle\mathcal{E}^2\rangle}{\theta_*^2}$, which rearranged is

$$\theta_*^2 = g\langle|\mathcal{E}|\rangle\sigma_{\mathcal{E}}, \quad (28)$$

which evinces that larger scaling factors ($k = g^{-1/2}$) call for longer tails. In the limit of zero dispersion $\text{var } |\mathcal{E}| \rightarrow 0$ and $\langle|\mathcal{E}|\rangle^2 \rightarrow \langle\mathcal{E}^2\rangle \equiv \sigma_{\mathcal{E}}^2$, it becomes $\frac{\theta_*^2}{\langle\mathcal{E}^2\rangle} = g$, so the ratio of threshold and pulse energies equals the discharge frequency.

A fourth equation stems from the properties of diffusion, applied to the absolute values of the system variables (Fig. 9). By design, $\theta_* = \langle|\tilde{A}|\rangle$ minimizes the mean squared error of

$|\tilde{A}|$, so $\text{var } |\tilde{A}| = g\langle(|\mathcal{E}| - \theta_*)^2\rangle + (1-g)\langle(\theta_* - |A|)^2\rangle$ (the same relation is embodied in Eq.22). Noting that $\text{var } |\tilde{A}|$ is the mean squared displacement from θ_* , the contributions from the lower $|A^+|$ and upper $|\mathcal{E}|$ partial second order moments can be deduced to be inversely proportional to their respective probability masses, which coincide with their respective renewal frequencies (g for \mathcal{E} and $1-g$ for A^+):

$$\frac{\langle(|\tilde{A}| - \theta_*)^2\rangle_{>\theta_*}}{\langle(\theta_* - |\tilde{A}|)^2\rangle_{\leq\theta_*}} = \frac{g\langle(|\mathcal{E}| - \theta_*)^2\rangle}{(1-g)\langle(\theta_* - |A^+|)^2\rangle} = \left(\frac{g}{1-g}\right)^{-1}.$$

After rearranging,

$$\frac{\langle(|\mathcal{E}| - \theta_*)^2\rangle}{\langle(\theta_* - |A^+|)^2\rangle} = \left(\frac{1-g}{g}\right)^2, \quad (29)$$

wherewith we can derive expressions for mean absolute values:

$$\langle|\mathcal{E}|\rangle = \frac{\theta_*^2 + g^2 - \langle A^2\rangle(1-g)}{2g\theta_*} \quad (30)$$

$$\langle|A|\rangle = \frac{\theta_*^2 - g^2 + \langle A^2\rangle(1-g)}{2\theta_*} \quad (31)$$

Equations 26, 27, 28, and 29 constitute a system of four interlocked nonlinear equations, which can be solved iteratively with a numerical routine; we used `fsolve` from MATLAB 9.2 (The MathWorks, Inc.; Natick, Massachusetts); thus with the fixed threshold approximation we get

$$\begin{aligned} g_* &\approx 0.4565, \\ \sigma_{A_*} &\approx 0.3322, \\ \theta_* &\approx 0.6668, \\ \sigma_{|\mathcal{E}_*|} &\approx 0.9742, \\ \sigma_{|A_*|} &\approx 0.2222, \\ k_* &\approx 1.4801, \end{aligned}$$

whence $k_{\varepsilon_*} \approx 1.4609$, $k_{\theta_*} = 1.0132$ also follows. These values are in reasonable agreement with $n_t = 10^7$ iterations numerical simulation estimates; Fig. 8 shows a reasonable convergence toward the fixed threshold approximation estimates over the first 7 levels. To account for one-step autocorrelations (Eq. C2) in calculating error estimates, we used effective sample sizes based on the the autocorrelation time [59, 60]: $\tau = 1 + \sum_{i=1}^{\infty} \rho^i$ (with ρ^i autocorrelation at lag i), which is roughly twice the decay time constant of the covariance function ($1/w$ and $\frac{3}{4}\theta^2$ for $\theta^{(t)}$ and $a^{(t)}$ respectively, see Appendix C).

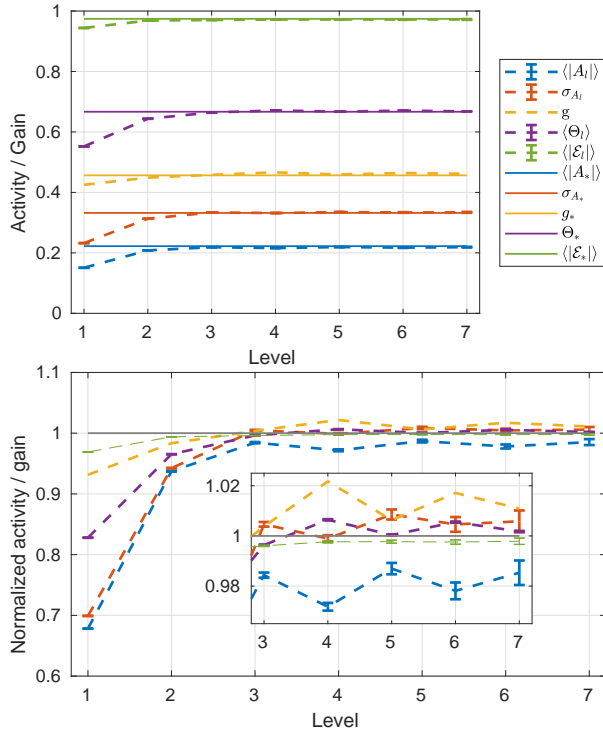


FIG. 8. Estimates of $A, g, \Theta, \mathcal{E}$ relevant statistics (top plot legend) across levels $l = 1 \dots 7$. Dashed lines indicate values estimated through numerical simulations (number of iterations $n_t = 9 \cdot 10^6$), whereas solid lines indicate values found with the fixed threshold approximation. The bottom graph shows the same variables, normalized by their fixed threshold estimate homologues. Errorbars indicate s.e.m. corrected for autocorrelation by use of effective sample sizes.

In deriving these solutions we have implicitly assumed (Eqs. 26, 28) that incoming pulses are identical to the outgoing pulses, up to a scaling factor k —which implies that the same scaling relationship holds for any variable respect to its homologue of the preceding level. This assumption deserves a justification.

V. RESCALED RECURRENT LOOP CONFIGURATION

The activity and threshold update and discharge rules (Eqs. 1 – 4) prescribe a sum of the incoming pulse and truncated subthreshold activity random variables. Clearly, the shape of the post-pulse activity density $f_{\tilde{A}_l}$ depends on the shape of $f_{\mathcal{E}_{l-1}}$, and these in turn depend on the shape of $f_{\tilde{A}_{l-1}}$ from the preceding level. But what happens if all levels are iteratively coupled as chain links? Fig. 8 suggests that as the chain approaches an infinite number of

links ($l \rightarrow \infty$), all variables converge respectively to specific densities, and that at level l any variable is a larger, k -scaled, self-similar replica of its precursor in level $l - 1$. Hence, we can set the incoming pulse to be a self-similar version of the incoming pulse as in the following recurrence relation:

$$\varepsilon_{t+1} = \begin{cases} a_t + \varepsilon_i/k_t & \text{if } a_t + \varepsilon_i/k_t \geq \theta_t \\ \varepsilon_j & \text{else} \end{cases} \quad (32)$$

$$a_{t+1} = \begin{cases} 0 & \text{if } a_t + \varepsilon_i/k_t \geq \theta_t \\ a_t + \varepsilon_i/k_t & \text{else} \end{cases} \quad (33)$$

$$\theta_{t+1} = (1 - w)\theta_t + w|a_t + \varepsilon_i/k_t| \quad (34)$$

$$k_{t+1} = \langle |\varepsilon_{1:N}| \rangle, \quad (35)$$

where here subscripts denote time instead of level indices and $\varepsilon_i, \varepsilon_j \sim \varepsilon_{1:t}$ are randomly and independently (bootstrap) resampled a pool $\varepsilon_{1:N} = \{\varepsilon_1, \dots, \varepsilon_N\}$ that in turn is replenished with the outgoing pulses. Resampling the incoming pulse ε_i instead of picking the last pulse ε_t is required because the actual configuration we are trying to mimic is essentially feedforward (unidirectional, toward higher levels l) and stochastically driven, so we need to avoid putting in spurious autocorrelations. The "else" assignment ε_j in Eq. 32 picks out a past value to become ε_{t+1} , instead of zero as in Eq. 3; this is consistent with the definition of \mathcal{E} (Section III) by ensuring that zero values are excluded. Eqs. 32 – 35 constitute a form of bootstrap resampling (Section E); after resampling and replacing a pool of $N = 10^5$ data points for 10^6 iterations (see Fig. 21), we obtain densities invariant under rescaling (Fig. 9), which can be seen as the limiting densities of Fig. 2 for $l \rightarrow \infty$. This is analogous to how universal scaling functions emerge on large scales in critical systems [61].

Eq. 35 estimates the scaling factor through the time average of the outgoing pulse size —note that the incoming pulse sizes are rescaled by the inverse of the scaling factor (Eqs. 32, 33). This time average is taken over a time span $[1, N]$; by the law of large numbers the larger is N , the scaling factor estimate becomes more accurate.

Eq. 34 is the delta learning rule (or stochastic gradient descent), an algorithm that converges in probability to the expectation of $|\tilde{A}|$ with a speed and variance dependent on the parameter w . Specifically, Eq. 34 can be expanded as $\theta_t = w \sum_{i=1}^t (1 - w)^{i-1} |\tilde{a}_{n-i}| + (1 - w)^t \theta_0$, which determines the balance at which past values are forgotten and new ones are incorporated into the estimate of Θ . Thus, Eq. 34 could be replaced by performing explicit

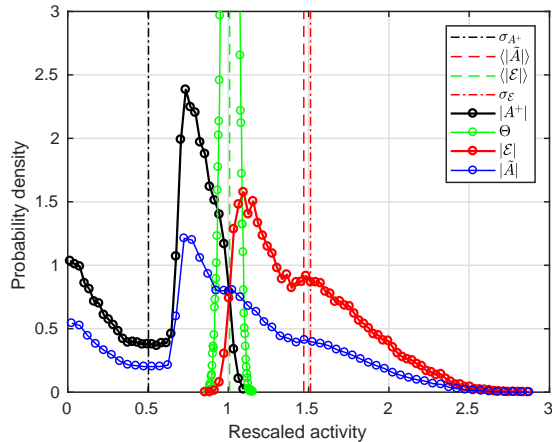


FIG. 9. Self-feeding configuration density estimates of $|A^+|$, $|\tilde{A}|$, $|\mathcal{E}|$, and Θ with $w = 0.01$. Note the (signed) variable densities are symmetric. The density of incoming pulses is set to the density of outgoing pulses divided by $\langle |\mathcal{E}| \rangle$, so that incoming pulse size mean equals 1. A bootstrapped pool of $N = 10^5$ data points for each variable was resampled and replaced one sample at a time for 10^6 iterations. Vertical lines indicate the location of relevant statistics (see legend).

threshold averaging as

$$\theta_{t+1} = \langle |\tilde{a}_{1:N}| \rangle, \quad (36)$$

which, similarly to Eq. 35, estimates $\langle \Theta \rangle$ with higher accuracy if N is large enough (assuming the system reaches a steady state regime).

Eqs. 32 – 35 constitute a 4-dimensional nonlinear recurrence relation, which simulates the feedforward configuration defined in Eqs. 1 – 4 in the limit $l \rightarrow \infty$. Borrowing the theory of Markov chains on continuous state space [62], it can be shown that both this recurrence relation and the original feedforward configurations are equivalent to an aperiodic and recurrent Harris chain, that hence has a unique stationary distribution —which describes the steady state regime. This stationary distribution is the 4-tuple $[f_{\mathcal{E}}, f_A, f_k, f_{\Theta}]$ of the "eigenfunctions" invariant under iteration of the map composed of sum, truncation, and rescaling operations (k also plays the role of eigenvalue, determining the scaling factor between successive levels). Assuming that k_t converges for large t , then $g_t = k_t^{-2}$ also holds from conservation (Eq. 17), with $g_t = \frac{1}{N} \sum_{t=1}^N \mathbb{1}_{\tilde{a}_t > \theta_t}$ the discrete-time version of Eq. 6.

Since both the recurrence relation and the feedforward map configurations are not differentiable (in fact not even continuous), conventional linear stability analysis is infeasible;

besides, the stochastic driving input precludes the existence of fixed points, except in terms of averages (Section IV D). Instead, the stationary distribution that emerges from the interplay of driving stochastic input and dynamical rules is a stochastic state that has no deterministic counterpart —without input, the system would remain quiescent forever. This is similar to how the persistence of noise-induced memory in excitable media [63] is contingent on a continuous input of extrinsic stochastic fluctuations. Analogously to the local stretching and global folding of orbits typical of nonlinear maps, the recurrent configuration map displays stretching and resetting (through the convolution-truncation operations) and contraction (rescaling of incoming pulses), but with the crucial difference that noise is injected by randomly sampling the pulse density. Noise here is an indispensable ingredient; in fact, the recurrence relation is effectively acting upon densities, rather than on "point-states".

By definition, the system satisfies global balance in the steady state —the transition rate among all states are such that the distribution of states remains stationary. To understand how states evolve locally, we can look at the transition function, which specifies the probability, given the current state, for all possible next states, i.e. the conditional density of the next state given the current state. The transition function was estimated numerically. First, consecutive duplets from the time series a_t and ε_t in recurrent configuration were sampled, and the resulting 2-D domain was split up into square bins of length 0.05; this yield bivariate histograms of the joint densities (Fig. 20). The conditional densities were then readily calculated by dividing the values of each column by the column total sum; the plots are shown in Fig. 10. The absence of discharge in the next state is indicated as $\varepsilon_{t+1} = 0$.

In the left column of Fig. 10, the low density in the bottom-right and top-left corners of $P(a_{t+1}|a_t)$ confirm the intuition that a state of large subthreshold activity a_t (of either sign) tends to be followed by a small a_{t+1} . The left middle column evinces that incoming pulses can only trigger outgoing pulses of the same sign. Outgoing pulse size increases monotonically with respect to both incoming pulse size and current subthreshold activity (middle left and right columns), with $\min \langle |\varepsilon_{t+1}| \rangle_{|a_t} \approx 0.54$ at $|a_t| = 0$. However, next state subthreshold activity reaches a maximum for non-boundary values of incoming pulse size ($\max \langle |a_{t+1}/k| \rangle_{|\varepsilon_t} \approx 0.57$ for $|\varepsilon_t| \approx 1.43$, middle right column) and current subthreshold activity ($\max \langle |a_{t+1}/k| \rangle_{|a_t} \approx 0.47$ for $|a_t| = 0$, left column). The shape of discharge rate as a function of current subthreshold activity can be gleaned from $P(a_{t+1} = 0|a_t)$ in the left column; here also we observe that discharge rate extrema are reached at non-boundary

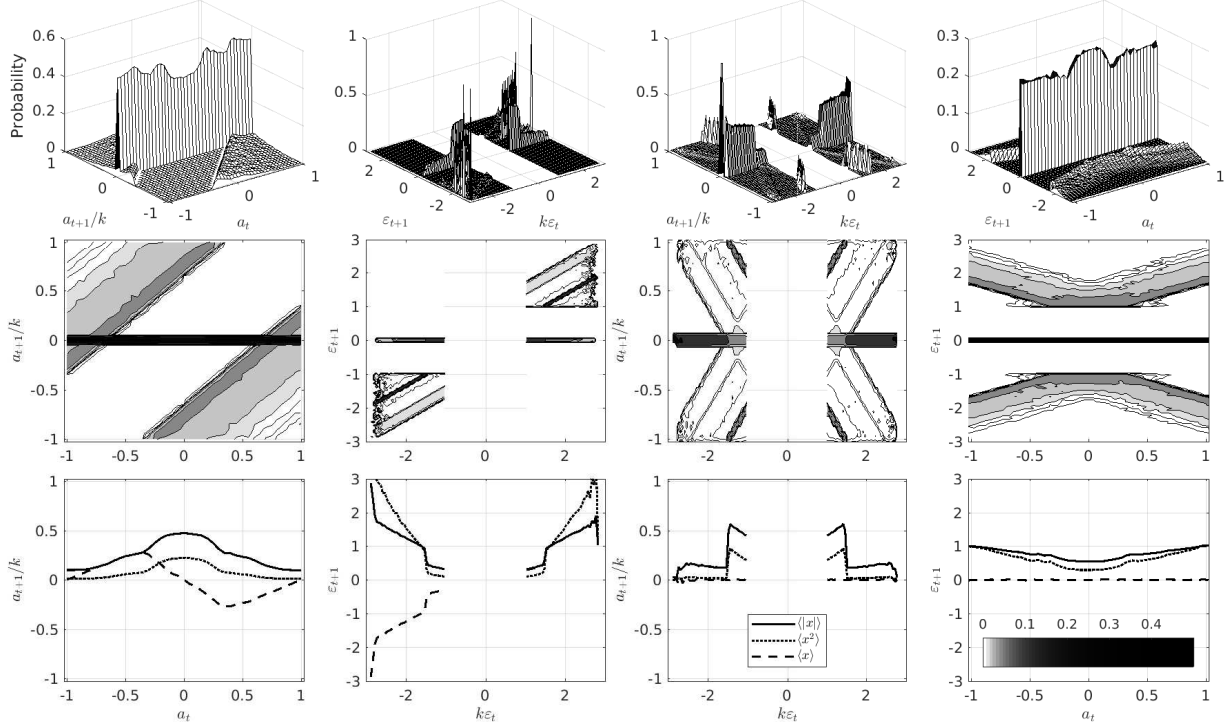


FIG. 10. Surface (top) and contour (middle) plots of the transition functions $P(a_{t+1}/k|a_t)$ in left, $P(\varepsilon_{t+1}|k\varepsilon_t)$ in middle left, $P(a_{t+1}/k|k\varepsilon_t)$ in middle right, and $P(\varepsilon_{t+1}|a_t)$ in right. Some variables have been scaled by k or $1/k$, so that $\langle |\tilde{A}| \rangle = \langle \Theta \rangle = 1$, to facilitate comparison. The bottom row shows the conditional expectation of the next state given the current state $\langle x \rangle$, where x is given by the figure column index, and the absolute $\langle |x| \rangle$ and squared $\langle x^2 \rangle$ conditional expectations. The color bar in the bottom right plot is the color legend of the middle row; it represents probability. The abrupt fluctuations at the boundaries in the middle left column are artifacts due to binning of samples in low density regions. Created with the same data as Fig. 9.

values (e.g., there is a minimum of $P(|a_{t+1}| = 0)$ at $|a_t| \approx 0.35$). Note also that any incoming pulse of size larger than $2\theta_t$ (which rescaled equals $2k_* \approx 2.96$ if $\theta_t = 1$ as in Fig. 10) would trigger a discharge, regardless of its sign and a_t . Such pulse sizes would be contracted by an expansion of the threshold, so we expect them to lie close to $\max |\mathcal{E}|$; this is supported by the estimated densities of \mathcal{E} in Fig. 10.

The transition function represents the probability $P(x_{t+1} = j|x_t = i)$ of moving to state i given current state i . Fig. 10 also shows that under repeated iteration, most trajectories of $x_t = [a_t, \varepsilon_t]$ would contract or decay to zero. This reflects that, at each level, the dy-

namics are dissipative and dissipation occurs at the same rate that energy arrives (although the cascade of levels as a whole conserves energy, except perhaps at the top level, which is a design feature). However, under a constant flow of energy with activity distributed as $P(x_t = i)$, the trajectory of the system is attracted to a stationary distribution defined by the "eigendensity" of the joint distribution of incoming energy and excitable element dynamics $P(x_{t+1} = j, x_t = i) = P(x_{t+1} = j|x_t = i)P(x_t = i)$ (Fig. 20 in Appendix E). The eigendensity of the system is precisely the stationary distributions $f_{\mathcal{E}}$ and f_A (9): if we arrayed the four transition matrices in Fig. 10 as a the single system transition matrix ($a_t, a_{t+1}/k$ (left bottom) and $k\varepsilon_t, \varepsilon_{t+1}$ (top right) in the main diagonal and $k\varepsilon_t, a_{t+1}/k$ at the bottom right and a_t, ε_{t+1} at the top left), diagonalizing this single matrix, the unique eigenvalue 1 would have eigendensity $f_A, f_{\mathcal{E}}$. The asymmetric form of the system transition matrix reflects that detailed balance is not satisfied: in general forward and backward transitions between any two states are not equiprobable.

A. Fixed threshold approximation

We are prominently interested in the case where the time scale of threshold and activities are separated, which leads to the fixed threshold approximation (Section IV D). In the limit $w \rightarrow 0$, k and Θ stop being stochastic variables and become fixed to k_* and θ_* , which implies that the discharge probability g_* is also constant. Notice that this also bears on the shape of the stationary distributions of \mathcal{E} and A . Removing threshold fluctuations reduces Eqs. 32 – 35 to a 2-dimensional system. Further, the state of each unit is now defined by a single variable a_t (as opposed to by a_t and θ_t). In symbols (similarly to Eqs. 15, 16 but in terms of random variables):

$$\mathcal{E} = A + \mathcal{E}/k_* \quad \text{if } A + \mathcal{E}/k_* > \theta_* \quad (37)$$

$$A = \begin{cases} 0 & \text{if } A + \mathcal{E}/k_* > \theta_* \\ A + \mathcal{E}/k_* & \text{else} \end{cases} \quad (38)$$

$$\theta_* = \langle |A + \mathcal{E}/k_*| \rangle \quad (39)$$

$$k_*^{-2} = g_* = P(|A + \mathcal{E}/k_*| > \theta_*) \quad (40)$$

These equations describe variable trajectories under the rescaled recurrent loop configuration, with the fixed threshold approximation. This approximation is useful because it

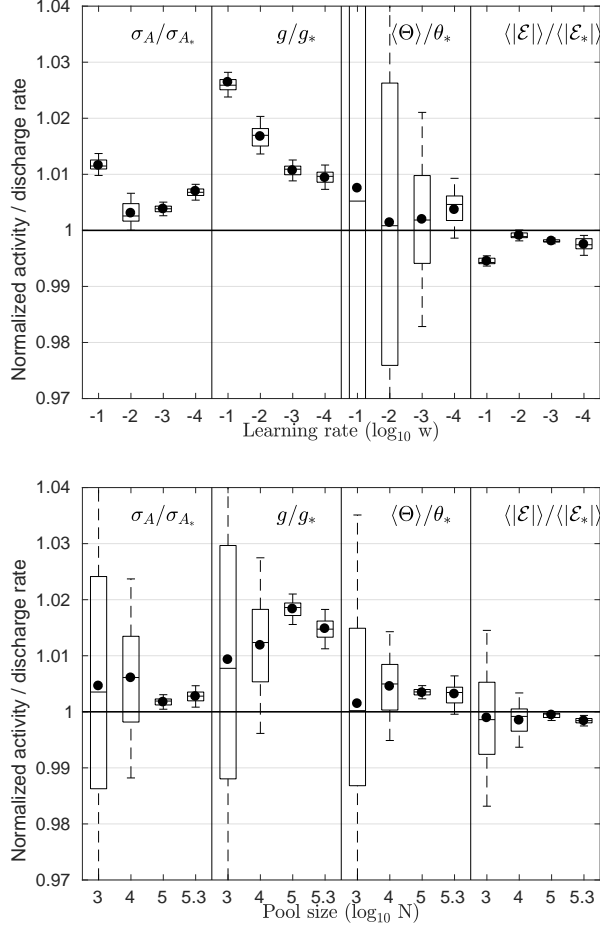


FIG. 11. Numerical simulation of uncorrelated driving input system in rescaled recurrent configuration. Variable estimates are normalized with respect to the fixed threshold approximation values. The top boxplot shows estimates calculated with Eqs. 32 – 35 and $N = 10^5$; the bottom boxplot uses Eqs. 32, 33, 36, 35. Box edges: 1st and 4th quartiles; box central segment: median; whiskers: 5th and 95th percentiles; solid circles: mean.

renders the system amenable to analytic approximations, while preserving the threshold-activity separation of time scales. Although we cannot implement a recurrence relation for the fixed threshold approximation as in Eqs. 32 – 35, we can approximate it by setting a small w (Appendix E).

Estimates of variable statistics under the rescaled recurrent loop configuration are shown in Fig. 11, where it is apparent that discharge rates are positively biased with respect to the fixed threshold approximation value, with bias being larger for noisier estimation

procedures. As seen in Fig. 9 (area under $f_{\tilde{A}}$ to the right of θ), g is a monotonic decreasing nonlinear function of Θ (cf. Eq. 6). Since the slope of $f_{\tilde{A}}$ is negative for any relevant value of $\tilde{a} = \theta$ (Figs. 2, 9; Appendix F), if we assume f_{Θ} symmetric about its mean, we can venture that $g \geq g_*$, with equality when Θ has zero variance fluctuations (fixed threshold). This is because $f_{\tilde{A}}$ is larger to the left of θ than to the right, so the rate of increase of g due to leftward fluctuations outweighs the rate of decrease due to rightward fluctuations, so the larger is the variance of f_{Θ} , the larger becomes the expectation of g . This explains the positive bias of noisy g estimates (which implies a negative bias for k). Further, threshold fluctuations entail a larger variance of A and \mathcal{E} , which also leads to positive biases for σ_A and $\sigma_{\mathcal{E}}$ (cf. 9, where f_{A^*} and $f_{\mathcal{E}}$ overlap due to the threshold fluctuations); the latter implies a negative bias for $\langle |\mathcal{E}| \rangle$ because $\langle |\mathcal{E}| \rangle = 1 - \sigma_{\mathcal{E}}$. Finally, we do not have a simple explanation for $\langle \Theta \rangle$ estimates being positively biased, but we surmise that the hard boundary at the origin "reflects" the threshold fluctuations.

B. Autocorrelated inputs

The PC can be generalized by allowing autocorrelated or non-zero mean driving input. Assuming the driving input is Gaussian distributed, this can be suitably modeled with fractional Gaussian noise [56] with parameter or Hurst exponent $H \in [0, 1]$ or with a non-zero mean normal distribution, which corresponds to $H = 1$.

Picking up the brief discussion in section III A, if the driving input has strictly positive (or in general non-zero) mean, in the limit $l \rightarrow \infty$ the pulse density $f_{\mathcal{E}}$ approaches a Gaussian density with mean twice the mean of the preceding unit: $\langle \mathcal{E}_l \rangle = 2\langle \mathcal{E}_{l-1} \rangle$ (note that for positive inputs $\langle \mathcal{E} \rangle = \langle |\mathcal{E}| \rangle$). In this case, $g = 0.5$ because firing occurs as soon as exactly two pulses arrive, the first one leading to $A_l = \mathcal{E}_{l-1}$ and its summation with the second one $\langle \mathcal{E}_{l-1} + \mathcal{E}_{l-1} \rangle = 2\langle \mathcal{E}_{l-1} \rangle = \langle \mathcal{E}_l \rangle$. Consequently, $\langle \Theta_l \rangle = \frac{3}{2}\sigma_{\mathcal{E}_{l-1}} = \frac{3}{4}\sigma_{\mathcal{E}_l}$ holds because \tilde{A}_l is distributed as two lumps with the same probability mass corresponding to the random variables $A_l = \mathcal{E}_{l-1}$ and \mathcal{E}_l , which have expected value $\langle \mathcal{E}_{l-1} \rangle$ and $\langle \mathcal{E}_l \rangle$ respectively. For finite l , we get $\langle |\mathcal{E}| \rangle < \sigma_{\mathcal{E}}$ and $\sigma_A < \frac{1}{2}\sigma_{\mathcal{E}}$, which become equalities for $l \rightarrow \infty$. This is because for each level step-up, average pulse energy scales as $\langle \mathcal{E}_l^2 \rangle = 4\langle \mathcal{E}_{l-1}^2 \rangle$ by conservation (Eq. 17), and squared mean pulse size scales as $\langle \mathcal{E}_l \rangle^2 = 2^2\langle \mathcal{E}_{l-1} \rangle^2$ by linearity of expectation. As l approaches infinity, the contribution to energy due to variance vanishes: $\lim_{l \rightarrow \infty} \frac{\text{var } \mathcal{E}_l}{\sigma_{\mathcal{E}_l}} = 0$

(idem for A_l). This is why the resulting densities are the same as for $H = 1$, as we will see soon. These results were verified in numerical simulations (not shown). Note that both mean squared and mean absolute activities are conserved.

For arbitrary $H \in [0, 1]$, Eq. 18 is not correct anymore. Instead,

$$k_l = g_l^{-H} \quad \forall l = 1 \dots n_l. \quad (41)$$

holds. Eq. 18 is a particular case of Eq. 41, which accomodates autocorrelated Gaussian input. Although not uncorrelated anymore, fractional Gaussian noise preserves self-similarity [56]. Energy, as defined till now as squared activity (Section IV B), is not conserved anymore for $H \neq 0.5$ because the summation of squared activities would not be anymore linear, nor mean squared displacement of "activity particles" would be linear in time. However, if we redefined energy as a function of activity that is conserved in time, then from Eq. 41 we can deduce that it would have the form $k^{1/H} \sim g^{-1}$, where the right hand side has units of time and the left hand side is has (equivalent) units of activity raised to the power of $1/H$. Thus, the PC with autocorrelated driving input can also be viewed as an "anomalous cascade", by analogy with anomalous diffusion: mean squared activity (mean energy) is not necessarily linear in time $\langle \mathcal{E}^2 \rangle \equiv \langle E \rangle \sim t^\alpha$, and the anomalous diffusion coefficient would be related to the Hurst exponent as $\alpha = 2H$.

In this spirit, we can restate Eqs. 26 – 29, in keeping with the heuristic arguments of section IVD, by substituting $1/2$ for H where suitable. After taking $\sigma_{\mathcal{E}} \equiv \langle \mathcal{E}^2 \rangle = 1$ for simplicity (without loss of generality), we get

$$g = g(g + \sigma_A^2) + \theta_*^{2+H^{-1}} \quad (42)$$

$$\frac{\sigma_A^2}{\theta_*^2} = g^{2H}(1 - g) \quad (43)$$

$$\theta_*^2 = g^{H+1/2} \langle |\mathcal{E}| \rangle \quad (44)$$

$$\frac{1 + \theta_*^2 - 2\theta_* \langle |\mathcal{E}| \rangle}{\frac{\sigma_A^2}{1-g} + \theta_*^2 - 2\theta_* \frac{\langle |A| \rangle}{1-g}} = \left(\frac{1-g}{g} \right)^{2H+1}, \quad (45)$$

which together with $\langle |A| \rangle = g\theta_* \langle |\mathcal{E}| \rangle$ constitutes a nonlinear system of five equations and five variables, solvable with iterative algorithms. However, both the equations above and Eqs. 32 – 35 rest on the fixed threshold approximation assumptions and on heuristics based on energy conservation in (anomalous) diffusion. Eq. 29 also makes the implicit assumption that the density of \tilde{A} has a connected support, which breaks down for high enough H (when f_A and $f_{\mathcal{E}}$ are no longer connected at Θ).

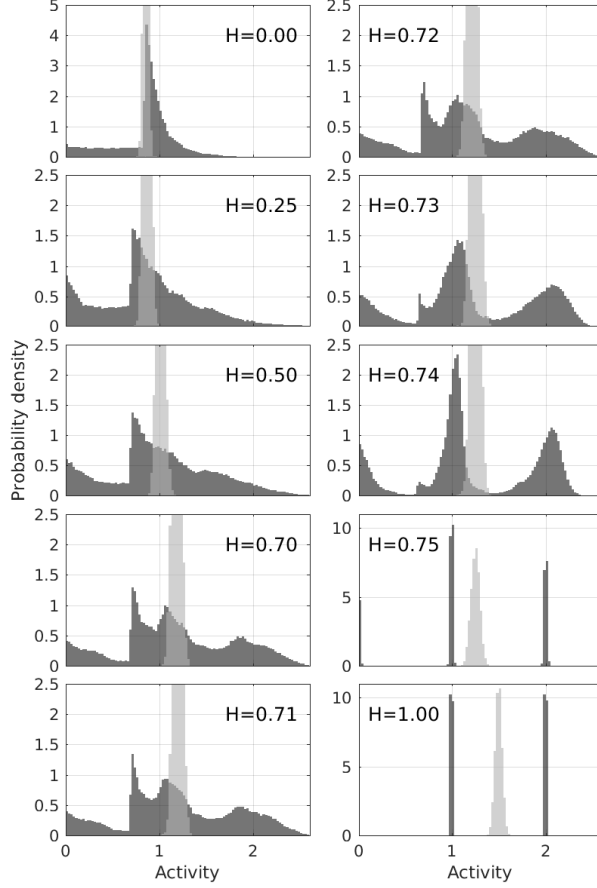


FIG. 12. Histogram of positive half densities of post-pulse activity \tilde{A} (dark) and threshold Θ (light) for different degrees of Gaussian input autocorrelation (indexed by the Hurst parameter H) in rescaled recurrent loop configuration with explicitly averaged thresholds (Eqs. 32,33,36,35). Simulation parameters: $5 \cdot 10^6$ burn-in iterations; pool size $N = 10^5$. As in Fig. 9, all plots have been scaled such that activity 1 corresponds to the average incoming pulse size $\langle |\mathcal{E}|/k \rangle$.

In recurrent configuration, with super-diffusive (anomalous diffusion with $H > 0.5$) input, there is a H beyond which incoming pulses never reach the threshold. This occurs because incoming pulses are so autocorrelated that most of the time two consecutive pulses have the same sign, triggering a discharge and thereby expanding the threshold enough that the incoming pulse maximum is less than the threshold minimum $\max |\mathcal{E}|/k < \min \Theta$ (where f_Θ is well approximated by a Gaussian; see section C). This starts occurring for some $H \in [0.74, 0.75]$ (see Fig. 12), where the post-pulse activity density breaks up from one into three blobs (actually, into five because all densities are symmetrical about the origin). Hence,

the fixed threshold approximation is invalid beyond this value. Under repeated iteration, these blobs degenerate into increasingly narrow sticks, exactly as described at the beginning of this subsection for $H = 1$. This transition is marked by a discontinuity in the derivative of all the PC variables with respect to H (Fig. 13).

The extrapolation of the gain-related variables to autocorrelated input, requires substituting H for $1/2$ as above (Eqs. 42 – 45):

$$k_*(H) = g_*^{-H} \quad (46)$$

$$k_{\theta,*}(H) = \frac{\theta_*}{g_*^H \langle |\mathcal{E}_*| \rangle} \quad (47)$$

$$k_{\varepsilon,*}(H) = k_*(H)/k_{\theta,*}(H). \quad (48)$$

Plotting the result of iterating the map defined by Eqs. 32, 33, 36, 35 that uses explicit averaging to determine the threshold with autocorrelated Gaussian noise input with parameter H yields the estimates of the PC variables as a function of H (Fig. 13). The homologous plot with thresholds determined with the delta learning rule (Eqs. 32 – 35) can be found in Fig. 22 in Appendix E. These curves display a few remarkable aspects. First, there is a concavity (or convexity) with peak at $H \approx 0.75$, surging from $H \approx 0.71$, on the otherwise smooth curves. Second, the fixed threshold approximation (solid thin in Fig. 12, using Eqs. 42 – 48) curves are a good fit only in the vicinity of $H = 1/2$; otherwise they widely deviate from the estimated curves. This was expected for H high enough that the density of \tilde{A} splits up (12); that it deviates elsewhere could be due either to the heuristics used in Eqs. 32 – 35 or to the trouble in adjusting simulation parameters that expedite fast and reliable convergence to the fixed threshold approximation. This is because there is a trade-off between the variance and convergence speed (bias) of the numerical estimates: in principle, increasing larger pool sizes (N) or smaller learning rates (w) leads to estimates approaching the fixed threshold approximation, but this also entails slower convergence rates (see also Appendix E). In either way, Fig. 12 shows that, as expected, curves with simulation parameters closest to the fixed threshold approximation (largest N 's or smallest w 's) are also the closest to the fixed threshold approximation curves. Yet, only $\langle |\mathcal{E}| \rangle$, g and k are a reasonably good fit in a neighborhood of $1/2$. Third, most curves bear non-trivial extrema—neither at the boundaries of $[0, 1]$ nor at $1/2$.

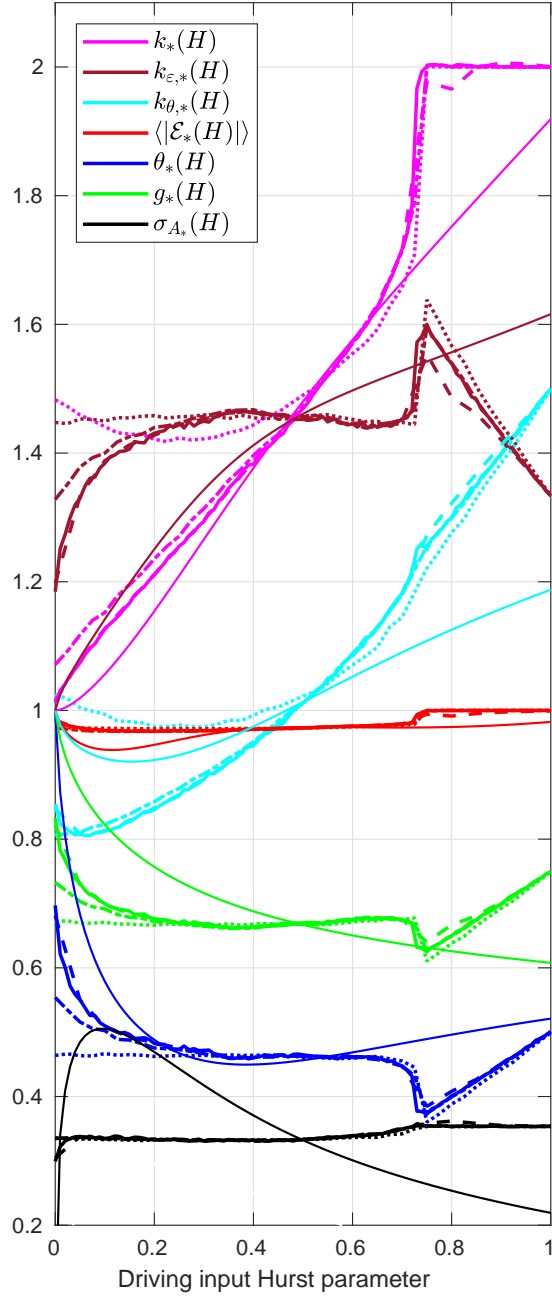


FIG. 13. Perfusive cascade variables' estimates (see legend) with explicit threshold averaging, as a function of driving input autocorrelation, in recurrent rescaled loop configuration. A , \mathcal{E} are scaled consistently with $\langle \mathcal{E}^2 \rangle = 1$. Line style indicates the estimation procedure: closed form expression (Eqs. 42 – 45) derived through the fixed threshold approximation (solid thin); simulation with pool sizes $N = 10^3$ (dotted), $N = 10^4$ (dash-dotted), $N = 10^5$ (solid thick), $N = 2 \cdot 10^5$ (dashed).

VI. A TOY MODEL FOR IRREDUCIBLE UNCERTAINTY IN THE CORTICAL HIERARCHY

The perfusive cascade model is a chain of excitable elements with finite refractory period, akin to neurons, that propagate pulses unidirectionally when an internal state variable (sub-threshold activity, in analogy with membrane potential) exceeds a range of values defined by another state variable (threshold, in analogy with threshold potential). This arrangement echoes both the electrophysiological properties of neurons and a taxonomy of the brain whereby temporal scales define the categories [31]. But the key motivation behind this arrangement is the purported operation of good regulators [17] compelled to trade off metabolic power [64] or metabolic power consumption and representational accuracy in environments comprising multiple spatio-temporal scales. In particular, we envisage the PC as a toy model of a good regulator or living system that implicitly incorporates an internal generative model of its environment [25] and conforms with the Bayesian brain hypothesis [24, 27, 28]—which states that the brain performs Bayesian inference on its sensory inputs to uncover the hidden causes generating them—and inference being accomplished through a hierarchical Bayesian scaffolding [26, 65–67]. To accomplish inference in real time on a continuous flow of sensory input, a Bayesian filtering scheme—which allows inverting dynamic non-linear state-space models by assuming that the conditional densities on the system’s states and parameters are Gaussian—can be used. Crucially, to make inference tractable, the system can be assumed to rely on a mean-field partition of a variational density [24, 27] to approximate its recognition model, which computes the posterior density over its internal states given the sensory input. In particular, dynamic expectation maximisation (DEM) is a Bayesian filtering scheme that accomodates random fluctuations on sensory inputs and (hierarchical) internal states that is rendered tractable through its use of a mean-field partition of its variational density, and is thus a plausible candidate scheme for general brain computation [68].

The PC focuses only on the purported dynamics of the flow of unresolved irreducible uncertainty through the hierarchy, thus overlooking any inferential machinery. Thus, it can be seen as a toy model that attempts to capture salient dynamical properties common to any system incorporating DEM. Importantly, and somewhat arbitrarily, in this article surprisal refers to irreducible uncertainty, i.e. the fraction of uncertainty (bearing information content)

that cannot be resolved by the system just by reconfiguring its generative model, and that can only be resolved or suppressed by exerting action in the environment. We assume that the system can act on uncertainty that reaches the top level—which motivates that uncertainty can be suppressed only at the top level. In this setup, pulses \mathcal{E} can be thought of as representing prediction errors relayed to a higher area, thresholds Θ as excitability or synaptic efficacy, and subthreshold activity A as subthreshold membrane potential. In turn, their associated squares represent surprisal relayed between-levels, surprisal threshold, and surprisal tolerance, respectively. Importantly, these and their associated variables—e.g. the discharge rates in Table II rightmost column—are not characteristic of single neurons, but rather of cortical regions, ordered by their rank in a model hierarchy of increasingly larger spatio-temporal scales.

Perfect accuracy is infeasible in a stochastic world. In Bayesian inference, only in the large data limit and given some regularity conditions, the posterior density approaches a docile Gaussian around the mode [69] [70]. In practice, each biological species embodies a generative model molded by stochastic selective pressure, that only needs to be good enough to avoid extinction. Although so far these generative models have been good enough to preserve a multiplicity of life forms, they cannot foresee some of the hazardous and rarest events their environment is capable of engendering: e.g. the effect of past rare events may have faded in the genetic memory, or some of them may simply have never occurred [71, 72]. These outlier events are part of the complex NESS (heavy-tailed) structure that exerts selective pressure, but have remained hidden because they are rare. Although we recognize that these events carry catastrophic effects [73, 74] for highly optimized living systems [43] and self-organized ecological systems [25], in this article we focus in the typical environmental conditions that the generative models have been selected to deal with, which justifies the use of mildly random inputs, i.e. Gaussian noise.

A. The trade-off between metabolic power consumption and performance

Living creatures are highly optimized systems [43, 75] that delicately balance performance, metabolic energy consumption, and robustness or surprisal tolerance requirements. We assume environmental uncertainty is suppressed fast enough to avoid death, but slow enough to make use of available resources efficiently. This implies maintaining both a good

enough model or representation of the environment and a good enough behavior, where good enough is understood in the Darwinian fitness sense. In animals, specifically in their brains, synaptic scaling and firing rate homeostasis [76] can be construed as mechanisms to suppress uncertainty. Notably, under the parametric empirical Bayes formulation of the free energy principle [18] (see section VI C), this trade-off is implicit in the phylogenetic priors that oversee the form of the internal generative model; e.g. in vertebrates, the hypothalamus is likely to make up a fraction these priors via its regulation of metabolic processes. Neuronal spikes (discharges) are costly: in humans, possibly fewer than 1% of neurons on average are active at any given moment [77], which means the typical activation pattern is sparse [78]. An upper bound estimate, assuming precise timing, for the information encoded by single neurons is ≈ 6 bit/spike [79]. In our simplified model, we assume that discharge cost is proportional to the pulse size: $C = \sum_l |\mathcal{E}_l|$, which resonates with rate coding (a reasonable alternative would be that all discharges were equally costly). Hence, metabolic power consumption is $P = \sum_l \nu_l |\mathcal{E}_l|$.

Surprisal increases linearly with time (see VI C), but not so its square root (activity). This strongly motivates the existence of a finite refractory period: at small time scales, activity fluctuates wildly—to the extent that it diverges in the limit of size zero fluctuations—so allowing pulses to be triggered by small fluctuations would be exceedingly wasteful. Indeed, the ratio of pulse size to discharge period at level l is proportional to the square root of discharge frequency:

$$\frac{\langle |\mathcal{E}_l| \rangle}{T_l} \approx \frac{.97 \sqrt{\langle \mathcal{E}_l^2 \rangle}}{T_l} = \frac{.97 \nu_l^{-1/2}}{T_l} \sim \nu_l^{1/2}, \quad (49)$$

so the metabolic *power* cost grows as a square root law with firing rate, thus diverging for a vanishing refractory period (which entails a zero threshold, see Appendix B 2). For autocorrelated input with Hurst exponent H , this generalizes to ν_l^{1-H} . In opposition, the metabolic *energy* cost (per spike) decreases with discharge frequency:

$$\langle |\mathcal{E}_l| \rangle \approx \nu_l^{-1/2}. \quad (50)$$

This suggests that, in view to save metabolic energy, it is expedient to let surprisal accumulate as much as the system can afford the attendant decrease in performance—while surprisal accrues linearly, the ebb and flow of sensory input follows a 1/2 exponent power law.

The PC implicitly (not actually modeled) achieves representational accuracy by transmitting pulses to supraordinate levels that correct or suppress the received error signals (driving input and incoming pulses from subordinate levels) through the reconfiguration of internal states. At the sensory level, these relayed pulses are implicitly elicited by a discrepancy between the sensory input expected under the system’s generative model, and the actual sensory input (the driving input); at non-sensory levels, this discrepancy is already embodied in incoming pulses. This scheme is an instance of predictive coding, an iterative approach to inference related to the EM algorithm, that assumes random effects can be modeled as additive Gaussian fluctuations [27, 65].

The excitability of pulse emission defines the trade-off between metabolic power and representational accuracy, and is regulated through two "knobs": threshold adaptation (Eq. 4) and refractory period (T_0). The refractory period discretizes the allowed firing times; this is why we cannot model our excitable elements as "Brownian neurons" to derive hitting times (cf. Appendix B). The refractory period is a physiological limitation in neurons: after a spike (discharge), neurons require some time to restore the electrochemical gradient that enables further spiking. But at the same time, a refractory period checks metabolic power consumption —at the expense of limiting perceptual accuracy and reaction time.

Threshold adaptation is a compromise solution between metabolic power consumption and performance: it enables the system to adjust its accumulated surprisal to the sensory input variance, while keeping a balance between representation update frequency, which is directly related to performance, and metabolic power consumption, both of which are proportional to discharge rates. Given a fixed driving input and number of levels n_l , setting more liberal thresholds entails higher discharge rate and gain (which entails faster reaction time) and higher metabolic power consumption $P \sim \sum_l \nu_l^{1/2}$, but less stored subthreshold energy $\sum_l \langle A_l^2 \rangle$ (which entails higher performance, see section VIC below). However the average flow of surprisal or energy remains unchanged in the steady state (section VIC).

B. Complexity on Earth’s surface and in the brain

The surface of Earth, where humans evolved, is an open and dissipative system sustained by a continuous flow of energy. Living beings (good regulators [17]), must incorporate a model of the world that is good enough to warrant our existence. Hence, we can in principle

estimate an upper bound for the complexity of this model by assessing the local complexity of the local environment where evolution took place. The relevant measure in this calculation is the minimum average information content [80] per unit time of the local environment, that bears on a living system’s Darwinian fitness. This is roughly upper bounded by the entropy production rate on Earth’s surface, which attends the existence of a NESS that continuously dissipates energy; reversible processes and subsystems at equilibrium do not contribute to the generation of complexity. One way to see this is considering that the Sun’s radiant flux or power is (directly or indirectly) the main source of (metabolic) energy for most known forms of life, and also the primary source of complexity of ecosystems; and the complexity of an ecosystem’s energy flow roughly establishes its entropy (together with its temperature). This view resonates with synergetics [81], a theoretical framework that explains the formation of self-organized structures far from equilibrium, when fed by some gradient of energy. Here, the radiant flux would be the gradient that feeds life, the self-organized structure born in it.

The following is a back of envelope estimation of the average information content about the environment modeled, and the average surprisal tolerated, by the brain. In living systems, much of the complexity of the environment may be implicitly modeled; developmental processes, physico-chemical properties, and metabolic processes are encoded in the genotype and typically expressed with no involvement of the brain. A lower bound to the complexity of the human generative model C_G (of which the brain is just a fraction) is the information encoded in the genome, which is estimated to be around $I_G \approx 6\text{Gb} \approx 10^{10}\text{b}$. This information is combined with the complexity generated by ontogenetic processes [49] to yield the generative model.

The Earth’s surface entropy production is roughly $\sigma_\alpha \approx 0.6 \text{ WK}^{-1}\text{m}^{-2}$, where absorption of the Sun’s incoming irradiance is by far the largest contribution [82]. Thus, the information rate needed to encode the spatio-temporal structure of the average m^2 patch of Earth surface is approximately σ_α . Before the Neolithic revolution, a typical human foraged (very coarsely) in a territory of area $\approx 10^{10}\text{m}^2$ (assuming a home range of 100 km [83], and a height of 10 m) over a life span of $\approx 10^9\text{s}$. Hence, the human generative model must comprise a dynamical model of at least a fraction of this spatio-temporal “home” domain, which after multiplying yields a total entropy of $S_\alpha \approx 10^{19}\text{J/K}$ or $S_\alpha/k_B \approx 10^{42}$ bits, where k_B is the Boltzmann constant. This is an upper bound to the generative model complexity $S_\alpha > C_G$

that accounts for all sources of information that encode the environment of a typical living system on Earth’s surface, but it includes microscopic degrees of freedom, so it is a gross overestimate. We can hone this bound by looking into the anatomy of the brain: it contains more than $\approx 10^{14}$ synapses and each synapse comprises $\approx 4\text{b}$ [84], which indicates a total storage capacity of $\approx 10^{15}\text{b}$. This is a tighter upper bound to the information content of the generative model, which we can approximate to its complexity $C_G \approx 10^{15}\text{b}$. This suggests that living systems only need to model a fraction $C_G/S_\alpha \approx 10^{-27}$ of the “home” environment’s information content to compose good enough models.

Looking into the benefits that brains afford enables to roughly estimate the irreducible information rate —the fraction of uncertainty that cannot be resolved without acting on the environment, and that aggregates random fluctuations across all levels of the presumed hierarchical structure of the environment. The motivation for this is that the generative model complexity can be crudely thought of as the probabilistic structure that the trajectory of surprisal describes in high dimensional space [85]. The fluctuation theorem relates the relative probability of average irreversible entropy $\langle S \rangle_t$ production or destruction over some time interval t [86] $\frac{P(\langle S \rangle_t = B)}{P(\langle S \rangle_t = -B)} = e^{Bt}$ so we can use it to find a lower bound to the surprisal bitrate B by asking how much time could a living system operate without its brain without significantly jeopardizing its fitness. How long a creature whose brain has been take away would survive in its milieu? One day or $\approx 10^5$ s is a reasonable guess nowadays, but perhaps $\approx 10^4$ s was more pertinent before the Neolithic revolution. Substituting above $t = 10^4$ and assuming a small probability ratio of 2 (indicating the point when the absence of brain starts to bear consequences), we get $B \approx 10^{-4}$ b/s, which is a very lax (lower) bound. The aggregate afferent sensory bitrate is estimated $\approx 10^7$ b/s. Sensory information is compressed downstream the brain hierarchy by by maximizing the mutual information between input and increasingly lower-dimensional neural representations [87]. Thus, the information capacity of higher-order functions such as visual attention [88] and cognitive control is $B \approx 50$ b/s (it ranges approximately from 2 to 100 b/s [89]). [90] Assuming B stands for the surprisal that is preserved throughout the hierarchy (and might account for a significant fraction of the stream of consciousness), the exogenous input surprisal that accrues each refractory period $T_0 = 5\text{ms}$ (section III A) is $\sigma_{\mathcal{E}_0}^2 = B \cdot T_0 \approx .25$ b. From this, we can calculate the diffusion constant (section IV B) $D = \frac{\sigma_{\mathcal{E}_0}^2}{2T_0} \approx 25$ b/s.

C. Energy, free energy, and surprisal tolerance

Let a particular living system be a good enough (unbiased) model receiving Gaussian distributed sensory input error (noise) [25]. If this system incorporates a generative model and performs inference about environmental states through a variational density [27], then the analogous to PC energy is called free energy in the context of variational Bayesian learning and hierarchical models of the brain [24, 27]. The free energy principle states that by (locally) minimizing free energy with respect to the variational parameters (the sufficient statistics of the variational density, encoded in brain states), variational learning prescribes how a living system reacts to stimuli. This can be achieved by extending variational Bayesian inference methods to keep surprisal at check along time trajectories through DEM [68], which thereby furnishes a principled simulation of brain dynamics.

In contrast, PC neglects the representation of internal states, to focus on the flow of unresolved surprisal. Although in it a generative model of the environment is not explicitly specified, surprisal (energy) is still conserved under addition, relayed downstream the hierarchy, and finally suppressed at the top level. At each level l , surprisal is accumulated as \tilde{A}_l until it triggers a discharge at a level set by Θ_l^2 (energy threshold), with pulse and subthreshold densities determined by the hierarchy level (Fig. 2) —that converge to the density in rescaled recurrent loop configuration for large enough l (Fig. 9). Note that when a system has random noise in a conserved property, small fluctuations preserve their influence across increasingly larger scales, because fluctuations can die away only by diffusion [61, 91]. This supplies another account of the observed scale invariance in the PC hierarchy (section VII) —whose conserved property is squared activity or energy.

A parametric empirical Bayes model can be replicated as a chain of conditionally independent subsystems where the stochastic terms are independent at each level [92]. This architecture has been incorporated explicitly as a hierarchical model of the cortex, where its stochastic terms at each level are typically assumed to be Gaussian distributed [27]. In contrast, stochastic terms in PC are Gaussian only at the sensory level. This is not just because the particular structure of the generative model is bypassed; more essentially, uncertainty suppressed at a given level is not resolved, instead it is simply relayed as a "pending issue" to the supraordinate level. Thus, the aggregate subthreshold activity is a form of "tolerated" surprisal stored across the hierarchy as $\sum_l A_l^2$, that models surprisal tolerance. This

is evinced in the subthreshold activity surprisal content of high frequencies: it is relatively small and similar for all levels; however low frequencies contain increasingly large quantities of surprisal at higher levels (Fig. 5). In contrast, pulse surprisal has a rather flat spectrum for all levels (Fig. 4). This is the major feature distinguishing PC from hierarchical Bayesian models of the cortex, and the reason for non-sensory levels having non-Gaussian stochastic terms.

D. Separation of time scales

An essential feature of systems displaying SOC is the time scale separation between slow driving and fast relaxation terms [2]. In our setup, we have also implicitly defined an infinite separation of time scales between the accumulation of incoming pulses and discharges: driving input must wait for all links of the chain to "decide" whether to discharge or not, before being injected in the next time step. However, even without this design feature, a large (but finite) separation of time scales between levels is a naturally emerging property of PC.

There are no free parameters in PC; time scale ratio, threshold, and discharge rate are properties derived from the defining rules. Unlike the cascade of bifurcations propagated from fast to slow elements in a chain of Roessler systems studied by [93], which requires strong pairwise correlations and adjusting time scale ratios to a specific range and Roessler parameters to the vicinity of bifurcations, PC exhibits long-range temporal correlations without parameter tuning. Instead, time scale ratios between hierarchical levels emerge naturally from the requirement to strike a balance between resource consumption and representational accuracy.

Separation of time scales implies the existence of characteristic time scales, and is inherently incorporated in the physics of the world. This can be expounded from the vantage point of synergetics [81], which rests on the adiabatic approximation or enslaving principle, whereby systems of coupled elements bearing separated time scales self-organize such that only a few slow and typically unstable order parameters become naturally relevant to explain the global structure, and fast oscillations become enslaved to slow modes. Synergetics has also been demonstrated in behavioural dynamics like bimanual coordination [94]. Separation of (time) scales is also illustrated by the manifestation of scale invariance in discrete fashion

(as opposed to continuous). Discrete scale invariance (DSI) is associated with log-periodic oscillations (cf. 7) and complex critical exponents, and has been studied e.g. in hierarchical geometrical systems, and rupture and growth phenomena [57]. There is also some evidence of DSI in human waking electroencephalogram (EEG) large voltage deflections [95], and in event-related changes of spectral power [96]. The center and ranges of behaviorally relevant brain oscillations categories with successively faster frequencies form an arithmetic progression on logarithmic scale [97]. It is plausible that the separation of time scales found in nature, through the evolution of a hierarchical architecture in the brain, resulted in neural variables exhibiting DSI.

E. A cortical cascade of irreducible uncertainty

Crucially, we have assumed that the generative model is good enough to stay unbiased, which means that the system is able to predict future environmental states with good enough accuracy to survive. This will be typically true, as long as the system remains in the environment that exerted selective pressure on it. However, this also means that the system will be overly vulnerable to perturbations of exceptional nature [43], i.e. perturbations that were absent during its evolutionary history.

Setting aside extreme events, the complex structure of the environment is well represented by an internal hierarchical model. Yet not all the entropy of the environment has a recognizable structure and so is reducible to a lighter parametric model: the remaining unexplained noise constitutes the sensory error—or sensory input in PC. This is irreducible uncertainty (surprisal), as opposed to the reducible uncertainty accounted for by the internal model, which we assume to be caused by many independent events that average to a sort of thermal noise, whose time integral is Brownian motion (Appendix B). Note the existence of an irreducible component to sensory uncertainty that is preserved downstream the cascade up to the top level is an assumption of PC, which is not justified in general.

The main virtue of PC is its simplicity: aside from the threshold adaptation rule and number of levels, it has no parameters. This comes at the cost of forgoing the internal configuration of the generative model. In DEM, bottom-up error signals modify their (supraordinate state) prior to suppress uncertainty. In turn, the prior constrains the kind of input that the its subordinate level expects. Each state carries Gaussian random fluctuations

whose reliability is parameterized by a precision variable. This scheme is remarkably comprehensive and can be designed to model any practically conceivable phenomenon e.g. responsiveness or attention to stimuli, and tolerance to uncertainty (e.g. tinkering with the D-step of DEM [68]). Thus, although DEM could be used to regulate the metabolic power-performance trade-off, through the judicious use of metabolic priors or through the regulation of the D-step duration, this would require ad hoc tuning. In our system, activities represent a fraction of uncertainty that is irreducible and accumulates up to the top level. Thus, pulses are interpreted as error signals restricted to the irreducible fraction of uncertainty, and are in general not Gaussian. Since we modeled surprisal as Brownian motion, higher units store increasingly larger quantities of surprisal although the discharge rule is common to all.

Element l 's activity A_l undergoes a random walk with step size distribution f_{ϵ_l} , where the steps can only occur at multiples of T_0 . At each level, activity is stochastically reset to some region closer to the origin —depending on the level of the discharging element— as a function of its distance to the origin (cf. [50]). This is one of many types of reversible Markov chain (random walk) that display power law dynamics [98]. Since the accumulating driving input is simply being relayed from level to level, the set comprising all system variables can be construed as a projection of a the stochastic process defined by the time series resulting from (say, Gaussian noise) driving input high-dimensional random walk onto the n_l one-dimensional activity variables. We have seen in the previous section that the mean squared displacement of activity (energy flow) is conserved: energy is simply transferred from the sensory to the top level, alternating between emitted pulses and stored subthreshold activity energies (Fig. 14), with a power spectrum similar to that of activities (Fig. 15).

Although we have only examined 1-dimensional input, the extension to d dimensions is straightforward. The fundamental solution to the diffusion equation (section IV B) can be readily generalized [57] to d dimensions, yielding a mean squared displacement $\text{MSD} = 2dDt$. Thus, the dimensionality of the state space is simply manifested as a linear expansion factor in activity MSD. This is important because it enables to expand the PC modeling scope to comprise high dimensional input time series, by only including a factor d for energies (or \sqrt{d} for activities) and letting the bilateral threshold generalize to a d -dimensional ball. Thus, surprisal remains a linear function of time, but if the now multidimensional activity space is partitioned into submanifolds —corresponding to its subelements, just as cortical

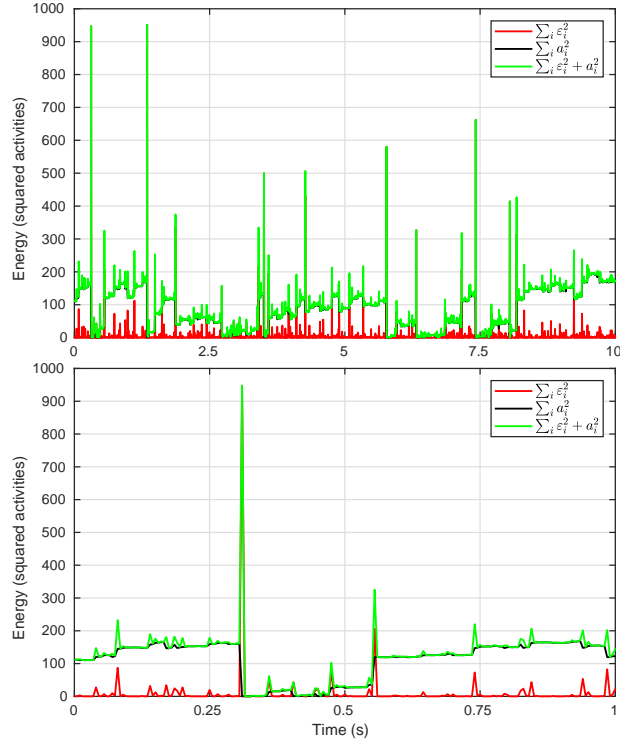


FIG. 14. Time series of pulse energies, subthreshold activity energies, for each $l = 1..7$ level and their sum, in steady state regime. Energy is interpreted as the surprisal or irreducible uncertainty emitted as pulses or stored as subthreshold activity (section VIE). Interval length: 2000 (top) and 200 (bottom) time steps. Parameters as in Fig. 1.

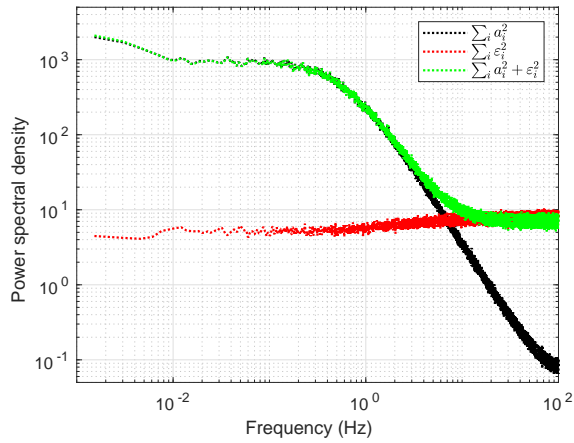


FIG. 15. Power spectral density estimate of the time series in Fig. 14. Estimation parameters as in Fig. 3.

columns constitute one brain area—, the surprisal of each subspace i will be weighted by its corresponding dimensionality d_i such that $d = \sum_i d_i$.

Our system has been stripped from the infrastructure specifying the internal states that infer environmental states (under the DEM scheme, this is the conditional expectations of states of the world [68]). However, we can envisage what the dynamics of its internal states would have been like if the generative model had been explicitly modeled. Each level l of the PC emulates an analogous level in the hierarchy of spatio-temporal scales that characterizes its environment, where l indicates the cortical region rank in sensorifugal order, so levels are more similar to cortical regions than to individual neurons. Hence the discharge rates of Table I are better understood as indicating transmission of activity between brain regions representing contiguous time scales. Pulse activity is a measure of the prediction error or mismatch between the sensory input actually received and the sensory input predicted by the current internal states or configuration of the system at each level. Likewise, pulse energy reflects surprisal being relayed to a supraordinate level. Since the system comprises a continuously actualized representation of the environment, it is coupled to environmental dynamics, and its state is encoded in the spatial pattern of activation of its excitable elements. The system tries to minimize uncertainty about the environment — match predictions with inputs, or suppress prediction errors— by dynamically reconfiguring its connectivity within and between levels (which in brains involves a subtle balance of excitation and inhibition [37, 99]). Hence, we expect that its dynamics will be largely defined by within-level *spatial* patterns of activation, which would not be detectable by their amplitude, but only by the activation topography. In summary, as in PC, pulses would display a mostly flat temporal spectrum (Fig. 4), whereas subthreshold activities would exhibit larger temporal correlations with a time scale congruent with the associated level (Fig. 5), but in addition both would display a rich spatial structure.

F. What happens at the top level?

By design, surprisal is quenched only at the top level in PC. The reason lies in the definition of surprisal: since it cannot be resolved by levels other than the top, it is conserved throughout the hierarchy. An intriguing account for this is that surprisal cannot be explained by automatic perceptual inferential processes, but it requires other suppression means e.g.

acting on the environment to suppress surprisal through the recruitment of top level mechanisms that map surprisal states to actions (the inverse model [100]). Such mechanisms typically require a model of the self-other distinction, which entails conscious processing [101].

G. What is the best rule for setting thresholds?

The threshold rule in Eq. 4 is equivalent to gradient descent on a surprisal quadratic loss (squared error) function [27] with learning rate w . Because the derivative of surprisal has activity units, the minimum mean squared error (MSE) of \tilde{A} is its mean. This is analogous to how the local derivative of free energy is proportional to prediction errors weighted by precision [27].

However, there are other plausible threshold adaptation rules. Perhaps the most relevant converges to the the median—which is the minimum mean absolute error (MAE)—through a judiciously small learning rate w :

$$\theta_i^{(t+1)} = \begin{cases} \theta_i^{(t)} + w & \text{if } |\tilde{a}_i^{(t)}| < \theta_i^{(t)} \\ \theta_i^{(t)} - w & \text{if } |\tilde{a}_i^{(t)}| \geq \theta_i^{(t)}. \end{cases} \quad (51)$$

Note this rule ignores the magnitude of the prediction error; instead it only acts on the sign of the prediction error by a fixed amount w .

This raises the question of whether there is an optimal threshold setting rule. Both MSE and MAE rules are ways to arbitrate the trade-off between metabolic energy and performance. Error or surprisal cost proportional to the error magnitude motivates MSE. MAE assumes that all non-zero errors as equally costly. Although in this article we have only used a MSE rule, this suggests a plausibly optimal rule: thresholds contract minimizing MSE, and expand minimizing MAE. The rationale is that thresholds should correct a firing shortage (by contracting) in proportion to its associated error because these are indicative of susceptibility to fatal outcomes, whereas corrections of firing in excess (by expanding) are motivated by metabolic energy saving.

H. A hierarchy of time scales in the brain

Activity power spectra (Fig. 5) exhibit a $\sim \nu^{-2}$ scaling exponent, and pulse avalanches (Fig. 7) are also scale invariant across up to (depending on the level) three orders of magnitude. The corner frequencies of activity spectra (Figs. 4, 5) lie in the midrange $10 \approx 100\text{Hz}$ and are associated with thresholds, which are directly related to the time scale of their corresponding levels (cf. Eq. 17). Conversely, pulses can be approximated as homogeneous Poisson processes (so discharge times are memoryless or independent of each other) which entails a flat spectrum [102] (cf. Fig. 4). This is because the random time at which a continuous-time stochastic process hits some target (hitting time) bears a density that depends on the form of the process, and in particular, the hitting time density for Brownian motion in a flanking threshold configuration (as in our system) has an exponentially decaying tail (see Appendix B2).

Linear superposition of these power spectra [103] could underpin the power law spectrum of EEG traces and LFPs of mammalian cortex [104]. Electrophysiological and modeling evidence indicate that LFPs may display Lorentzian function corner frequencies—characterized by e.g. postsynaptic current and dendritic current efflux decay times—that split the frequency range [105] into a flat ($\nu < 20\text{Hz}$), $\sim \nu^{-2}$ scaling exponent ($20\text{Hz} < \nu < 75\text{Hz}$), and ν^{-4} scaling exponent ($75\text{Hz} < \nu$) bands [106]. Temporal integration in dendrites or soma or exponentially decaying membrane currents are some known neural processes that can be modeled with the same Ornstein-Uhlenbeck process that describes activity and pulse dynamics (Appendix C). This contrasts with magneto- and electroencephalographic trace temporal scaling exponents, which are typically $\approx .8$ [19, 20], but with a large intersubject variability of $\approx .55\text{--}1.05$ [37, 107]. Their correlations with behavioral scaling exponents are both more prominent in higher brain areas than in sensory areas and more widespread in resting state than during task performance [22], consistent with PC dynamics, where bottom-up signals have flat spectra (Fig. 4) and higher levels display a wider frequency range of power-law form (Fig. 5).

Most hierarchical accounts of brain architecture—including PC—prescribe that sensory input drives the fastest (lowest) areas, whose signals then traverse the hierarchy sequentially activating areas with increasingly slower rhythms; likewise, slower rhythms modulate via top-down effects larger and faster subordinate domains [108]. This is supported by much

evidence. Higher frequency oscillations are confined to a small regions, whereas slow oscillations recruit large networks [109]. Beta oscillations are readily observable immediately after evoked gamma oscillations in sensory evoked potential recordings and can synchronize over long conduction delays that cannot be tolerated by gamma rhythms [110], that gamma rhythms display a smaller correlation length than beta rhythms [111], and with nearby cells coherence decreasing with distance [112]. Nested frequencies, where the phase of slower rhythms are correlated with the amplitude of faster rhythms [102, 113, 114], are pervasive across the whole spectrum of brain activity [115].

In the stylized architecture of PC, each level has associated a spatio-temporal scale defined by its height in the hierarchy, which mirrors the brain hierarchy [31, 116–119]. The sensory level is a pre-cortical element such as a thalamic nucleus relay: e.g. the lateral geniculate nucleus [120] is the main input that projects to the primary visual cortex. Hence, it would be located at the lowest level with a characteristic time scale of $\approx T_0$ or few milliseconds. Levels 2–5 would constitute the sensory-fugal streams of processing that transform sensation into cognition, while the sixth and seventh levels contain transmodal gateways that compose a coherent multimodal representation of the state of the world [117]. The hippocampus [29, 117] and the hypothalamus [117] are likely to be regions sitting at the top level with a time scale comparable to lifespan. In particular, the hypothalamus is the principal coordinator of the homeostatic, autonomic and hormonal aspects of the internal milieu [117]. The characteristic time scales of other brain areas would come between, e.g. ≈ 1 –100 ms for sensory areas, ≈ 10 – 10^3 ms for association areas (e.g. 0.8 s for LIP [121]), ≈ 10 – 10^3 ms for primary and premotor areas [122], ≈ 10 s for superior temporal sulcus and precuneus, ≈ 36 s for temporo-parietal junction and frontal eye field [118], > 10 s for anterior cingulate cortex and lateral prefrontal cortex, and a very long characteristic time scale of perhaps years for the medial temporal lobe (which contains high level objects such as person identities [123]) and orbitofrontal cortex (OFC; which harbors long-lasting affective values)[31]. Some areas near the top level such as lateral prefrontal and/or posterior parietal areas [117] are particularly interesting because they bear the crucial role of mapping internal states to action; this enables living systems to actively counteract exogenous perturbations to survive [124]. Finally, the sensory level operates ≈ 100 times faster than the top (seventh) level, while carrying $\approx 10^7/10^2$ times its information rate (section VIB, [109]). If the number of neurons in the temporal hierarchy of the cortex were proportional to their information

content, then there ought to be $\approx 10^3$ times more neurons in the sensory than in the top level, which gives an incremental number of neurons ratio of $\approx 10^{3/7} \approx 2.7$ between consecutive levels. Applying this quotients to a 10^{11} -neuron brain yields an estimate of $\approx 6 \cdot 10^7$ neurons in the top level, which matches the order of magnitude of the number of hippocampal neurons [125]. However, this hierarchical layout should be taken with a grain of salt. The hippocampus has also been proposed to be a temporal storage of explicit facts [126] that are transferred into the neocortex in order to improve the generative model of the brain, and a structure that encodes (temporal) ordinal structure without reference to particular events [127], which would place it near, but not at the top. Other areas might that might fit in the top level are those harboring long-term declarative memories (temporal cortex) [128], affective values (OFC) [31] and in general slowly oscillating areas [118, 129, 130].

I. Criticality in the brain

One of the reasons critical systems are interesting is that they may resemble life. Complex dissipative structures (NESS) typically arise when a steady flow of energy passes through a particular region of space. Conversely, creatures persisting long enough in complex environments must be able to counteract the fluctuations stirred by the energy flow, which means they can anticipate and act upon these fluctuations [18]. Life on Earth evolved in a critical world [131] that exhibits power law or fractal spatio-temporal spectra across a wide range of magnitudes [132] —e.g. in dynamic natural scenes [133]. This suggests that living creatures embody critical internal representations that unfold across a multiplicity of temporal scales. In humans, this is reflected for instance in the temporal frequency perception of natural scenes [134] and in brain synchronization metrics [135].

By design, systems that perform inference about the causes of its inputs through a variational free energy formulation (e.g. systems incorporating DEM) are disposed to destabilize their own dynamics (autovitiation); this is because they seek out regions of low free energy that have a low curvature, which leads to the apparition of slow dynamic modes (critical slowing) [32]. This is consonant with research suggesting that the brain lies on average in a slightly subcritical state [136, 137] (but see [37]) with occasional incursions into a supercritical state [32, 138]. This suggests that the purpose itself that defines perception —reducing the mismatch between environmental and internal states— is what induces criticality in

perceptive systems [139], similarly to self-organized critical systems. PC is a SOC system operating in subcritical phase because it has a unique driving force with a rate infinitesimal relative to activations (i.e. the next input waits for all chain elements to "decide" whether to discharge or not), energy is conserved, and it has a finite number of levels [2]. However, enabling it to accept input before the cascade ends would render it supercritical (cf. sandpile model with finite driving rate [2]).

Empirically, the hypothesis that the brain operates near criticality [12, 140] has also gained much (if not conclusive) support [16, 141, 142]. Power-law temporal correlations have been found in EEG [19, 20] and MEG signals [143] across a broad range of frequencies [106, 144], in functional neuroimaging data [145], and real neuronal avalanches (stereotyped population-size firing events) have been repeatedly observed in animals in multielectrode arrays, *in vitro* in acute cortical slices and cultures [14], and *in vivo* [16, 114], displaying spatio-temporal and neuronal group size scale invariance [146].

The continuous-input Bak-Tang-Wiesenfeld lattice sandpile model [3, 41] shares many traits with PC: discrete pulse density peaks (which is related to DSI, see section VID), energy conservation, and power law spectra for avalanches and stored energy, and Lorentzian temporal spectra [41]. Notably, when energy is injected from one end and dissipation is added, long range correlations are quenched, yet temporal spectra become $\sim \nu^{-1}$. This results from a linear superposition of the (now uncorrelated) independent lattice elements, which are composed of exponentials with decay times that depend on their location in the lattice. This is analogous to the mechanism that underpins the power law spectrum in our system, where uncorrelated energy (surprisal) accumulates successively at increasing time scales, setting up independently excitable elements of different intrinsic time scales (also to McWhorter's model of shot noise [147]). The key features that comprise this configuration are the separation of time scales (achieved by decorrelating dissipation in [41] and by hierarchical design in PC) and the chain topology.

In another similar model, input is injected into the center of a square lattice, constituted by elements characterized by threshold firing, refractory period, and synaptic plasticity [35]. This model displays power law distributions of avalanches (with exponent ≈ -1.2) and spectrum (≈ -0.8) presumably because its built-in plasticity in conjunction with random initial conditions carves a complex landscape of synapses with a near-critical branching parameter; however, it has many parameters. Adjusting the ratio of excitation and inhibition

can yield similar results [37], and this additionally furnishes an explanation for the wide range of temporal scaling exponents found in the literature.

J. Neuronal avalanches

Neurons in the cortex are likely to be segregated into layers contingent on their duties as predictive coding hardware. Specifically, prediction error (pulse) neurons would be allocated to supragranular and state neurons to infragranular cortical layers [18, 148], so we can liken pulses to prediction error neuron spikes in supragranular cortical layers. Neuronal avalanches are presumed to originate from activity in superficial (supragranular) layers 2 and 3 that propagates across multiple cortical columns in all regions of the cortex [114, 149]. This can be taken one more step further, by relating pulses to local field potentials (LFPs) [67] (the electric potentials recorded in extracellular space in brain tissue), which are the signals picked up by micro-electrodes and by EEG —the latter after filtering and diffusion across head tissues.

Here the term avalanche denotes a volley of pulses triggered within a single time step. Somewhat atypically, we let avalanche size to be proportional to the sum of its constituent pulse sizes. The mixture density $f_{\varepsilon_{min}}$ (section III C) then corresponds to recordings with high enough temporal (or spatial, if levels were spatially segregated) resolution to tell apart each individual pulse even within one time step (or avalanche) —akin to high resolution multielectrode recordings in electrophysiology. In contrast, the sum density $f_{\Sigma\varepsilon}$ comes from registering all the pulses generated within one time step (or avalanche) as their linear superposition [102, 150, 151]. The sum density is analogous to linear superposition of temporally overlapping post-synaptic potentials on micro-electrodes or LFPs on surface electrodes [103], where temporal subsampling [136, 151] or limited spatial resolution may blend separate avalanches into a single time-varying medley. However, note that the sequential nature of avalanches is lost in our system due to time discretization, which merges all pulses within a time step, and the lack of spatial extent within levels. At any rate, recall that in our system pulses (and their avalanches) cannot be naively interpreted as actual electrical potentials or spike counts (section VI E): for example, the analogous to the branching parameter [14] would be the gain g , but the lack of a within-level spatial dimension precludes sensible comparison.

Empirical estimates from microelectrode arrays suggest that neuronal avalanche size and durations bear scaling exponents $3/2$ and 2 respectively [14, 143, 149] (cf. $3/2$ with 1.77 in Fig. 7; or with 1.64 in Fig. 16). The number $3/2$ matches the avalanche size scaling exponent in a model of globally coupled (mean-field) threshold elements with random stimulation location [33] similar to the Olami-Feder-Christensen earthquake model [6], mean-field self-organized branching processes [152], many flavors of mean-field zero-temperature Ising models [153] and mean-field directed and dynamical percolation [154]. This is notable because the critical behavior of directed percolation belongs to a robust universality class that is widespread in systems exhibiting cascading transitions from active to absorbing phases, that is closely related to SOC [152, 154]. However, the significance of $3/2$ is moot because there are similar models with other scaling exponents [154], mean-field approximation are typically incorrect for low dimensional systems (e.g. 2-dimensional sandpile model [2, 3]) and the exponent estimate ≈ 1.5 – 2.1 may depend significantly on the spacing between electrodes in the array [140]. Further, avalanches occur in short timescales of 1–100ms [22, 155], but electrographic long-range temporal correlations timescales are in the range 1–1000 s, so it is plausible that the $3/2$ exponent be restricted to spreading of activity within (isofrequency) levels.

A priori, the most relevant operational variables are the densities of pulse activities and their avalanches (Fig. 7), which are related to neural activity. Nonetheless, energy densities allow to visualize the distribution of stored and relayed surprisal across levels (Figs. 16, 17). This can be interesting because energy is the only conserved quantity throughout the hierarchy, which in addition defines discharge rates, and has a physiological meaning (irreducible uncertainty that only the top level can quench). Therefore, we provide also the scaling exponents of pulse (scaling exponent -1.95 for mixture, -1.64 for sum density; Fig. 17) and subthreshold energy densities (scaling exponent $-.83$ for mixture, $-.29$ for sum density; Fig. 17). Both variables display power law behavior within their range, with a right tail roll-off more conspicuous for subthreshold activities caused by the thresholding.

K. Autocorrelated and non-Gaussian inputs

Autocorrelated input may occur when the system is not a good enough model of its environment or input. Then we would expect its predictions to be biased, which entails that

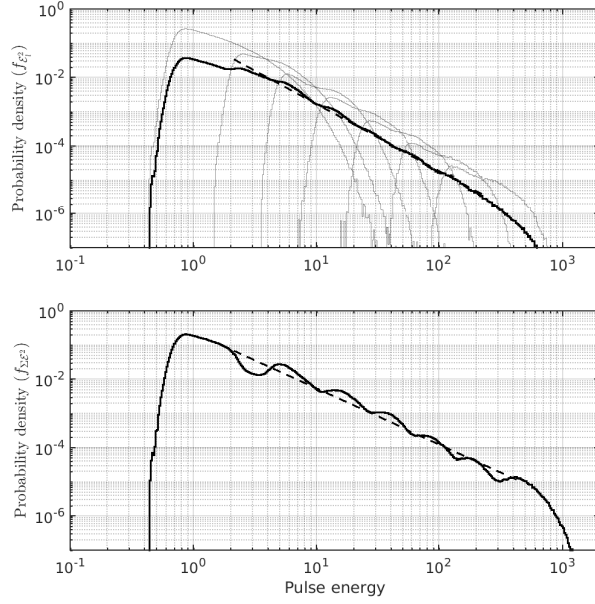


FIG. 16. Density estimates of pulse energies for $n_l = 7$ levels. Upper: mixture density (black), and individual levels (light grey) for all $l = 1 \dots 7$. Lower: total sum of pulse energies. Slopes (dashed, top -1.95 , bottom -1.64) were fitted in the least squares sense in a range that excluded finite-size effects: $[\langle \mathcal{E}_1^2 \rangle, \langle \mathcal{E}_7^2 \rangle]$ for $f_{\mathcal{E}_{mix}}$ and $[\langle \mathcal{E}_1^2 \rangle, \sum_{i=1}^7 \langle \mathcal{E}_i^2 \rangle]$ for $f_{\Sigma \mathcal{E}^2}$.

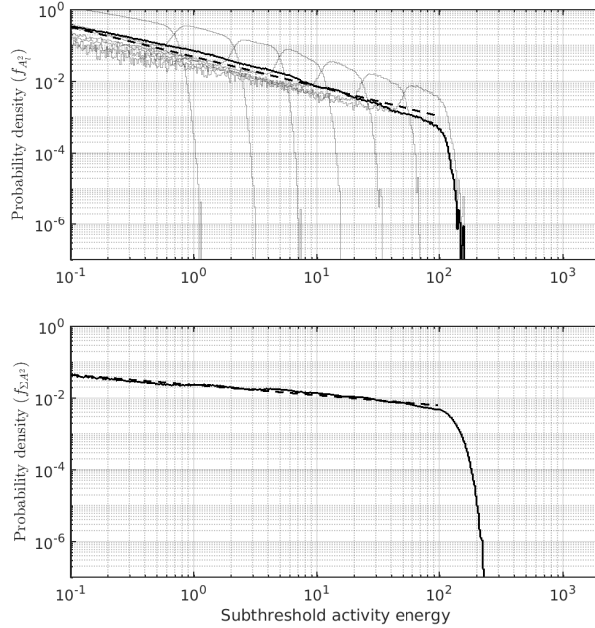


FIG. 17. Density estimates of subthreshold activity energies for $n_l = 7$ levels. Interpretation as in Fig. 16. Both slopes (dashed, top -0.83 , bottom -0.29) were fitted in the range $[10^{-2}, 10^2]$.

the error signal distribution will be biased at the sensory level, and the system will face, in addition to the surprisal characteristic of its environment, a biased noise. For inferential systems that are good enough regulators [17, 18], the Hurst exponent of the input stochastic process should be $H \approx 0.5$ and thus $k \approx 1.5$. This reflects that good regulators expect only unbiased surprisal, which is temporally uncorrelated. Accordingly, Brownian motion is a central component that is added on top of signals in standard models of decision making in neuroscience [156]. For autocorrelated input $H \neq 0.5$, there is a transition at $H \approx 0.75$, beyond which the subthreshold density splits into two disjoint modes (section VB).

The adaptive threshold rule (Eq. 4) enables the PC variables (if there are enough levels) to converge to the rescaled recurrent configuration state (section V; Fig. 9) if the input density is not too heavy-tailed: the tail should have a finite first moment (mean). The reason is that iteratively applying Eq. 4 converges to the mean (section VI G). Approximating the tail with a Pareto distribution $\sim x^{-\alpha}$, this is satisfied if $\alpha > 2$. Under an input density lacking mean (e.g. Cauchy), thresholds would diverge.

L. Subthreshold bistability

Remarkably, the bimodal PC subthreshold activity densities (Fig. 2, 9, in black, note the large probability mass associated to zero is not shown) closely resemble *in vivo* intracellular spontaneous membrane potential shift recordings (anesthetized rat corticostriatal, Fig. 5 in [157]; neo-striatal, Fig. 3 in [158]; cat neocortical pyramidal neurons, Fig. 5 in [159]). Note also that activity densities with positively (negatively) autocorrelated exogenous input (Fig. 12) are conspicuously similar to membrane potential histograms under depolarizing (hyperpolarizing) currents [158] [159]. The membrane potential of cortical neurons responds to synaptic input in a two-state manner [160]. Some neurons toggle between one very hyperpolarized (Down state), and one more depolarized (Up state) membrane potentials [161], where fluctuations around the Up state are of higher amplitude and follow stimulation [160], whereas the Down state is relatively free of noise [161]. Similarly, waiting times between avalanches have a bimodal distribution [102]. The possible coexistence of both SOC and both continuous and discontinuous phase transitions via a cusp bifurcation has been demonstrated by modeling the electrochemical dynamics of synaptic terminals with a few parameters [42], which provides an explanation for up and down states. This behavior has

been construed as an effect of homeostatic regulation [162]. Bistability (in alpha rhythms) has also been proposed to ensue from a (fifth-order branch) subcritical bifurcation in corticothalamic activity dynamics [163]. The PC bimodal density of subthreshold activity in both feedforward and rescaled recurrent loop configurations provides a simple explanation for Up and Down states as the steady state expression of excitable elements that accumulate synaptic input while adjusting the firing threshold to the incoming pulse sizes, which in turn is a manifestation of the trade-off between metabolic power consumption and performance.

VII. CONCLUSION

The perfusive cascade is a toy model of a good regulator [17] that, despite being wholly stripped of the salient behavior of its generative model, displays dynamics characteristic of highly optimized systems that model a complex, multi-scale environment and of brains. Surprisal transport through its stylized hierarchy is near self-similar [164, 165], and leads to scaling laws for all its derived variables. The state units that embody its model of the world are self-dissimilar [43] and are not explicitly modeled, although they enable the assumption that activities at all levels reflect the mismatch between incoming pulses (derived from sensory input) and expectations about the sensory input [27].

Its essential features are lack of adjustable parameters, a universal scaling function in the limit of infinite levels (under weak conditions, section VI K), trade-off between metabolic power consumption and performance, SOC or autovitiation [32], a hierarchy of time scales [31, 119] such that where each level aggregates all brain regions that match its time scale, and bistable subthreshold fluctuations closely resembling intracellular recordings (section VII L). Subthreshold activities and pulses have Lorentzian and flat temporal power spectra, respectively; and their energy can represent surprisal or irreducible uncertainty that is accumulated or relayed between levels, respectively. When using a biological plausible refractory period ($T_0 = 5\text{ms}$) and hierarchy depth ($n_l = 7$ [117]), the resulting PC scaling range 1–85 Hz roughly matches the physiologically relevant brain rhythms. In contrast to other similar models [37][35] that predict a wide range of scaling exponents, the scaling exponent of the PC spectrum ensues from the weighted linear combination of spectra from each level—which can yield any value in the range $[-2, 0]$ —as opposed parameter tuning. These weights are proportional to the number of neurons in each level, which decreases exponentially while

climbing the hierarchy (section VIH). This suggests that temporal scaling patterns found in electrophysiological recordings can be explained as weighted linear combinations of sub-threshold activities and pulses from different hierarchy levels. This setup enables making some predictions pertinent to experimental neuroscience: (1) prediction error neurons (presumably in supragranular layers) that display Up-Down states exist throughout the brain; (2) power spectra of M/EEG traces can display any scaling exponent in the range $[-2, 0]$ (depending on the task and recorded brain area composition) within the frequency band where circuit level neural dynamics unfold (which corresponds roughly to $[0, 100]$ Hz for a refractory period of 5 ms); (3) temporal power spectra scaling exponents are steeper under rest than under stimulation, because (stimuli-driven) error signals have flatter spectra.

The PC bare bones design unavoidably brings about shortfalls and caveats and warrants some skepticism, but it also reveals new appealing research paths. We only examined one adaptive threshold rule that weights mean squared error, but there are other biologically plausible options (section VIG). The simple PC daisy chain topology precluded modeling intra-level effects —e.g. lateral connections between neurons or microcolumns in the same level. Importantly, we focussed on surprisal as irreducible uncertainty, thereby neglecting fluctuations derived from error signals that are successfully suppressed, which are likely to account for a substantial fraction of activity and surprisal in actual good regulators.

Crucially, we left out top-down effects, which are a fundamental aspect of good regulators incorporating hierarchical Bayesian generative models, where the causal asymmetry between top-down modulatory effects and bottom-up driving effects is pivotal to inference and learning [24, 27]. This would lead to back and forth volleys between contiguous levels, and the effect of bottom-up signals would be modulated by supraordinate priors at every level. By shifting the reference or zero value of activity, top-down effects by themselves could suppress discharges (by reconfiguring internal states to accurately predict input, e.g. eureka moment) or encourage them (e.g. under flawed perceptual inference). A top-down signal could set off a surge of activity in subordinate levels, with its size being exponentially related to the rank of the emitting level (section VIH). An expedient course for future work on top-down effects could be explicitly modeling top-down signals that suppress uncertainty in subordinate levels and splitting the time step into the number of hierarchy levels traversed. This could potentially inform the presence of local peaks commonly superimposed on M/EEG power spectra [109] and untangle avalanche clusters due to temporal subsampling [136, 151]

(section VIJ). Finally, allowing PC to accept input before stimulus-evoked cascades end would render it (more) subcritical (section VII).

Making the top level be the only place where energy (suprisal) leaves the system is a crucial design attribute: it forces energy to traverse the whole chain before leaving the system. One interesting accessory feature would be fixing the top level threshold and considering the surprisal quenching at the top level as caused by the action of the system on the environment (note the top level surprisal cannot be suppressed by the effect of supraordinate levels). Then, the PC feedforward configuration would become a metaphor for passive perception under strong priors (as in mind-wandering) and occasional stimulus-driven action. In addition, difficult or surprising situations could be modeled by increasing the input variance, or even its tail shape. There are few alternatives with only bottom-up signals, but when top-down signals are included many plausible variations appear. For instance, the study of PC suggests that the hierarchical coupling of brain levels is essential to its critical behavior, but the switching between transient states characteristic of cognitive dynamics [85, 166, 167] is not explicitly modeled. Allowing to suppress surprisal by acting on the environment (as opposed to only reconfiguring internal states) would provide an explicit mechanism that displays the same sort of itinerant dynamics arising in SOC, synergetics [81], and living creatures [32]. The dichotomy between perception and action is a fundamental design principle of living systems that dictates the architecture of hierarchical brain models through their intimate relationship [100]. However, the implementation of action effectors does not arise from the top level: the time scale of the faster goal-directed motor planning is roughly .1–.5 Hz for humans, which (non casually) corresponds to the time window of the stream of consciousness [168–170]. Hence, the top level associated with action is lower than for perception. In motor control and free-energy formulations of behavior, action is computed via an inverse model [100, 171, 172] that maps sensory prediction errors to actions. Thus, a hierarchy level operating roughly in the theta band, consistent with large theta-cycle avalanches triggering smaller and faster ones [102], is likely to encompass the top level of the inverse model, which would be akin to a “sandbox” used to simulate future courses of action. A candidate for implementing the inverse model is the default mode network. The resting brain evinces large-amplitude spontaneous <0.1 Hz fluctuations in neuromagnetic signals that are temporally correlated across functionally related areas (chiefly medial prefrontal cortex, posterior cingulate cortex, and angular gyrus [173]) that are posited to constitute

a default mode network subserving long term planning, recollection [174–177] and mood [178]. These notions suggest research pathways for how itinerant dynamics emerge from the exploration of the intertwined action-peception space of possibilities and sensory inputs, and how this relates to the trade-off between metabolic power saving and performance.

The analysis of autocorrelated input (section VIK) hints that multifractal analysis [164] could be a useful tool in assessing potential time-varying multiplicative cascading processes underlying dynamics of PC aggregate activity. This is because multifractal analysis can be used to break down a time series of multiplicative interactions that transport information or energy across multiple temporal scales into overlapping contributions derived from a time-varying scaling exponent. Its application to theoretical neuroscience entails “a local threshold dynamic between adjacent neurons that leads to a dissipation of exogenous or afferent stimuli across multiple spatial scales of the nervous system ... This intermittent spatial dissipation ... defines the sensitivity and adaptability of the cognitive system to exogenous perturbations” [165]. This would allow examining the degree of incoming pulses autocorrelation—which are likely to play an important role in the operation of PC-like architectures— at both level-wise and whole system scales.

ACKNOWLEDGMENTS

The article was prepared within the framework of the HSE University Basic Research Program.

Appendix A: Analytical expressions for stationary densities

For $w \equiv w^+ = w^-$, and stationary driving input $I \sim \mathcal{N}(0, 1)$, f_{A_l} is the steady state distribution of subthreshold activity, and post-pulse activity is defined as $\tilde{A}_l = A_l + \mathcal{E}_{l-1}$ (with $\mathcal{E}_0 \equiv I$), we have for $l = 1..L$:

$$f_{\tilde{A}_l} = f_{A_l} * f_{\mathcal{E}_{l-1}}, \quad (\text{A1})$$

$$\begin{aligned} f_{A_l} &= \sum_{i=0}^{\infty} f_{A_l^{(i)}} q_l^{(i)} \prod_{j=0}^{i-1} (1 - q_l^{(j)}) \\ &= f_{A_l^{(0)}} q_l^{(0)} + (1 - q_l^{(0)}) (f_{A_l^{(1)}} q_l^{(1)} + \\ &\quad (1 - q_l^{(1)}) ((f_{A_l^{(2)}} q_l^{(2)} + \dots)), \end{aligned} \quad (\text{A2})$$

where $*$ denotes convolution product [179]. This is reminiscent of an iterative method (Fixed Scale Transformation) devised to study irreversible growth processes [180]. $f_{A_l^{(t)}}$ is the stationary distribution of A_l at iteration number t after the last reset to zero, and $q_l^{(t)} = 1 - \int_{-\theta_l}^{\theta_l} f_{\tilde{A}_l^{(t)}}$. Explicitly, $f_{A_l^{(t)}} = B_{\theta_l}[f_{A_l^{(t-1)}} * f_{\mathcal{E}_{l-1}}]$; in particular, $f_{A_l^{(0)}} = \delta(0)$, where δ is the Dirac delta; $f_{A_l^{(1)}} = B_{\theta_l}[f_{\mathcal{E}_{l-1}}]$, $f_{A_1^{(1)}} = B_{\theta_1}[I]$. For example, for $l = 1$:

$$f_{A_1} = \delta(0)q_1^{(0)} + (1 - q_1^{(0)})(B_{\theta_1}[I]q_1^{(1)} + (1 - q_1^{(1)})(B_{\theta_1}[B_{\theta_1}[I] * I]q_1^{(2)} + \dots)).$$

$q_l^{(0)}$ is the probability of firing consecutively (twice or more), and in general $q_l^{(t)}$ the probability of firing $t + 1$ iterations after the last firing time. In particular, note that $q_l^{(0)} = 1 - \int_{-\theta_l}^{\theta_l} f_{\mathcal{E}_{l-1}}$ would equal on average $1/2$ if activities were reset after every iteration—which would lead to $\langle A_l \rangle = \langle \Theta_l \rangle = \langle \mathcal{E}_{l-1} \rangle$.

The probability $P(\mathcal{E}_l \neq 0) = P(A_l = 0) = P(|\tilde{A}_l| > \Theta_l)$ of unit l firing at any time t (in the limit $t \rightarrow \infty$) is

$$\begin{aligned} P(\mathcal{E}_l \neq 0) &= 1 - \sum_{i=0}^{\infty} q_l^{(i)} \prod_{j=0}^i (1 - q_l^{(j)}) \\ &= \sum_{i=0}^{\infty} [q_l^{(i)}]^2 \prod_{j=0}^{i-1} (1 - q_l^{(j)}) \\ &= [q_l^{(0)}]^2 + (1 - q_l^{(0)}) \cdot \\ &\quad ([q_l^{(1)}]^2 + (1 - q_l^{(1)})(\dots)). \end{aligned} \tag{A3}$$

A coarse estimation of $\langle \Theta_1 \rangle$ using A4, A1 and A2 up to first order approximation—one iteration, till $i = 1$, i.e. ignoring $O(A_1^{(2)})$ terms and above—yields $\langle \Theta_1 \rangle \approx 0.8197$, in reasonable approximation to the numerical simulations. To validate A3, plugging in the $\langle \Theta_1 \rangle$ obtained in simulations and truncating the series at $i = 3$, we get $f_{\mathcal{E}_1}(\mathcal{E}_1 \neq 0) \approx 0.4336$. Table II displays the average activities, thresholds, and pulses or error signals obtained through numerical simulations with $L = 7$ units and $n_t = 9 \cdot 10^5$ iterations and exogenous input distributed as white Gaussian noise.

Solving for f_{Θ_l} would be more laborious—it requires specifying w to solve simultaneously the interlocked pair of equations A2 and 4. However, by the central limit theorem, in the steady state Θ_l converges in distribution to a normal function f_{Θ_l} , for $l = 1, \dots, n_l$. Larger w values induce flatter f_{Θ_l} and f_{A_l} distributions. By Eq. 4, the expectation of the threshold

TABLE II. Numerical estimates of mean subthreshold activities, thresholds, and pulse absolute values. In theory $P(A_l = 0) = P(|A_l + \mathcal{E}_{l-1}| > \Theta_l \mid \mathcal{E}_{l-1} \neq 0) = P(\mathcal{E}_l \neq 0 \mid \mathcal{E}_{l-1} \neq 0) \equiv g_l : \forall l > 1$ should hold because, given a uncorrelated exogenous input, $\mathcal{E}_l^{(t)}$ and $\mathcal{E}_l^{(t+1)}$ must also be uncorrelated. The discrepancies are due to sampling error. Parameters as in Table I.

Level l	$\langle A_l \rangle$	$\langle \Theta_l \rangle$	$\langle \mathcal{E}_l \rangle$	$P(A_l = 0)$
1	0.2309(2)	0.8464	1.4479(8)	.4251(5)
2	0.4782(5)	1.4769	2.2214(14)	.4501(5)
3	0.7408(9)	2.2470	3.2759(29)	.4605(5)
4	1.0686(13)	3.3212(2)	4.8099(60)	.4696(5)
5	1.5937(19)	4.8576(2)	7.0698(131)	.4620(5)
6	2.2914(28)	7.1114(4)	10.3020(282)	.4707(5)
7	3.4148(42)	10.4729(6)	15.2187(606)	.4648(5)

equals the expectation of post-pulse activity $\langle \Theta_l \rangle = \langle |\tilde{A}_l| \rangle$. Thus, if only the expectation $\langle \Theta_l \rangle$ is sought, the calculation of joint densities can be eschewed by calculating $\langle \tilde{A}_l \rangle$ or equivalently by finding the value that on average matches the signs of threshold fluctuations, which numerically can be estimated by minimizing the functional

$$\langle \Theta_l \rangle = \langle |\tilde{A}_l| \rangle \approx \arg \min_{\theta} \left| \langle \tilde{A}_l - \theta \rangle_{\tilde{A}_l > \theta} - \langle \theta - \tilde{A}_l \rangle_{\tilde{A}_l < \theta} \right|, \quad (\text{A4})$$

where $\langle \tilde{A}_l - \theta \rangle_{\tilde{A}_l > \theta} = \int_{\theta}^{\infty} (x - \theta) f_{\tilde{A}_l}(x) dx$, and $\langle \theta - \tilde{A}_l \rangle_{\tilde{A}_l < \theta} = \int_0^{\theta} (\theta - x) f_{\tilde{A}_l}(x) dx$ and $f_{\tilde{A}_l}$ is approximated with its empirical (numerical) distribution. This approximation becomes exact in the limit $w \rightarrow 0$.

Appendix B: Brownian neurons: firing behavior at fine-grained time scales

We have assumed throughout that integrator units discharge only at specific discrete time steps. This trait simulates refractoriness, or the property of being unresponsive to stimuli for a period of time—the refractory period. Neurons are one instance of excitable elements with a refractory period. Nonetheless, it is also interesting to study the case of non-refractory elements or "Brownian neurons", which are continuously responsive and may take in a continuous input. These elements are a kind of stochastic model of neuron membrane

voltage, similar to Stein’s and Orstein-Uhlenbeck’s neuron models [181, 182]. We will focus on excitable behavior as the refractory period $T_0 \rightarrow 0$ approaches zero, that is the scaling limit where a random walk converges to the Wiener process. Note that under the adaptive threshold rule used in the main text, a zero refractory period with a continuous-time process entails a zero threshold, so here instead the threshold will be fixed to some finite value.

1. Firing rate

We proceed to derive bounds and approximations for the discharge rates of the sensory unit and units located far enough from the sensory unit. The firing rate of the sensory unit is the probability that it fires at any time $P(A_1 = 0) = P(\mathcal{E}_1 \neq 0)$, which is given by Eq. A3. As mentioned in Appendix A, the probability of discharging at iteration t is the θ exceedance probability $q_1^{(t)} = 1 - \int_{-\theta_1}^{\theta_1} f_{\tilde{A}_1^{(t)}}$. Since $f_{\tilde{A}_1}$ falls exponentially-like, θ_1 is guaranteed to lie not far from the median of $f_{\tilde{A}_1}$, so the firing rate is guaranteed to remain close to $1/2$, which would not occur if $f_{\tilde{A}_1}$ decayed as a power law [183]. Because of diffusion towards the thresholds, this probability would be lower if the activity \tilde{A}_1 were distributed as white Gaussian noise $\mathcal{N}(0, 1) = W^{(1)}$, and higher as a Wiener process $W^{(t)}$. A tighter upper bound can be further achieved by approximating $\tilde{A}_1^{(t)}$ with the sum of Gaussian input with the activity attained in the limit of infinitely many iterations without firing, namely $\tilde{A}_1^{(t)} \sim \mathcal{N}(0, 1) + \tilde{A}_1^{(\infty)}$, where $\tilde{A}_1^{(\infty)} \sim \mathcal{U}_{[-\theta_1, \theta_1]}$ in $[-\theta, \theta]$ as a result of iteratively applying convolution and truncation. For fixed t , this random variable has lower variance than Brownian motion, but higher than \tilde{A}_1 . In particular, Eq. A3 yields for the sensory unit $P_{\mathcal{N}(0,1)}(\mathcal{E}_1 \neq 0) = .3973 < P_{\tilde{A}_1^{(t)}}(\mathcal{E}_1 \neq 0) = .4251 < P_{\tilde{A}_1^{(\infty)} + \mathcal{N}(0,1)}(\mathcal{E}_1 \neq 0) = .4608 < P_{B^{(t)}}(\mathcal{E}_1 \neq 0) = .5157$.

2. Hitting time density

The hitting time is the random time at which a stochastic process first reaches some target subset of the codomain. For Brownian motion on the real line starting at the origin, the hitting time for the subset $[\theta, \infty)$ follows [184] a Lévy distribution with scale parameter θ^2 , thus $\tau_{\theta_1} = \frac{\theta}{\sqrt{2\pi}} e^{-\theta^2/(2t)} t^{-3/2}$. Its heavy tail falls off as $\sim t^{-3/2}$, and its mean is undefined. However, the problem is essentially changed if the target subset is defined by two flanking

thresholds as $\mathbb{R} \setminus [-\theta, \theta]$. Then $\tau_\theta = \min \{t \geq 0 : W^{(t)} = \theta\}$, which is the same as the first exit time from $[-\theta, \theta]$. If we assume no reset, the first exit time of A_1 from $[-\theta_1, \theta_1]$ (or first hit time of its complement interval) would be the same as the hitting time of θ_1 for reflected Brownian motion $|W|$ (RBM). The RBM expected value is $\langle |W^{(t)}| \rangle = \sqrt{2t/\pi}$ (from the Wiener process transition density function with origin at zero $f_{W^{(t)}}(x) = \frac{1}{\sqrt{2\pi t}} e^{-\frac{x^2}{2t}}$ [184]), so we expect the threshold $\langle |W^{(t_1)}| \rangle = \theta_1$ is attained at time $t_1 = \frac{\pi}{2}\theta_1^2$. Thus, if $\tilde{A}_1 \sim |W|$, we would expect reaching the threshold $\theta_1 = \sqrt{2/\pi}$ on average at $t_1 = 1$. However, the actual values are $t_1 = 1.125$ and $\theta_1 = .8464$ because leftover activity from quiescent trials and the threshold updating rule (Eq. 16) push the threshold upwards.

The first exit time for \tilde{A}_1 can be calculated as the weighted sum of each time step by its firing probability; simulations yield $\langle \tau_{\pm\theta_1} \rangle = 1.655$. In contraposition, the expected hitting time or residence time for RBM is

$$\langle \tau_{\pm\theta} \rangle = \theta^2, \quad (\text{B1})$$

which can be derived from the knowledge that $(W^{(t)})^2 - t$ is a martingale [62]). For $\theta_1 = .8464$ (see above) this gives $\langle \tau_{\pm\theta_1} \rangle = .7164$. This discrepancy (a factor of ≈ 2.31) is due to the discretization of allowed firing times imposed by the existence of a refractory period $T_0 = 1 > \langle \tau_{\pm\theta_1} \rangle$: the discrepancy is roughly the fraction of energy "skipping the threshold during the refractory period", which coincides with the inverse of the gain $g_1^{-1} \approx 2.35$ (see Table I to look up g_1).

We could stop here, but in pursuance of getting a comprehensive picture of the dynamics of integrator units in the limit of non-refractoriness, let us derive the RBM hitting time density $f_{\tau_{\pm\theta}}$. The reflection principle [62], which stands on the observation that the distribution of future paths is symmetric at any given time, relates the running maximum of a Wiener process up to time t to its tail distribution at time t [185]. In turn, the running maximum is equal to the cumulative distribution of the hitting time $F_{\tau_{\pm\theta}}(t) = P(\tau_{\pm\theta} \leq t)$ [184], so

$$P(\tau_{\pm\theta} \leq t) = P(\max_{0 \leq u \leq t} W^{(u)} \geq \theta) = 2P(W^{(t)} > \theta).$$

This can also be applied to calculate the hitting time of RBM, but some caution is called for. The idea is to use the reflection principle iteratively on the thresholds $-\theta$ and θ . The RBM hitting time is the first exit time from the $[-\theta, \theta]$ stripe: $\tau_{\pm\theta} = \min \{t : W^{(t)} \notin [-\theta, \theta]\}$. As in Brownian motion, when a particle first reaches the threshold θ , it carries on outwards or reverts with the same probability (by symmetry, the same reasoning applies to particles

attaining first $-\theta$). Hence, $P(\max_{0 \leq u \leq t} |B^{(u)}| \geq \theta) = 2P(|W^{(t)}| > \theta)$ as long as paths do not travel further than 2θ from the first hit, i.e., if $|B^{(t)}| < 3\theta$. Beyond this point, some of the reverting paths will attain the opposite threshold $-\theta$. To exclude the contribution from virtual paths that hit thresholds more than once, we have to remove the path densities located in $[(4k-1)\theta, (4k+1)\theta]$ for $k \in \mathbb{Z}$ —these are the odd-numbered interleaved stripes, resulting from iteratively reflecting the $[-\theta, \theta]$ stripe over the thresholds [186]. This ensures we count only paths that hit at least one of the thresholds, and not paths hitting multiple times. To sum up,

$$\begin{aligned}
F_{\tau_{\pm\theta}}(t) &= P(\tau_{\pm\theta} \leq t) = P(\max_{0 \leq u \leq t} |W^{(u)}| \geq \theta) \\
&= \int_{-\theta}^{\theta} P(|W^{(t)}| > \theta) dy \\
&= \int_{-\theta}^{\theta} \sum_{k \in \mathbb{Z}} 2f_{W^{(t)}}(y + (4k+2)\theta) dy \\
&= \sum_{k \in \mathbb{Z}} 2 \int_{-\theta}^{\theta} \frac{1}{\sqrt{2\pi t}} e^{-\frac{(y+(4k+2)\theta)^2}{2t}} dy \\
&= \sqrt{\frac{2}{\pi t}} \sum_{k \in \mathbb{Z}} \int_{(4k+1)\theta}^{(4k+3)\theta} e^{-\frac{x^2}{2t}} dx \\
&= \sum_{k \in \mathbb{Z}} \operatorname{erf}\left(\frac{(4k+3)\theta}{\sqrt{2t}}\right) - \operatorname{erf}\left(\frac{(4k+1)\theta}{\sqrt{2t}}\right),
\end{aligned} \tag{B2}$$

where we performed the change of variables $x = y + (4k+2)\theta$, and the error function erf takes $\frac{x}{\sqrt{2t}}$ as variable. This is equivalent to the generalized reflection principle formula [187]: $P(\max_{0 \leq u \leq t} |W^{(u)}| \leq \theta) = \sum_{k \in \mathbb{Z}} f_{W^{(t)}}(y + 4k\theta) - f_{W^{(t)}}(y + (4k+2)\theta) = 1 - P(\max_{0 \leq u \leq t} |W^{(u)}| > \theta)$. Finally, differentiating $P(\tau_{\pm\theta} \leq t)$ returns the hitting time density:

$$\begin{aligned}
f_{\tau_{\pm\theta}}(t) &= \frac{d}{dt} P(\tau_{\pm\theta} \leq t) \\
&= \sum_{k \in \mathbb{Z}} \frac{d}{dt} \left(\operatorname{erf}\left(\frac{(4k+3)\theta}{\sqrt{2t}}\right) - \operatorname{erf}\left(\frac{(4k+1)\theta}{\sqrt{2t}}\right) \right) \\
&= \frac{\theta}{\sqrt{2\pi t^3}} \sum_{k \in \mathbb{Z}} (4k+1) e^{-\frac{\theta^2(4k+1)^2}{2t}} - (4k-1) e^{-\frac{\theta^2(4k-1)^2}{2t}} \\
&= \frac{\theta}{\sqrt{2\pi t^3}} \sum_{k \in \mathbb{Z}} (-1)^k (2k+1) e^{-\frac{\theta^2(2k+1)^2}{2t}} \\
&= \frac{\theta\sqrt{2}}{\sqrt{\pi t^3}} \sum_{k=0}^{\infty} (-1)^k (2k+1) e^{-\frac{\theta^2(2k+1)^2}{2t}}
\end{aligned} \tag{B3}$$

Alternatively to Eq. B3, $f_{\tau_{\pm\theta}}$ can be calculated from the moment-generating function of $f_W(t)$, which can be derived from the properties of martingales. It can be shown that $e^{\sigma W(t) - \frac{\sigma^2}{2}t}$ is a martingale [62]. Then, for a Wiener process starting at the origin, it holds $\langle e^0 \rangle = \langle \exp(\sigma W(\min(\tau_{+\theta}, \tau_{-\theta})) - \frac{\sigma^2}{2} \min(\tau_{+\theta}, \tau_{-\theta})) \rangle$, so $1 = \frac{1}{2} \langle \exp(\sigma\theta - \frac{\sigma^2}{2}\tau_{\pm\theta}) + \exp(-\sigma\theta - \frac{\sigma^2}{2}\tau_{\pm\theta}) \rangle$, and rearranging $\langle e^{-\frac{\sigma^2}{2}\tau_{\pm\theta}} \rangle \frac{e^{\sigma\theta} + e^{-\sigma\theta}}{2} = 1$. After the change of variables $\sigma = \sqrt{2\theta}$, we get an expression for the Laplace transform of the hitting time density [62]

$$\langle e^{-s\tau_{\pm\theta}} \rangle = \operatorname{sech} \theta\sqrt{2s}$$

Its inverse Laplace transform $\mathcal{L}^{-1}\{\operatorname{sech} \theta\sqrt{2s}\}(t) = \frac{1}{2\pi i} \lim_{R \rightarrow \infty} \int_{c-iR}^{c+iR} \frac{e^{st} ds}{\cosh \theta\sqrt{2s}}$ is the hitting time density $f_{\tau_{\pm\theta}}(t)$, with $c \in \mathbb{R}$ such that the real part of any of the singularities of the integrand is less than c . Cauchy's residue theorem allows to compute the line integral of an analytic function g over a closed rectifiable curve Γ in terms of the function's residues [188]. Let $g(s) = \frac{e^{st}}{\cosh \theta\sqrt{2s}}$ be the integrand, and $\Gamma = C \cup \gamma$, where $\gamma = [c - iR, c + iR]$ is the line integral we wish to calculate, and $C = c + Re^{i\varphi} : \varphi \in [\frac{\pi}{2}, \frac{3\pi}{2}]$ is the arc of the semicircle with center c and radius R . Then, the residue theorem states that $\oint_{\Gamma} g = \int_{\gamma} g + \int_C g = 2\pi i \sum_k \operatorname{Res}(g, s_k)$, where s_k are the poles of g located inside Γ . Hence, letting the radius R of the semicircle Γ grow to infinity,

$$\frac{1}{2\pi i} \lim_{R \rightarrow \infty} \int_{c-iR}^{c+iR} g = \sum_k \operatorname{Res}(g, s_k) - \frac{1}{2\pi i} \lim_{R \rightarrow \infty} \int_C g. \quad (\text{B4})$$

Since e^{st} is an entire function, the poles s_k of g are the zeroes of $\cosh \theta\sqrt{2s}$, which are defined by $\cosh \theta\sqrt{2s_k} = 0$; this yields the distinct poles $s_k = -\frac{\pi^2}{8\theta^2}(2k+1)^2$, with $k \in \mathbb{N}_0$; seeing that all poles satisfy $s_k < 0$, we can take $c = 0$. We can evaluate the second term of the r.h.s. of Eq. B4 through an approach akin to that of Jordan's lemma [188], i.e., by finding an upper bound to the contour integral modulus

$$\begin{aligned} \left| \int_C g \right| &\leq \int_C |g| = \int_{\frac{\pi}{2}}^{\frac{3\pi}{2}} \left| \frac{e^{tR(\cos \varphi + i \sin \varphi)} R i e^{i\varphi}}{\cosh(\theta\sqrt{2R}e^{i\varphi/2})} \right| d\varphi \\ &= R \int_{\frac{\pi}{2}}^{\frac{3\pi}{2}} \frac{e^{tR \cos \varphi}}{|\cosh(\theta\sqrt{2R}e^{i\varphi/2})|} d\varphi \\ &\leq 2R \int_{\frac{\pi}{2}}^{\frac{3\pi}{2}} e^{tR \cos \varphi} d\varphi, \end{aligned}$$

which has limit zero as $R \rightarrow \infty$ because $\cos \varphi \leq 0$ for $\varphi \in [\frac{\pi}{2}, \frac{3\pi}{2}]$. The last step requires calculating $\max_{\varphi \in [\frac{\pi}{2}, \frac{3\pi}{2}]} |\cosh(\theta\sqrt{2R}e^{i\varphi/2})|^{-1} = \max_{\varphi \in [\frac{\pi}{2}, \frac{3\pi}{2}]} 2|\cosh(2\theta\sqrt{2R} \cos \frac{\varphi}{2})|^{-1}$

$\cos(2\theta\sqrt{2R}\cos\frac{\varphi}{2})|^{-2} = 2$, which is achieved for $\varphi = \pi$. Consequently,

$$f_{\tau_{\pm\theta}} = \frac{1}{2\pi i} \lim_{R \rightarrow \infty} \int_{-iR}^{iR} g = \sum_k \text{Res}(g, s_k).$$

Since $\frac{d}{ds} \cosh \theta\sqrt{2s}|_{s=s_k} = \frac{\theta}{\sqrt{2s_k}} \sinh \theta\sqrt{2s_k} = \frac{\theta^2}{\frac{\pi}{2}(2k+1)} \sin \frac{\pi}{2}(2k+1) \neq 0$, all poles ($\forall k \in \mathbb{N}^0$) are simple and isolated. Hence, $\frac{e^{st}}{\cosh \theta\sqrt{2s}}$ is a meromorphic function (except at infinity), and it can be expanded —Mittag-Leffler’s theorem— around each of its poles s_k as a sum of partial fractions, where each partial fraction expansion is the principal part of $\text{sech } \theta\sqrt{2s}$ at the pole s_k [188]. The residue at pole s_k is thus

$$\begin{aligned} \text{Res}(g, s_k) &= \lim_{s \rightarrow s_k} (s - s_k)g(s) \\ &= \frac{e^{s_k t}}{\frac{\theta^2}{\frac{\pi}{2}(2k+1)} \sinh \theta\sqrt{2s_k}} \\ &= \frac{\frac{\pi}{2}(2k+1)}{\theta^2} \frac{e^{-\frac{\pi^2}{8\theta^2}(2k+1)^2 t}}{\sin \frac{\pi}{2}(2k+1)} \\ &= \frac{\pi}{2\theta^2} (2k+1)(-1)^k e^{-\frac{\pi^2}{8\theta^2}(2k+1)^2 t}. \end{aligned}$$

Finally, by the residue theorem

$$f_{\tau_{\pm\theta}}(t) = \frac{\pi}{2\theta^2} \sum_{k=0}^{\infty} (-1)^k (2k+1) e^{-\frac{\pi^2}{8\theta^2}(2k+1)^2 t}. \quad (\text{B5})$$

Numerical simulations show that Eq. B3 converges much faster than Eq. B5 for $t \ll 1$, and vice versa for $t \gg 1$. We can use Eq. B5 to calculate the expected hitting time τ_W of a Brownian neuron, with threshold θ_1 , where firing of sensory units is possible only at specific times separated by $T_0 = 1$, as $\langle \tau_W \rangle = \sum_{k \in \mathbb{Z}^+} k \frac{f_{\tau_{\pm\theta}}(k)}{\sum_{i \in \mathbb{Z}^+} f_{\tau_{\pm\theta}}(i)} = 1.21756$, which lies between the values of $\langle \tau_{\theta_1} \rangle$ for RBM and the sensory unit. Importantly, this shows that the hitting time density of Brownian neurons has an exponentially decaying tail.

3. Brownian neurons mimicking refractory units: reduced variance and noisy relaxation processes

One could ask: how to tinker with Brownian neurons so they reproduce the firing rates and mean hitting times of discrete (sensory unit) neurons? For mean hitting times, perhaps the simplest way is reducing the variance of the Brownian neuron. Picking up the calculation of appendix B ($(B^{(t)})^2 - t$ is a martingale), we can derive the standard deviation of the

Brownian neuron that equates its mean hitting time to that of the sensory unit as $\sigma_{\text{red}} = \theta_1 / \sqrt{\langle \tau_1 \rangle} = .6579$.

For firing rates, we can counterpoise the discrepancy between Brownian and sensory units by adding a zero-reverting term to the Brownian neuron transition density, thus rendering it a noisy relaxation or (driftless) "Ornstein-Uhlenbeck neuron". This mimics the activity resetting effect of discharges (cf. Eq. 2). The problem now is to find the mean-reverting coefficient ρ of the stochastic differential equation

$$dx = -\rho x dt + dW$$

obeyed by the Ornstein-Uhlenbeck neuron that matches the firing rate of the sensory unit $P_{\tilde{A}_1^{(t)}}(\mathcal{E}_1 \neq 0)$. Numerical optimization of ρ with respect to its transition density [184] yields $\rho = .2819$, which compared to 0 stands for the influence of discharge-induced suppression on the dynamics of \tilde{A}_1 .

Appendix C: Dynamics of thresholds, pulses, and activities

Threshold dynamics can be described with an AR(1) model. Recalling Eq. 4, and assuming $w = w^+ = w^-$:

$$\begin{aligned} \theta^{(t+1)} &= (1 - w)\theta^{(t)} + w|\tilde{a}^{(t)}| \\ &= w\langle \Theta \rangle + (1 - w)\theta^{(t)} + \tilde{\epsilon}^{(t)} \end{aligned} \quad (\text{C1})$$

where $w\langle \Theta \rangle$ is the average, $1 - w$ is the regressor parameter, and $\tilde{\epsilon}^{(t)} = w(|\tilde{a}^{(t)}| - \langle \Theta \rangle)$ is a white noise process with zero mean and variance $\sigma_{\tilde{\epsilon}}^2 = w^2 \text{var} |\tilde{A}|$. The l subscripts have been omitted for clarity. For $1 - w \approx 1$, this constitutes a wide-sense stationary process and the central limit theorem ensures that—in the steady state— Θ is approximately Gaussian-distributed, with mean $\langle \Theta \rangle$ and covariance $C_{\theta, \theta}(n) \equiv \text{cov} [\theta^{(t+n)}, \theta^{(t)}] = \frac{\sigma_{\tilde{\epsilon}}^2}{1 - (1 - w)^2} (1 - w)^{|n|} = \frac{w^2 \text{var} |\tilde{A}|}{1 - (1 - w)^2} (1 - w)^{|n|} \approx \frac{\text{var} |\tilde{A}|}{2} w (1 - w)^{|n|} = \frac{\sigma_{\tilde{\epsilon}}^2}{2w} (1 - w)^{|n|}$, whence

$$C_{\theta, \theta}(n) \approx \frac{\sigma_{\tilde{\epsilon}}^2}{2w} (1 - w)^{|n|}, \quad (\text{C2})$$

where the approximation is valid for small w [189]. $C_{\theta, \theta}(n)$ decays with a time constant $-T_s / \log(1 - w) \approx T_s / w$ ($T_s = T_l$ sampling period) [190]. Notice that we set different sampling periods $T_s = T_l = \nu_{l-1}^{-1}$ corresponding to each level $l = 1 \dots 7$ (with $\nu_0^{-1} = T_0$),

because thresholds can be updated only upon arrival of pulses, so the firing rate of preceding units determines the threshold updating rate at each level. Since $\tau \gg T_l$ for small w , we can calculate the power spectrum through the Fourier transform [191] of the (continuum approximation) covariance:

$$\begin{aligned}
S_{\theta,\theta}(\nu|l) &= \frac{\sigma_{\tilde{\epsilon}}^2}{1 - (1-w)^2 \tau^{-2} + (2\pi\nu)^2} \frac{2\tau^{-1}}{1 - (1-w)^2 \tau^{-2} + (2\pi\nu)^2} \\
&\approx \frac{w^2 \text{var} |\tilde{A}|}{2w} \frac{2w/T_l}{w^2/T_l^2 + (2\pi\nu)^2} \\
&= \text{var} |\tilde{A}| \frac{T_l}{1 + \left(\frac{T_l}{w} 2\pi\nu\right)^2}, \tag{C3}
\end{aligned}$$

which is a Lorentzian function, with maximum $S_{\theta,\theta}(0) = T_l \text{var} |\tilde{A}|$ at $\nu = 0$ and corner frequency $\gamma_\theta = \frac{w}{2\pi T_l}$. The corner frequencies for each unit firing period are shown in Table III. Note that the time resolution at each level $T_s = T_l$ decreases with the level number, reflecting the slower dynamics of later units.

The continuous-time analogue of the AR(1) process in Eq. C1 is a Ornstein-Uhlenbeck process (OUP) with mean $\langle \Theta_l \rangle$, mean-reversal term $-w$, and noise variance $\sigma_{\tilde{\epsilon}}$. This can be deduced by rearranging Eq. C1 as $\theta_l^{(t)} = \theta_l^{(t-1)} - w(\theta_l^{(t-1)} - \langle \Theta_l \rangle) + \tilde{\epsilon}^{(t)}$ and taking the limit as the step size approaches zero:

$$d\theta = -w(\theta - \langle \Theta \rangle)dt + \sigma_{\tilde{\epsilon}}dW. \tag{C4}$$

Donsker's invariance principle guarantees that the random walk series of $\tilde{\epsilon}^{(t)}$ increments $\lim_{n \rightarrow \infty} \frac{1}{\sqrt{n}} \sum_{i=1}^{nt} \tilde{\epsilon}^{(i)}$ converges in distribution to $\sigma_{\tilde{\epsilon}} W(t)$ for $t \in [0, 1]$, where $W(t)$ is the standard Wiener process. This corresponds to the scaling limit $T_s \rightarrow 0$ of the discrete AR(1) process in Eq. C1. When T_s is not negligible, Eq. C4 is no longer a good approximation and it has to be corrected with additional factors that depend on the step size. In the steady state, the OUP covariance function [184] is $\text{cov} [\theta^{(t+u)}, \theta^{(t)}] = \frac{\text{var} |\tilde{A}|}{2} w e^{-wu} = \frac{\sigma_{\tilde{\epsilon}}^2}{2w} e^{-wu}$, which for $w \rightarrow 0$ approaches the covariance function of the discrete AR(1) process (Eq. C2). Numerical simulations with $w = 0.01$ yielded $\sigma_{|\tilde{A}|} \equiv \sqrt{\text{var} |\tilde{A}|} \approx 0.53 \langle \Theta_l \rangle$ for $l \geq 3$ (Table III) [192]. This gives the following reasonable continuum approximation to the threshold dynamics for $l \geq 3$:

$$\frac{1}{w} d\theta \approx -(\theta - \langle \Theta \rangle)dt + 0.53 \langle \Theta \rangle dW. \tag{C5}$$

The solid curves in Fig. 3 are derived from Eq. C5, except the noise variances from Table III were used instead of 0.53.

TABLE III. Numerical estimates of steady state threshold dynamics noise variance components $\sigma_{|\tilde{A}_l|}$ normalized by the average threshold; and corner frequencies $\gamma_{\theta,l}$ and $\gamma_{a,l}$ (time series of length $n_t = 9 \cdot 10^6$).

Level l	$\frac{\sigma_{ \tilde{A}_l }}{\langle \Theta_l \rangle}$	$\frac{\sigma_{ \mathcal{E}_l }}{\langle \mathcal{E}_l \rangle}$	$\gamma_{\theta}(l)$ (Hz)	$\gamma_a(l)$ (Hz)
1	.7557	.3493	.318	59.2
2	.5664	.2576	.135	19.5
3	.5393	.2491	.061	8.41
4	.5301	.2421	.028	3.85
5	.5395	.2419	.013	1.80
6	.5253	.2425	.006	0.82
7	.5452	.2411	.003	0.38

Computing the power spectral density (PSD) using the discrete Fourier transform on windowed finite time series entails unavoidably an estimation bias. This is because using a finite-length signal is equivalent to multiplying the original infinite-length signal by a window function, and the frequency response of a finite window (Fejér’s kernel) is not just a Dirac delta, but a distribution with a finite-sized mainlobe and many tailing off sidelobes which nevertheless spread out to cover the whole frequency range [193]. As a result, the estimate of a windowed signal has power leaked into all frequencies around any true signal frequency. This effect is called spectral leakage, and it affects the periodogram and its derivatives such as Welch’s method typically biasing PSD estimates upwards [193] (however, flat spectrum or white noise signals are not affected). In particular, the high frequency power of AR(1) models doesn’t decay as a power law —as it does for the continuous OUP— because these frequencies correspond to trial-by-trial changes, that cannot vanish in discrete implementations. In general, on top of estimation bias, there is always a trade-off between variance reduction and resolution when estimating PSDs. Using Welch’s method with a (rectangular) window length $n_w = 10^5$, the squared Fejér’s kernel has a peak mainlobe of 10^{10} and its largest sidelobes peak at about 27dB below it —at a distance of $f_s/n_w \approx 10^{-3}$ Hz, the lowest resolvable frequency. In Fig. 3, we can observe that spectral leakage inflates the PSD at the lowest and highest frequencies —the PSD cannot be estimated at the lowest frequencies (10^{-3} Hz) due to the loss of resolution attending the improvement in variance afforded by Welch’s

method. To verify that the bias is due to spectral leakage, we also estimated PSDs using the computationally expensive Thompson’s multitaper method (not shown), which uses a bank of optimal bandpass filters called Slepian sequences (instead of a bank of rectangular bandpass filters as in Welch’s method) that reduces Fejér’s kernel’s sidelobes. For a time-bandwidth parameter 3, the bias is substantially reduced at both lowest and highest frequencies —although at the expense of higher variance.

The PSD of a sum of signals is the sum of the signals’ PSDs only if the signals are uncorrelated. Otherwise, $S_{\theta_i+\theta_j}(\nu) = S_{\theta_i,\theta_i}(\nu) + S_{\theta_j,\theta_j}(\nu) + 2 \operatorname{Re}(S_{\theta_i,\theta_j}(\nu))$, where $S_{\theta_i,\theta_j}(\nu)$ is the cross power spectral density (CPSD). Hence, estimating the PSD of $\sum_{i=1}^L \theta_i^{(t)}$ in general requires computing numerically $L(L-1)/2 = 21$ pairwise CPSD functions for $L = 7$, with no closed-form expression. However, a reasonable approximation can be achieved computing only the CPSD function that contributes the highest power: $S_{\sum_{i=1}^7 \theta_i}(\nu) \approx \sum_{i=1}^7 S_{\theta_i,\theta_i}(\nu) + 2 \operatorname{Re}(S_{\theta_6,\theta_7}(\nu))$. Inspection of the PSD of the sum of variables in Figs. 3 and 4 reveals that pulses ε_l have pairwise CPSD components that contribute to the CPSD of the sum only at low frequencies. This is confirmed by their close to 1 coherence estimates and zero-lag cross-phase (Fig. 18).

The dynamics of the activity variables $a_l^{(t)}$ follows a random walk with stationary and independent increments distributed as $\varepsilon_l^{(t)}$ that resets to zero upon exiting $[-\theta_l, \theta_l]$. Rewriting Eq. 2:

$$a_l^{(t)} = (a_l^{(t-1)} + \varepsilon_{l-1}^{(t)}) \mathbb{1}_{a_l^{(t-1)} + \varepsilon_{l-1}^{(t)} \in [-\theta_l, \theta_l]}, \quad (\text{C6})$$

where $\mathbb{1}_x$ is the indicator function, which equals zero when its argument x is false and one when true, and $\theta_l = \theta_l^{(t)}$ is also a function of t . In general, subthreshold activity can be modeled as a Markov renewal process with discrete discharge times t , inter-event times $\nu_{a,l-1}^{-1}$ that equal the inverse of the firing rate of the preceding unit, and activity as a continuously valued state A_l , where the jumps are the incoming pulses from the preceding unit \mathcal{E}_{l-1} . Alternatively, it can be construed as a discrete version of Brownian motion with stochastic resetting [194]: since $\varepsilon^{(t)}$ has a well defined variance, in the scaling limit $a_l^{(t)}$ behaves as a Brownian particle that resets to zero as soon as it exits $[-\theta_l, \theta_l]$, so Eq. C6 becomes:

$$da = \sigma_{\mathcal{E}} dW \quad \text{if } a \in [-\theta, \theta], \quad (\text{C7})$$

and $a = 0$ otherwise, with $\sigma_{\mathcal{E}}$ the standard deviation of \mathcal{E} .

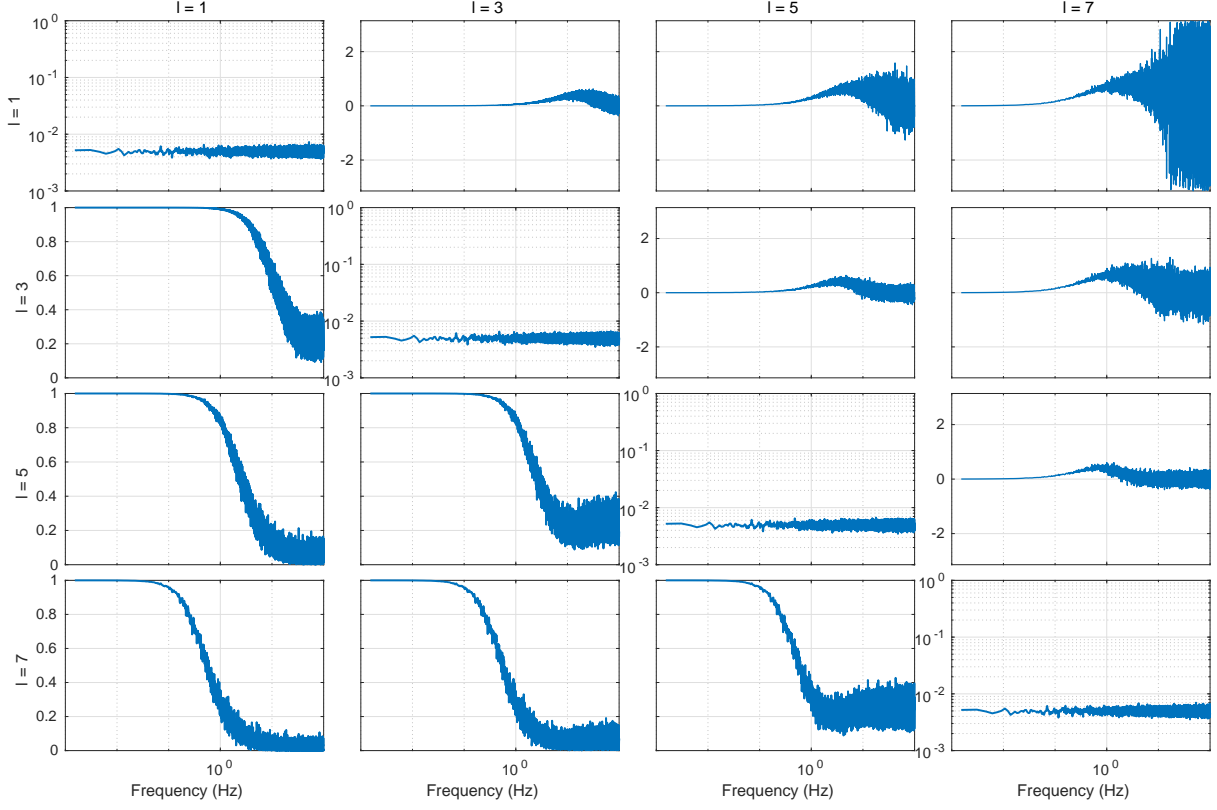


FIG. 18. Cross-spectral phase (cells above the main diagonal) and magnitude-squared coherence (below the main diagonal) pair-wise estimates between pulses $\varepsilon_l^{(t)}$, $l = 1, 3, 5, 7$. The main diagonal is populated by the PSD, as in Fig. 6. The cross-spectral phase was defined as the argument of the cross-spectral density $S_{\varepsilon_i, \varepsilon_j}$; and the magnitude-square coherence was defined as $\frac{|S_{\varepsilon_i, \varepsilon_j}|^2}{S_{\varepsilon_i} S_{\varepsilon_j}}$, with PSD estimation parameters set as in Fig. 3.

It can be shown [195] that the covariance function $C_{a,a}(t_1, t_2)$ of the process $a^{(t)}$ with stochastic reset can be expressed in terms of the covariance function of the same process without reset—which is a Wiener process scaled by σ_{ε_0} — $\sigma_{\varepsilon_0}^2 C_{W,W}(t_1, t_2)$, with $t_2 > t_1$, as $C_{a,a}(t_1, t_2) = P(\tau > t_2 - t_1) \left[\int_0^{t_1} P(\tau < t') P(t' < \tau < t' + dt') \sigma_{\varepsilon_0}^2 C_{W,W}(t', t_2 - t_1 + t') + P(\tau > t_1) \sigma_{\varepsilon_0}^2 C_{W,W}(t_1, t_2) \right]$ where τ is used to denote $\tau_{\pm\theta}$ for clarity. Since the activity process without reset becomes a Wiener process in the scaling limit, $C_{W,W}(t_1, t_2) = \min(t_1, t_2) = t_1$, and in the steady state $P(\tau > t_1) C_{W,W}(t_1, t_2) = \bar{F}_\tau(t_1) t_1 \rightarrow 0$ as $t_1 \rightarrow \infty$, so we obtain

$$C_{a,a}(t_1, t_2) = \bar{F}_\tau(t_2 - t_1) \int_0^{t_1} F_\tau(t') f_\tau(t') \sigma_{\varepsilon_0}^2 t' dt', \quad (\text{C8})$$

where $\bar{F}_\tau(t) = 1 - F_\tau(t)$ is the tail distribution of τ , and $\sigma_{\varepsilon_0}^2 = 2D$ is just twice the diffusivity parameter D used in diffusion problems. There is no closed-form expression for this equation

that we know of, so we shall approximate it.

Repeated firing or discharging can be modeled as a renewal process, which involves ignoring the activity values and focusing only on the accumulated number of discharges $N(t)$ at each iteration t , where the jumps are resets to zero. The inter-event times (the duration between successive discharges) are distributed as the first exit time f_τ (Eq. B3 or B5). Although the probability of firing in a given time interval depends on the last discharge time, this dependency vanishes when averaging over long time spans. By the elementary renewal theorem [184], the number of discharges is asymptotically linear, i.e. in the long run $t \rightarrow \infty$ the averaged firing frequency approaches the inverse of the hitting time mean:

$$\lim_{t \rightarrow \infty} \langle \nu \rangle \equiv \lim_{t \rightarrow \infty} \frac{1}{t} \langle N(t) \rangle = \langle \tau \rangle^{-1} = \theta^{-2}, \quad (\text{C9})$$

where the last equality follows from Eq. B1. Since the inverse is a convex function, by Jensen's inequality the expectation of the inverse is larger or equal than the inverse of the expectation: $\langle \nu \rangle = \langle \tau^{-1} \rangle \geq \langle \tau \rangle^{-1}$, which indicates that θ^{-2} is also a lower bound of the average firing rate. For large t the asymptotic variance of $N(t)$ behaves [184] according to

$$\lim_{t \rightarrow \infty} \frac{\text{var}[N(t)]}{t} = \frac{\text{var}[\tau]}{\langle \tau \rangle^3} = \frac{2}{3} \theta^{-2}, \quad (\text{C10})$$

where in the rightmost equality we used $\text{var}[\tau_{\pm\theta}] = \frac{2}{3} \theta^4$, which can be derived from the properties of martingales [62] in a similar manner to Eq. B1. Together with Eq. C9, this determines the magnitude of the fluctuations of inter-firing times about their expectation θ^{-2} ; these fluctuations are approximately normally distributed [184].

From the density of first exit times, we can deduce the probability that a unit fires with rate $r = t^{-1}$ from $f_\tau(t)dt = f_\nu(r)dr$. Thus, the sequence of firing times can be interpreted as a inhomogeneous Poisson point process over t with rate intensity function $r f_\tau(t)$ (cf. Eq. B5). Hence the probability that the activity fires or reaches the threshold n times within a segment $[0, t]$ starting from the previous reset at zero time is

$$P(\text{firing } n \text{ times}) = \frac{[\Lambda(t)]^n}{n!} e^{-\Lambda(t)},$$

where $\Lambda(t) = \int_0^t \tau^{-1} f_\tau(\tau) d\tau = \langle t^{-1} \rangle$ before the first discharge, but as $t \rightarrow \infty$, by the elementary renewal theorem $\Lambda(t) \rightarrow \langle \tau \rangle^{-1} t = rt$.

Thus, by neglecting short time correlations, the elementary renewal theorem furnishes a simple approximation to the firing rate. This effectively amounts to construing repeated

firing as a Poisson point process with rate $r = \theta^{-2}$. By considering the inter-event times of $a^{(t)}$ as a (homogeneous) Poisson process with constant resetting rate, we can derive again (cf. Eq. C8) the covariance function of $a^{(t)}$ in terms of the covariance function of Brownian motion [195] by substituting F_τ for its homogeneous counterpart as

$$\begin{aligned}
C_{a,a}(t_1, t_2) &\approx e^{-r(t_2-t_1)} \int_0^{t_1} r e^{-rt'} \sigma_{\varepsilon}^2 t' dt' \\
&= r \sigma_{\varepsilon_0}^2 e^{-r(t_2-t_1)} \int_0^{t_1} t' e^{-rt'} dt' \\
&= \frac{\sigma_{\varepsilon_0}^2}{r} e^{-r(t_2-t_1)} [1 - e^{-rt_1} (rt_1 + 1)] \\
&\underset{t_1 \rightarrow \infty}{=} \frac{\sigma_{\varepsilon_0}^2}{r} e^{-r(t_2-t_1)}, \tag{C11}
\end{aligned}$$

where, in the first line, the first factor is the probability that there is no reset between t_1 and t_2 (Eq. C with $n = 0$); and the integrand denotes the probability that the last reset before t_1 occurs between t' and $t' + dt'$ [195]. Note that this approximated covariance function is stationary only if fluctuations around the expectation are ignored (from the elementary renewal theorem). These fluctuations introduce a bias, but we can alleviate it by making use of Eq. C10 and taking the expectation of Eq. C11 with respect to the approximately normally distributed r :

$$C_{a,a}(t) \approx \sigma_{\varepsilon_0}^2 \left\langle \frac{e^{-r|t|}}{r} \right\rangle \approx \theta^2 \sigma_{\varepsilon_0}^2 e^{-\frac{4}{3}\theta^{-2}|t|}, \tag{C12}$$

where $t = t_2 - t_1$ (when $t_2 > t_1$); we approximated $\langle r^{-1} \rangle \approx \langle r \rangle^{-1}$; we used $r = \langle \nu \rangle \approx \mathcal{N}(\theta^{-2}, \frac{2}{3}\theta^{-2})$ from Eqs. C9 and C10; and $\langle e^{\mathcal{N}(\theta^{-2}, \frac{2}{3}\theta^{-2})} \rangle = e^{\frac{4}{3}\theta^{-2}}$ by the properties of the lognormal distribution. $C_{a,a}$ decays with time constant $\frac{3}{4}\theta^2$. Finally, the PSD of $a^{(t)}$ can be computed by Fourier-transforming Eq. C12:

$$S_{a,a}(\nu|l) = \theta_l^2 \sigma_{\varepsilon_0}^2 \frac{2\frac{4}{3}\theta_l^{-2}T_0^{-1}}{(2\pi\nu)^2 + (\frac{4}{3}\theta_l^{-2}T_0^{-1})^2} = \frac{\sigma_{\varepsilon_0}^2 \theta_l^2 \gamma_a}{\pi(\nu^2 + \gamma_a^2)}, \tag{C13}$$

which is again a Lorentzian function —like the PSD of $\theta^{(t)}$ — with corner frequency $\gamma_a = (2\pi\frac{3}{4}\theta_l^2T_0)^{-1}$ and maximum $S_{a,a}(0) = 2\sigma_{\varepsilon_0}^2 T_0(\frac{3}{4})^2\theta_l^4$. Notice that, unlike for $S_{\theta,\theta}(\nu|l)$, the ”sampling rate” is fixed to T_0 across all levels. This is because the Brownian motion approximation to activities (Eq. C7) and its subsequent assumptions are not valid at the large timescales of higher levels: they incorporate large and sparse fluctuations induced by $\varepsilon_l^{(t)}$ that can only be modeled as Brownian motion by breaking up the $\varepsilon_l^{(t)}$ into small fluctuations across many small iterations T_0 .

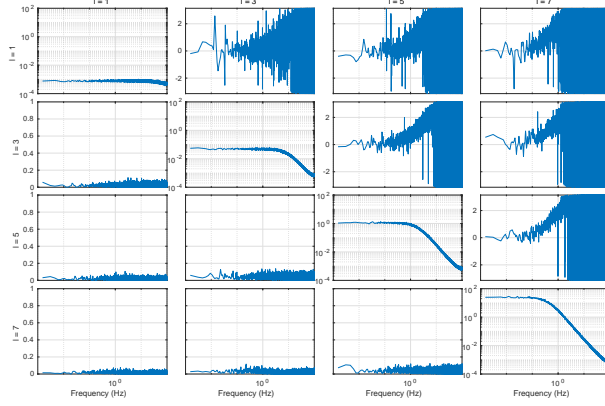


FIG. 19. Cross-spectral phase and magnitude-squared coherence pair-wise estimates of subthreshold activities $a_l^{(t)}$, $l = 1, 3, 5, 7$. Layout and estimation parameters as in Fig. 18.

This still doesn't yield a good estimate of the numerically computed PSD because it overestimates power across the whole frequency range with respect to the numerical simulation output. The reason lies in its discretization and recording schemes: since activities are reset at every iteration when a discharge occurs, $P(A_l = 0) = g_l$, so the amplitude of the simulated time series of activities is a fraction $1 - g_l$ of the amplitude of the continuous-time analog, upon which we derived the PSD estimate. With this last modification, the PSD estimate of the discretized time series becomes

$$S_{a,a}(\nu|l) \approx \frac{\sigma_{\mathcal{E}_0}^2 \theta_l^2 (1 - g_l)^2 \gamma_a}{\pi(\nu^2 + \gamma_a^2)}. \quad (\text{C14})$$

Unlike pulses, activities are pair-wise incoherent over the whole frequency range (Fig. 19), so a specific frequency power in a given level is not transmuted into power in the subsequent level. As a corollary, the PSD of the sum of activities can be approximated by the sum of their PSDs (5).

Regardless of the specific parameters, the takeaway is that activity dynamics, characterized by interleaved periods of diffusion and resetting forces, are well described by the OUP, a similar stochastic process where mean-reverting forces replace jump resets.

Appendix D: Some relationships among activity variables' statistics

From the definition of variance:

$$\langle |\tilde{A}_l|^2 \rangle = \langle \tilde{A}_l^2 \rangle = \text{var} |\tilde{A}_l| + \langle |\tilde{A}_l| \rangle^2 = \text{var} |\tilde{A}_l| + \langle \Theta_l \rangle^2 = \langle A_l^2 \rangle + \langle \mathcal{E}_{l-1}^2 \rangle = \langle A_l^2 \rangle + \langle \mathcal{E}_l^2 \rangle g_l$$

$$\begin{aligned} \langle |\tilde{A}_l|^2 \rangle &= \langle |A_l + \mathcal{E}_{l-1}|^2 \rangle = \langle (A_l + \mathcal{E}_{l-1})^2 \rangle = \langle A_l^2 + \mathcal{E}_{l-1}^2 + 2A_l\mathcal{E}_{l-1} \rangle = \langle A_l^2 \rangle + \langle \mathcal{E}_{l-1}^2 \rangle + \\ 2\langle A_l\mathcal{E}_{l-1} \rangle &= \langle |A_l|^2 \rangle + \langle |\mathcal{E}_{l-1}|^2 \rangle \end{aligned}$$

From the law of total variance applied to $|A|$, $|A^+|$, and $|\tilde{A}|$:

$$\text{var } |\tilde{A}_l| = (1 - g_l) \text{var } |A_l^+| + g_l \text{var } |\mathcal{E}_l| + g_l(1 - g_l)(\langle |\mathcal{E}_l|^2 \rangle + \langle |A_l^+|^2 \rangle) - 2g_l(1 - g_l)\langle |\mathcal{E}_l| \rangle \langle |A_l^+| \rangle$$

$$\text{var } |A_l| = \text{var } A_l^+(1 - g_l) - \langle |A_l^+|^2 \rangle (1 - g_l)^2$$

$$\text{var } |A_l^+| = \text{var } A_l(1 - g_l)^{-1} - \langle |A_l|^2 \rangle (1 - g_l)^{-2}$$

From the definition of variance:

$$\begin{aligned} \text{var } |\tilde{A}_l| &= (1 - g_l) \text{var } |A_l^+| + g_l \text{var } |\mathcal{E}_l| + g_l(1 - g_l)(\langle |\mathcal{E}_l| \rangle - \langle |A_l^+| \rangle)^2 = \langle A_l^2 \rangle - \langle |A_l|^2 \rangle (1 - \\ g_l)^{-1} &+ g_l \text{var } |\mathcal{E}_l| + g_l(1 - g_l)\langle |\mathcal{E}_l|^2 \rangle + g_l(1 - g_l)^{-1}\langle |A_l|^2 \rangle - 2g_l\langle |\mathcal{E}_l| \rangle \langle |A_l| \rangle = \langle A_l^2 \rangle + g_l \text{var } |\mathcal{E}_l| + \\ g_l(1 - g_l)\langle |\mathcal{E}_l|^2 \rangle - \langle |A_l|^2 \rangle - 2g_l\langle |\mathcal{E}_l| \rangle \langle |A_l| \rangle &= \text{var } |A_l| + g_l \text{var } |\mathcal{E}_l| + g_l(1 - g_l)\langle |\mathcal{E}_l|^2 \rangle - 2g_l\langle |\mathcal{E}_l| \rangle \langle |A_l| \rangle \end{aligned}$$

$$\begin{aligned} \langle |\tilde{A}_l|^2 \rangle &= \text{var } |\tilde{A}_l| + \langle \Theta_l \rangle^2 = \text{var } |A_l| + g_l \text{var } |\mathcal{E}_l| + g_l(1 - g_l)\langle |\mathcal{E}_l|^2 \rangle - 2g_l\langle |\mathcal{E}_l| \rangle \langle |A_l| \rangle + g_l^2\langle |\mathcal{E}_l|^2 \rangle + \\ \langle |A_l|^2 \rangle + 2g_l\langle |\mathcal{E}_l| \rangle \langle |A_l| \rangle &= \text{var } |A_l| + g_l \text{var } |\mathcal{E}_l| + g_l(1 - g_l)\langle |\mathcal{E}_l|^2 \rangle + g_l^2\langle |\mathcal{E}_l|^2 \rangle + \langle |A_l|^2 \rangle = \text{var } |A_l| + \\ g_l \text{var } |\mathcal{E}_l| + g_l\langle |\mathcal{E}_l|^2 \rangle + \langle |A_l|^2 \rangle &= \langle A_l^2 \rangle + g_l\langle \mathcal{E}_l^2 \rangle \end{aligned}$$

$$\begin{aligned} \langle \Theta_l \rangle^2 &= \langle A_l^2 \rangle + \langle \mathcal{E}_l^2 \rangle g_l - \text{var } |A_l| - g_l \text{var } |\mathcal{E}_l| - g_l(1 - g_l)\langle |\mathcal{E}_l|^2 \rangle + 2g_l\langle |\mathcal{E}_l| \rangle \langle |A_l| \rangle = \langle |A_l|^2 \rangle + \\ g_l^2\langle |\mathcal{E}_l|^2 \rangle + 2g_l\langle |\mathcal{E}_l| \rangle \langle |A_l| \rangle & \end{aligned}$$

The relation $\langle A^2 \rangle \approx \langle (\theta_* - |A^+|)^2 \rangle$ was verified to hold with reasonable accuracy in numerical simulations. It can be interpreted as equating the time-averaged subthreshold energy to the expected post-pulse energy deficit to reach the threshold in the quiescent trials, a manifestation of energy flow conservation.

Appendix E: Numerical analysis of the rescaled recurrent loop configuration

The recurrence relation specified by Eqs. 32–35 in section V implements a hybrid of bootstrap resampling and discrete-time dynamical system that enables estimating the densities of the variables defining the perfusive cascade, in rescaled recurrent loop configuration, a sort of "perfusive rescaled loop" that bites its own tail. This can be programmed as an iterative loop.

One pool of $N = 10^5$ data points was defined for each variable. The pool of each variable was initialized with values randomly picked out from the time-series (length $9 \cdot 10^6$) of homologous variable at level $l = 1$ (see Fig. 2, second row of left column) in the cascade configuration described in III A. At each iteration t , pulses ε_i were resampled randomly from the pulse pool $\varepsilon_{1:N}$, whereas the gains k_t , thresholds θ_t and subthreshold activities

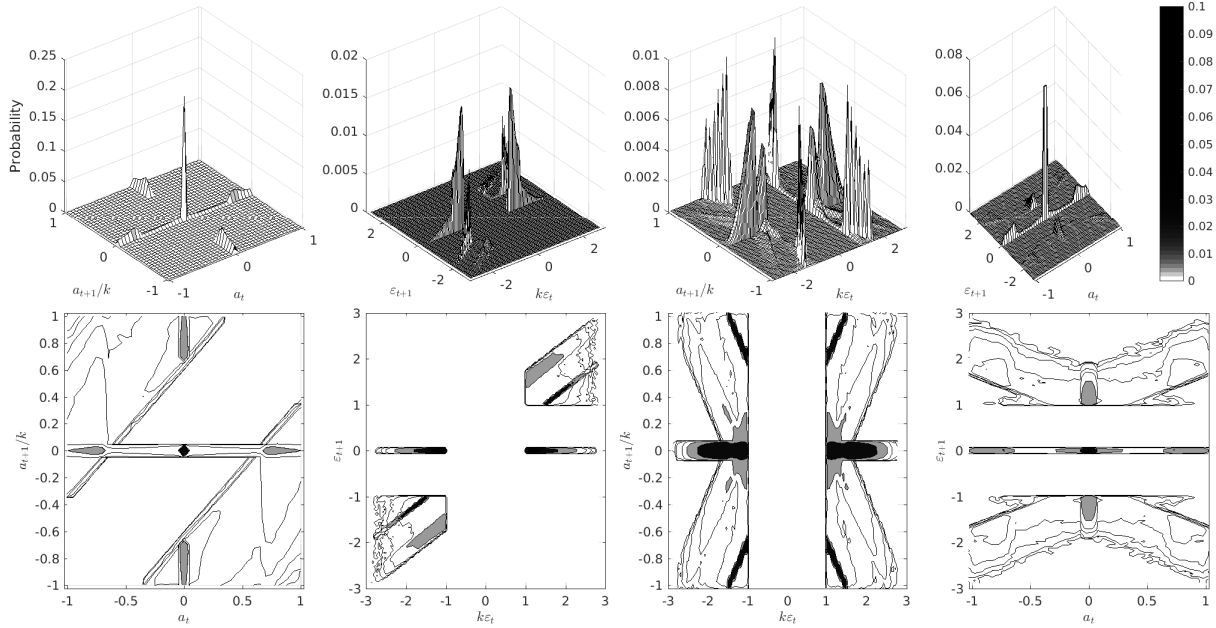


FIG. 20. Surface (top) and contour (bottom) plots of the joint densities $P(a_{t+1}/k, a_t)$ in left, $P(\varepsilon_{t+1}, k\varepsilon_t)$ in middle left, $P(a_{t+1}/k, k\varepsilon_t)$ in middle right, and $P(\varepsilon_{t+1}, a_t)$ in right. Variables have been scaled by k or $1/k$ to facilitate comparison. The color bar at the right of the top right plot is the color legend of the bottom row contour plots; it represents probability.

a_t used were the values they had assigned in the previous iteration. Then each variable was allocated a new value at iteration $t + 1$ according to Eqs. 32 – 35. This routine was run 10^6 times. Instead of using the last trial value a_t , subthreshold activities could also be resampled randomly from the pool $a_{1:N}$ (just as pulses were resampled from $\varepsilon_{1:N}$) to achieve the same results, because same-trial subthreshold activities and incoming pulses are independent. The same holds for θ_t and k_t (in Eq. 34). This was verified in simulations. This scheme generated the data underlying Figs. 9, 10, and 20. Some histogram routines (for plotting transition matrices) are susceptible to binning artifacts. This can be often averted by adding a randomly signed machine epsilon to "jitter" the samples.

Unlike in the feedforward configuration, here we need to estimate k_t to iterate the map. Since k_t is a function of the pool of pulses $\varepsilon_{1:N}$ (cf. Eq. 34), it is susceptible to estimation errors (through pulses), which in turn propagate to the other variables at each iteration. This feature compounds the estimation uncertainty of all variables, and precludes simulating the recurrent loop with fixed threshold and k (e.g. θ_* and k_* in the fixed threshold approximation) —except in the limit of infinitely large bootstrapping pools. Another caveat

is that a recurrent loop embodies a positive feedback that tends to magnify skewness: if left unchecked, the densities will become increasingly lopsided, to the point that the resulting densities will correspond to the case of perfectly correlated driving input ($H = 1$, see below). To avoid this effect, every few iterations the pools must be rendered symmetric, by e.g. randomly flipping the sign of all pulse samples.

The fixed threshold approximation is approached —by definition— in the limit of vanishing θ_t fluctuations: by calculating θ with a pool of subthreshold activity samples $\tilde{a}_{1:N}$, i.e. using Eq. 36 instead of 34, and setting a large enough N — by the law of large numbers, threshold fluctuations wane along with N . However, it is important to realize that the larger is the pool, the more "inertia" it has, so in practice it is expedient to start with a small ("light") pool, and only when it reaches a steady state fill it up with new samples; a large biased pool will remain so for many iterations, which is computationally wasteful.

The above scheme can accommodate autocorrelated driving input with little modification. First, the pulse $\varepsilon_{1:N}$ and subthreshold activity $a_{1:N}$ pools take in samples after applying the absolute value function, so they contain only positive or zero values; since all densities are symmetrical about the origin, no information is thereby lost. Second, the incoming pulse magnitude is defined by the pool sample, whereas its sign is pseudo-randomly generated as $\text{sgn}\mathcal{U}_{[0,1]} < H$, where $\mathcal{U}_{[0,1]}$ the uniform density with support $[0, 1]$, and $H \in [0, 1]$ is a parameter describing the autocorrelation of driving input, that corresponds to the Hurst exponent in fractional Gaussian noise. Thus, the larger is H , the higher is the probability that two consecutive pulses have the same sign, with $H = 0.5$ characterizing white noise. The duplets used to estimate transition matrices in Figs. 10 and 20 were stored at every iteration in separate variables.

A numerically simulated trajectory of the triplet $[\sigma_A/\sigma_{A_*}, \langle\Theta\rangle/\theta_*, \langle|\mathcal{E}|\rangle/\langle|\mathcal{E}_*|\rangle]$ in phase space for a 10^5 iterations fragment is shown in Fig. 21. The system was let settle in the steady state beforehand for 10^6 iterations, so the trajectory wiggles in an attractor located nearby the fixed threshold approximation (although visually it is similar to a 3-dimensional Brownian particle) while displaying a small bias respect to the FTA estimate (cf. 11). In general, reducing the pool size N leads to larger fluctuations, but increasing it too much hinders the trajectory from returning to the vicinity of the expected value after a (random) fluctuation. Increasing the learning rate while using the delta learning rule (Eq. 34 instead of Eq. 36) results in larger oscillations in the $\langle\Theta\rangle/\theta_*$ dimension (not shown).

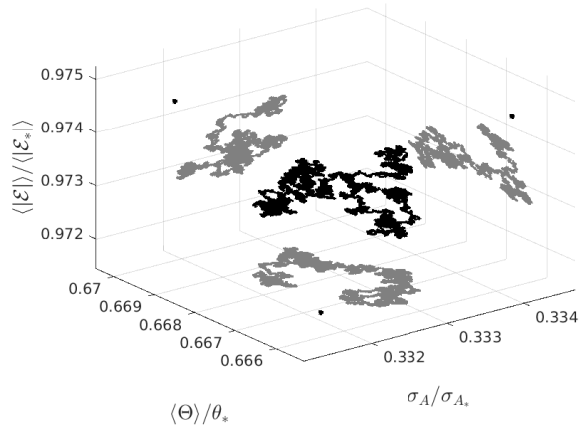


FIG. 21. Simulated trajectory of states for 10^5 iterations in rescaled recurrent loop configuration (Eqs. 32, 33, 36, 35), embedded in the three-dimensional manifold of the normalized variables σ_A/σ_{A_*} , $\langle \Theta \rangle/\theta_*$ and $\langle |\mathcal{E}| \rangle/\langle |\mathcal{E}_*| \rangle$. The dot indicates the fixed threshold approximation (FTA) estimate location. This and the trajectory are also shown projected (in gray) onto the three planes defined pair-wise by the FTA estimates. Parameters: Pool size $N = 10^5$, Gaussian noise input Hurst exponent $H = 0.5$, 10^6 iteration burn-in.

Fig. 22 displays variable estimates using the delta learning rule for thresholds in recurrent configuration as a function of input Hurst parameter. Although it roughly conveys the same information than its homologous Fig. 13 with explicit threshold averaging, we can observe that with the smallest learning rate of $w = 10^{-4}$ (dashed line), the hill peak at $H \approx .74$ is shifted to $H \approx .8$. The reason seems to lie in that under superdiffusion, this configuration greatly overestimates the discharge rate g and underestimates the threshold with respect to the fixed threshold approximation, as can be seen in Fig. 22. Finally, note that in the feedforward configuration simulations in section III, we used a learning rate $w = 0.01$, which corresponds to the dashed-dotted line in Fig. 22.

Appendix F: Modeling of pulse size densities with the generalized Pareto distribution

We suggested in section III A that pulse density profiles follow approximately a generalized Pareto distribution (GPD), which is a family of probability densities, often used to model the shape of the tail of other distributions [196]. Here we use the GPD as a parametric

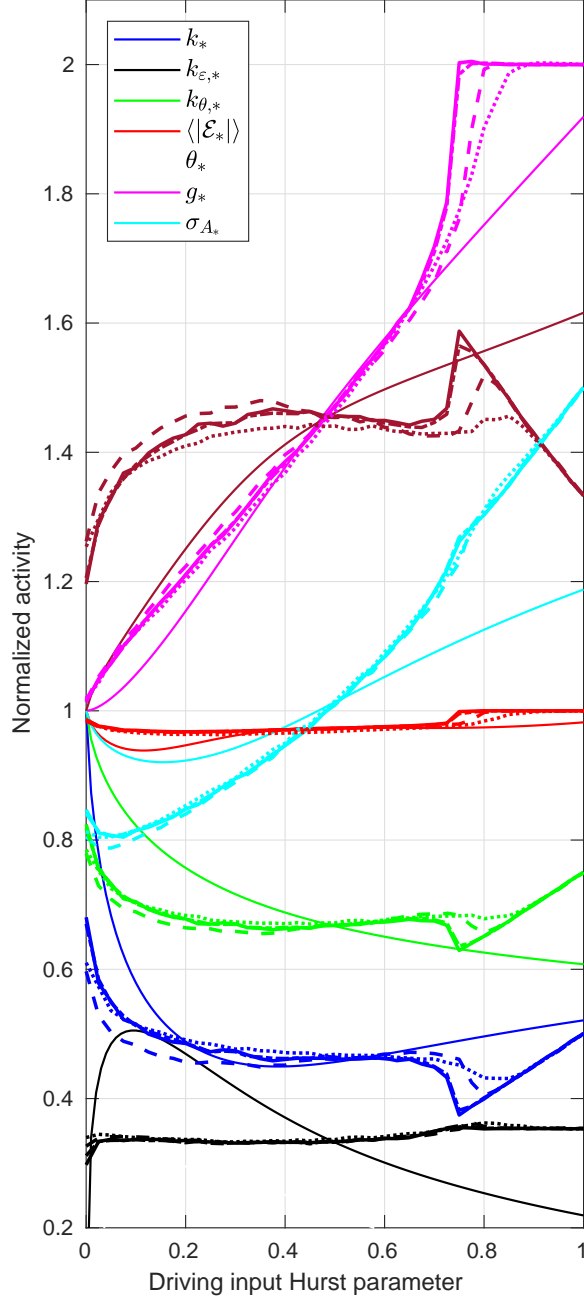


FIG. 22. Perfusive cascade variables' (see legend) estimates with delta learning rule, as a function of driving input autocorrelation, in recurrent rescaled loop configuration. A , \mathcal{E} are scaled consistently with $\langle \mathcal{E}^2 \rangle = 1$. Line style indicates the estimation procedure: closed form expression (Eqs. 42 – 45) derived through the fixed threshold approximation (solid thin); simulation with learning rate $w = 10^{-1}$ (dotted), $N = 10^{-2}$ (dash-dotted), $N = 10^{-3}$ (solid thick), $N = 2 \cdot 10^{-4}$ (dashed).

approximation to the tails of $f_{\tilde{A}}$, or equivalently to the pulse sizes $f_{|\mathcal{E}|}$. The GPD density is defined as

$$f_{GPD}(x|\mu, \sigma, \xi) = \frac{1}{\sigma} \left(1 + \xi \frac{x - \mu}{\sigma} \right)^{-1 - \frac{1}{\xi}},$$

with the parameters location μ (which defines the minimum of \mathcal{E}), scale σ , and shape ξ (which characterizes how steeply the tail falls off). In this section, the reader is advised to be on guard not to confuse the standard deviation symbol σ , which always bears the subscript of a variable, with the GPD scale parameter *sigma*. Its support is $x \geq \mu$ when $\xi \geq 0$ and $\mu \leq x \leq \mu - \sigma/\xi \equiv M$ when $\xi < 0$. Its mean is $\mu + \frac{\sigma}{1-\xi}$ when $\xi < 1$, its median is $\mu + \sigma \frac{2^\xi - 1}{\xi}$, and its mode is μ .

By definition, $f_{|\mathcal{E}_l|}$ is the tail distribution of the absolute value of post-pulse activity $|\tilde{A}_l|$. Its cumulative distribution function $F_{|\mathcal{E}_l|}(x) \equiv P(|\mathcal{E}_l| \leq x)$ is also the excess distribution of post-pulse activities above the firing threshold $P(|\tilde{A}_l| - \theta_l \leq x \mid |\tilde{A}_l| > \theta_l) = \frac{F_{|\mathcal{E}_l|}(\theta_l + x) - F_{|\mathcal{E}_l|}(\theta_l)}{1 - F_{|\mathcal{E}_l|}(\theta_l)}$. For large enough l , this can be interpreted as the tail of the cumulative distribution of a sequence of identically distributed and independent random variables conditioned to be larger than some threshold: each ε_l can be decomposed as the sum of inputs ε_0 's by recursively substituting each ε_l by its summands $\varepsilon_{l-1} + a_{l-1}$, which by construction are already conditioned on their absolute value exceeding θ_{l-1} . This supplies the conditions of applicability of the Gnedenko-Pickands-Balkema-de Haan theorem, which states that the tail of the excess distribution is asymptotically given by a GPD as the variable approaches the end of the tail of the distribution [57]. This implies that in the steady state, and for large enough l , the tail distribution $F_{\mathcal{E}_l}$ can be asymptotically characterized by a GPD.

This justifies using the GPD to model $f_{|\mathcal{E}_l|}$ for large enough l . Maximum likelihood fits (through MATLAB's `fitdist` function) of the GPD parameters to the numerically obtained histograms of $f_{|\mathcal{E}_l|}$ yielded the estimates displayed in Table IV.

The GPD parameters corresponding to the fixed threshold approximation can be obtained through the estimates for θ and $\sigma_{|\mathcal{E}|}$ given at the end of section IV D; thereby we can establish the equalities $\mu_* = \theta_*$ and $\mu_* + \frac{\sigma_*}{1-\xi_*} = \sigma_{|\mathcal{E}_*|}$. This yields

$$\begin{aligned} \frac{\sigma_*}{\mu_*} &\approx 0.6579 \\ \xi_* &\approx -0.4274. \end{aligned}$$

It follows that $-1 - \frac{1}{\xi_*} \approx 1.3396$ is the exponent in f_{GPD} , the mean is $\frac{\sigma_{|\mathcal{E}_*|}}{\mu_*} \approx 1.4609$ (which entails a gain of .4349), the median $1 + \frac{\sigma_*}{\mu_*} \frac{2^{\xi_*} - 1}{\xi_*} \approx 1.3947$ (gain .5), and the maximum of the

TABLE IV. Maximum likelihood estimates of GPD parameters fit to the numerical pulse size distributions of the perfusive cascade levels $l = 1 \dots 7$. Location parameters μ_l were fixed to their corresponding level threshold means (cf. Table II); scale parameters are scaled by their corresponding location parameters. Only significant digits are shown. Numerical simulation parameters are as in Fig. 2.

Level l	μ_l	σ_l/μ_l	ξ_l
1	$\langle \Theta_1 \rangle$.832	-.151
2	$\langle \Theta_2 \rangle$.596	-.169
3	$\langle \Theta_3 \rangle$.571	-.214
4	$\langle \Theta_4 \rangle$.564	-.239
5	$\langle \Theta_5 \rangle$.606	-.304
6	$\langle \Theta_6 \rangle$.606	-.319
7	$\langle \Theta_7 \rangle$.609	-.315

support $\frac{M_*}{\mu_*} \approx 2.5393$ (notice all these values have been scaled by the threshold $\mu_* = \theta_*$). Finally, the derivative of the density at the threshold is $f'_{GPD}(\mu_*) = -\frac{1+\xi_*}{\sigma_*} \approx -0.8703$.

-
- [1] I. Prigogine and G. Nicolis, Self-Organisation in Nonequilibrium Systems: Towards A Dynamics of Complexity, in *Bifurc. Anal.* (Springer Netherlands, 1985) pp. 3–12.
 - [2] A. Vespignani and S. Zapperi, How self-organized criticality works: A unified mean-field picture, *Phys. Rev. E - Stat. Physics, Plasmas, Fluids, Relat. Interdiscip. Top.* **57**, 6345 (1998), arXiv:9709192 [cond-mat].
 - [3] P. Bak, C. Tang, and K. Wiesenfeld, Self-organized criticality: An explanation of the 1/f noise, *Phys. Rev. Lett.* **59**, 381 (1987).
 - [4] B. Gutenberg and C. F. Richter, Earthquake magnitude, intensity, energy, and acceleration: (Second paper), *Bull. Seismol. Soc. Am.* **46**, 105 (1956).
 - [5] H. J. S. Feder and J. Feder, Self-organized criticality in a stick-slip process, *Phys. Rev. Lett.* **66**, 2669 (1991).
 - [6] Z. Olami, H. J. S. Feder, and K. Christensen, Self-organized criticality in a continuous,

- nonconservative cellular automaton modeling earthquakes, *Phys. Rev. Lett.* **68**, 1244 (1992).
- [7] K. Nagel and M. Paczuski, Emergent traffic jams, *Phys. Rev. E* **51**, 2909 (1995), arXiv:9502004 [adap-org].
- [8] B. Drossel and F. Schwabl, Self-organized critical forest-fire model, *Phys. Rev. Lett.* **69**, 1629 (1992).
- [9] C. J. Rhodes, H. J. Jensen, and R. M. Anderson, On the critical behaviour of simple epidemics, *Proc. R. Soc. B Biol. Sci.* **264**, 1639 (1997).
- [10] A. Corral, C. J. Pérez, A. Díaz-Guilera, and A. Arenas, Self-organized criticality and synchronization in a lattice model of integrate-and-fire oscillators, *Phys. Rev. Lett.* **74**, 118 (1995).
- [11] A. V. Herz and J. J. Hopfield, Earthquake cycles and neural reverberations: Collective oscillations in systems with pulse-coupled threshold elements., *Phys. Rev. Lett.* **75**, 1222 (1995).
- [12] D. Chialvo and P. Bak, Learning from mistakes, *Neuroscience* **90**, 1137 (1999).
- [13] E. T. Lu, R. J. Hamilton, J. M. McTiernan, and K. R. Bromund, Solar flares and avalanches in driven dissipative systems, *Astrophys. J.* **412**, 841 (1993).
- [14] J. M. Beggs and D. Plenz, Neuronal avalanches in neocortical circuits., *J. Neurosci.* **23**, 11167 (2003).
- [15] C. G. Langton, Computation at the edge of chaos: Phase transitions and emergent computation, *Phys. D Nonlinear Phenom.* **42**, 12 (1990).
- [16] W. L. Shew and D. Plenz, The functional benefits of criticality in the cortex., *Neuroscientist* **19**, 88 (2013).
- [17] R. C. Conant and W. R. Ashby, Every good regulator of a system must be a model of that system, *Int. J. Syst. Sci.* **1**, 89 (1970).
- [18] K. J. Friston, J. Kilner, and L. Harrison, A free energy principle for the brain., *J. Physiol. Paris* **100**, 70 (2006).
- [19] E. Novikov, A. Novikov, D. Shannahoff-Khalsa, B. Schwartz, and J. Wright, Scale-similar activity in the brain, *Phys. Rev. E - Stat. Physics, Plasmas, Fluids, Relat. Interdiscip. Top.* **56**, R2387 (1997).
- [20] K. Linkenkaer-Hansen, V. V. Nikouline, J. M. Palva, and R. J. Ilmoniemi, Long-Range Temporal Correlations and Scaling Behavior in Human Brain Oscillations, *J. Neurosci.* **21**,

- 1370 (2001).
- [21] C. T. Kello, G. D. A. Brown, R. Ferrer-i Cancho, J. G. Holden, K. Linkenkaer-Hansen, T. Rhodes, and G. C. Van Orden, Scaling laws in cognitive sciences, *Trends Cogn. Sci.* **14**, 223 (2010).
 - [22] J. M. Palva, A. Zhigalov, J. Hirvonen, O. Korhonen, K. Linkenkaer-Hansen, and S. Palva, Neuronal long-range temporal correlations and avalanche dynamics are correlated with behavioral scaling laws., *Proc. Natl. Acad. Sci. U. S. A.* **110**, 3585 (2013).
 - [23] A. Zhigalov, G. Arnulfo, L. Nobili, S. Palva, and J. Matias Palva, Relationship of fast- and slow-timescale neuronal dynamics in human MEG and SEEG, *J. Neurosci.* **35**, 5385 (2015).
 - [24] P. Dayan, G. E. Hinton, R. M. Neal, and R. S. Zemel, The Helmholtz Machine, *Neural Comput.* **7**, 889 (1995).
 - [25] K. J. Friston, P. Rotshtein, J. J. Geng, P. Sterzer, and R. N. Henson, A critique of functional localisers, *Neuroimage* **30**, 1077 (2006).
 - [26] D. Mumford, On the computational architecture of the neocortex - II The role of cortico-cortical loops, *Biol. Cybern.* **66**, 241 (1992).
 - [27] K. Friston, Learning and inference in the brain, *Neural Networks* **16**, 1325 (2003).
 - [28] T. S. Lee and D. Mumford, Hierarchical Bayesian inference in the visual cortex, *J. Opt. Soc. Am. A* **20**, 1434 (2003).
 - [29] D. J. Felleman and D. C. Van Essen, Distributed hierarchical processing in the primate cerebral cortex., *Cereb. Cortex* **1**, 1 (1991).
 - [30] W. A. Phillips and W. Singer, In search of common foundations for cortical computation (1997).
 - [31] S. J. Kiebel, J. Daunizeau, and K. J. Friston, A Hierarchy of Time-Scales and the Brain, *PLoS Comput. Biol.* **4**, e1000209+ (2008).
 - [32] K. J. Friston, M. Breakspear, and G. Deco, Perception and self-organized instability., *Front. Comput. Neurosci.* **6**, 10.3389/fncom.2012.00044 (2012).
 - [33] C. W. Eurich, J. M. Herrmann, and U. A. Ernst, Finite-size effects of avalanche dynamics, *Phys. Rev. E - Stat. Physics, Plasmas, Fluids, Relat. Interdiscip. Top.* **66**, 15 (2002).
 - [34] N. Bertschinger and T. Natschläger, Real-Time Computation at the Edge of Chaos in Recurrent Neural Networks, *Neural Comput.* **16**, 1413 (2004).
 - [35] L. De Arcangelis, C. Perrone-Capano, and H. J. Herrmann, Self-organized criticality

- model for brain plasticity, *Phys. Rev. Lett.* **96**, 10.1103/PhysRevLett.96.028107 (2006), arXiv:0602014 [q-bio].
- [36] A. Levina, J. M. Herrmann, and T. Geisel, Dynamical synapses causing self-organized criticality in neural networks, *Nat. Phys.* **3**, 857 (2007), arXiv:0712.1003.
- [37] S.-S. S. Poil, R. Hardstone, H. D. Mansvelder, and K. Linkenkaer-Hansen, Critical-state dynamics of avalanches and oscillations jointly emerge from balanced excitation/inhibition in neuronal networks., *J. Neurosci.* **32**, 9817 (2012).
- [38] K. J. Friston, J. Mattout, N. Trujillo-Barreto, J. Ashburner, and W. Penny, Variational free energy and the Laplace approximation, *Neuroimage* **34**, 220 (2007).
- [39] V. Loreto, A. Vespignani, and S. Zapperi, Renormalization scheme for forest-fire models, *J. Phys. A. Math. Gen.* **29**, 2981 (1996).
- [40] The PC system is similar to a sequence of sluices or a stack of sōzus. A sōzu is a water-powered rocking device —a bamboo pipe pivoted to one side of its center of gravity. At rest its mouth is tilted upwards while its bottom lies on a support. A trickle of water fills it till its tipping point (the center of gravity is displaced past the pivot), when the pipe rotates around its pivot and dumps out *all* the water it contained. A sōzu operates intermittently in the seesaw fashion of a relaxation oscillator [197] as long as the water flow persists. Thus, in a hierarchy of sōzus arranged so that each lies below the preceding, outflows and inflows are coupled sequentially, and the ensemble constitutes a cascade with level-wise intermittent falls. However, there are two important differences: water can only steadily build up, until it is discharged (there is no anti-water equivalent) and thresholds are fixed. Threshold adaptation could be accomplished by fastening the pivot shaft to the pipe, filling it with a dilatant (shear-thickening fluid), and making it rotate about another internal coaxial shaft in turn attached to the support. If the dilatant viscosity change had a long enough time constant, it would mimic approximately the behavior of adaptive thresholds.
- [41] P. De Los Rios and Y. C. Zhang, Universal 1/f noise from dissipative SOC models, *Phys. Rev. Lett.* **82**, 472 (1999).
- [42] A. Levina, J. M. Herrmann, and T. Geisel, Phase transitions towards criticality in a neural system with adaptive interactions., *Phys. Rev. Lett.* **102**, 118110 (2009).
- [43] J. M. Carlson and J. Doyle, Highly optimized tolerance: A mechanism for power laws in designed systems, *Phys. Rev. E - Stat. Physics, Plasmas, Fluids, Relat. Interdiscip. Top.* **60**,

- 1412 (1999).
- [44] D. R. Chialvo, Emergent complexity: What uphill analysis or downhill invention cannot do, *New Ideas Psychol.* **26**, 158 (2008), arXiv:0804.0008.
 - [45] A. L. Fairhall, G. D. Lewen, W. Bialek, and D. Ruyter, Efficiency and ambiguity in an adaptive neural code, *Nature* **412**, 787 (2001).
 - [46] A. Kohn, *Visual adaptation: Physiology, mechanisms, and functional benefits* (2007).
 - [47] B. Nessler, M. Pfeiffer, L. Buesing, and W. Maass, Bayesian Computation Emerges in Generic Cortical Microcircuits through Spike-Timing-Dependent Plasticity, *PLoS Comput. Biol.* **9**, e1003037 (2013).
 - [48] A. Bernacchia, The interplay of plasticity and adaptation in neural circuits: A generative model, *Front. Synaptic Neurosci.* **6**, 26 (2014).
 - [49] S. A. Kauffman, Origins of Order in Evolution: Self-Organization and Selection, in *Underst. Orig.* (Springer, Dordrecht, 1992) pp. 153–181.
 - [50] M. R. Evans and S. N. Majumdar, Diffusion with optimal resetting, *J. Phys. A Math. Theor.* **44**, 10.1088/1751-8113/44/43/435001 (2011), arXiv:1107.4225.
 - [51] J. H. J. H. Holland, Emergence: from chaos to order, *Choice Rev. Online* **35**, 35 (1998).
 - [52] S. Dehaene and J.-P. P. Changeux, Ongoing spontaneous activity controls access to consciousness: a neuronal model for inattentive blindness., *PLoS Biol.* **3**, 10.1371/journal.pbio.0030141 (2005).
 - [53] W. Schottky, Small-shot effect and flicker effect, *Phys. Rev.* **28**, 74 (1926).
 - [54] S. B. Lowen and M. C. Teich, Fractal renewal processes generate 1/f noise, *Phys. Rev. E* **47**, 992 (1993).
 - [55] J. A. Barnes and D. W. Allan, A Statistical Model of Flicker Noise, *Proc. IEEE* **54**, 176 (1966).
 - [56] B. B. Mandelbrot and J. W. Van Ness, Fractional Brownian Motions, Fractional Noises and Applications, *SIAM Rev.* **10**, 422 (1968).
 - [57] D. Sornette, *Crit. Phenom. Nat. Sci.*, Springer Series in Synergetics (Springer Berlin Heidelberg, Berlin, Heidelberg, 2000) p. 528.
 - [58] Y. C. Zhang, Scaling theory of self-organized criticality, *Phys. Rev. Lett.* **63**, 470 (1989).
 - [59] T. P. Straatsma, H. J. Berendsen, and A. J. Stam, Estimation of statistical errors in molecular simulation calculations, *Mol. Phys.* **57**, 89 (1986).

- [60] R. E. Kass and D. Steffey, Approximate Bayesian Inference in Conditionally Independent Hierarchical Models (Parametric Empirical Bayes Models), *J. Am. Stat. Assoc.* **84**, 717 (1989).
- [61] J. P. Sethna, K. A. Dahmen, and C. R. Myers, Crackling noise (2001).
- [62] R. Durrett, *Probability: Theory and Examples*, 5th ed. (Cambridge University Press, 2019).
- [63] D. R. Chialvo, G. A. Cecchi, and M. O. Magnasco, Noise-induced memory in extended excitable systems, *Phys. Rev. E - Stat. Physics, Plasmas, Fluids, Relat. Interdiscip. Top.* **61**, 5654 (2000).
- [64] We use the term metabolic energy (or metabolic power, for metabolic energy rate) when referring to the energy required by living organisms to maintain homeostasis, to distinguish it from squared activity.
- [65] R. P. N. Rao and D. H. Ballard, Predictive coding in the visual cortex: a functional interpretation of some extra-classical receptive-field effects, *Nat. Neurosci.* **2**, 79 (1999).
- [66] S. Hochstein and M. Ahissar, View from the top: Hierarchies and reverse hierarchies in the visual system (2002).
- [67] K. J. Friston, A theory of cortical responses., *Philos. Trans. R. Soc. Lond. B. Biol. Sci.* **360**, 815 (2005).
- [68] K. J. Friston, N. Trujillo-Barreto, and J. Daunizeau, DEM: A variational treatment of dynamic systems, *Neuroimage* **41**, 849 (2008).
- [69] Bernstein-Von Mises theorem.
- [70] M. J. Beal and Z. Ghahramani, The Variational Bayesian EM Algorithm for Incomplete Data: with Application to Scoring Graphical Model Structures, in *Bayesian Stat.*, edited by J. M. Bernardo, M. J. Bayarri, J. O. Berger, A. P. Dawid, D. Heckerman, A. F. M. Smith, and M. West (Oxford University Press, 2003) Chap. 7.
- [71] S. A. Kauffman and S. Johnsen, Coevolution to the edge of chaos: Coupled fitness landscapes, poised states, and coevolutionary avalanches, *J. Theor. Biol.* **149**, 467 (1991).
- [72] N. N. Taleb, *The Black Swan: The Impact of the Highly Improbable* (Random House Trade Paperbacks, 2010) p. 480.
- [73] D. M. Raup, Biological extinction in earth history (1986).
- [74] M. L. McKinney, Extinction vulnerability and selectivity: Combining ecological and paleontological views (1997).
- [75] M. Newman, The power of design (2000).

- [76] J. M. Beggs, *The Critically Tuned Cortex* (2019).
- [77] P. Lennie, The cost of cortical computation, *Curr. Biol.* **13**, 493 (2003).
- [78] B. A. Olshausen and D. J. Field, Emergence of simple-cell receptive field properties by learning a sparse code for natural images., *Nature* **381**, 607 (1996).
- [79] C. F. Stevens and A. Zador, Information through a spiking neuron, *Adv. Neural Inf. Process. Syst.* , 75 (1996).
- [80] Although information content and surprisal are usually synonyms to Shannon information, here information content denotes the entropy of the living system’s internal model, whereas surprisal denotes the fraction of that entropy attributable to surprisal, corresponding to mismatches between the sensory input and the expected sensory input.
- [81] H. Haken, *Synergetics*, Springer Series in Synergetics (Springer Berlin Heidelberg, Berlin, Heidelberg, 1983).
- [82] A. Kleidon, Nonequilibrium thermodynamics and maximum entropy production in the Earth system: applications and implications. (2009).
- [83] C. Gamble, *Settling Earth Archaeol. Deep Hum. Hist.* (Cambridge University Press, 2012) pp. 1–377.
- [84] C. Bromer, T. M. Bartol, J. B. Bowden, D. D. Hubbard, D. C. Hanka, P. V. Gonzalez, M. Kuwajima, J. M. Mendenhall, P. H. Parker, W. C. Abraham, T. J. Sejnowski, and K. M. Harris, Long-term potentiation expands information content of hippocampal dentate gyrus synapses, *Proc. Natl. Acad. Sci. U. S. A.* **115**, E2410 (2018).
- [85] K. J. Friston, Transients, metastability, and neuronal dynamics., *Neuroimage* **5**, 164 (1997).
- [86] D. J. Evans and D. J. Searles, The fluctuation theorem, *Adv. Phys.* **51**, 1529 (2002).
- [87] R. Linsker, Perceptual Neural Organization: Some Approaches Based on Network Models and Information Theory, *Annu. Rev. Neurosci.* **13**, 257 (1990).
- [88] P. Verghese and D. G. Pelli, The information capacity of visual attention, *Vision Res.* **32**, 983 (1992).
- [89] T. Wu, A. J. Dufford, M. A. Mackie, L. J. Egan, and J. Fan, The Capacity of Cognitive Control Estimated from a Perceptual Decision Making Task, *Sci. Rep.* **6**, 10.1038/srep34025 (2016).
- [90] Note that the width of the conscious integration kernel (the interval over which events are integrated into a single percept) is $\approx 100\text{--}400$ ms [170, 198, 199], which suggests an information

- content for each “conscious snapshot” of ≈ 10 b.
- [91] T. Hwa and M. Kardar, Dissipative transport in open systems: An investigation of self-organized criticality, *Phys. Rev. Lett.* **62**, 1813 (1989).
 - [92] B. Efron and C. Morris, Stein’s estimation rule and its competitors—an empirical bayes approach, *J. Am. Stat. Assoc.* **68**, 117 (1973).
 - [93] K. Fujimoto and K. Kaneko, How fast elements can affect slow dynamics, *Phys. D Nonlinear Phenom.* **180**, 1 (2003), arXiv:0108038 [nlin].
 - [94] V. K. Jirsa, A. Fuchs, and J. A. Kelso, Connecting Cortical and Behavioral Dynamics: Bimanual Coordination, *Neural Comput.* **10**, 2019 (1998).
 - [95] T. Zorick and M. A. Mandelkern, Discrete scale invariance of human large eeg voltage deflections is more prominent in waking than sleep stage 2, *Front. Hum. Neurosci.* **9**, 638 (2015).
 - [96] E. Jürgens, F. Rösier, E. Hennighausen, and M. Heil, Stimulus-induced gamma oscillations: harmonics of alpha activity?, *Neuroreport* **6**, 813 (1995).
 - [97] M. Penttonen and G. Buzsáki, Natural logarithmic relationship between brain oscillators, *Thalamus Relat. Syst.* **2**, 145 (2003).
 - [98] S. Erland and P. E. Greenwood, Constructing $1/\omega^\alpha$ noise from reversible Markov chains, *Phys. Rev. E - Stat. Nonlinear, Soft Matter Phys.* **76**, 031114 (2007).
 - [99] C. van Vreeswijk and H. Sompolinsky, Chaos in neuronal networks with balanced excitatory and inhibitory activity., *Science (80-.)*. **274**, 1724 (1996).
 - [100] K. J. Friston, J. Daunizeau, J. Kilner, and S. J. Kiebel, Action and behavior: A free-energy formulation, *Biol. Cybern.* **102**, 227 (2010).
 - [101] M. Martinez-Saito, A Skeptical View on the Physics-Consciousness Explanatory Gap, *Axiomathes* , 1 (2021).
 - [102] F. Lombardi, H. J. Herrmann, D. Plenz, and L. De Arcangelis, On the temporal organization of neuronal avalanches, *Front. Syst. Neurosci.* **8**, 204 (2014).
 - [103] R. Srinivasan, P. L. Nunez, D. M. Tucker, R. B. Silberstein, and P. J. Cadusch, Spatial sampling and filtering of EEG with spline laplacians to estimate cortical potentials, *Brain Topogr.* **8**, 355 (1996).
 - [104] W. J. Freeman, L. J. Rogers, M. D. Holmes, and D. L. Silbergeld, Spatial spectral analysis of human electrocorticograms including the alpha and gamma bands, *J. Neurosci. Methods* **95**, 111 (2000).

- [105] C. Bédard, H. Kröger, and A. Destexhe, Does the 1/f frequency scaling of brain signals reflect self-organized critical states?, *Phys. Rev. Lett.* **97**, 118102 (2006), arXiv:0608026 [q-bio].
- [106] K. J. Miller, L. B. Sorensen, J. G. Ojemann, and M. Den Nijs, Power-law scaling in the brain surface electric potential, *PLoS Comput. Biol.* **5**, e1000609 (2009).
- [107] D. J. Smit, E. J. de Geus, M. E. van de Nieuwenhuijzen, C. E. van Beijsterveldt, G. C. M. van Baal, H. D. Mansvelder, D. I. Boomsma, and K. Linkenkaer-Hansen, Scale-free modulation of resting-state neuronal oscillations reflects prolonged brain maturation in humans, *J. Neurosci.* **31**, 13128 (2011).
- [108] A. K. Engel, P. Fries, and W. Singer, Dynamic predictions: Oscillations and synchrony in top-down processing, *Nat. Rev. Neurosci.* **2**, 704 (2001).
- [109] G. Buzsáki and A. Draguhn, Neuronal oscillations in cortical networks., *Science (80-.)*. **304**, 1926 (2004).
- [110] N. Kopell, G. B. Ermentrout, M. A. Whittington, and R. D. Traub, Gamma rhythms and beta rhythms have different synchronization properties, *Proc. Natl. Acad. Sci. U. S. A.* **97**, 1867 (2000).
- [111] A. Von Stein, P. Rappelsberger, J. Sarnthein, and H. Petsche, Synchronization between temporal and parietal cortex during multimodal object processing in man, *Cereb. Cortex* **9**, 137 (1999).
- [112] F. Varela, J.-P. P. Lachaux, E. Rodriguez, and J. Martinerie, The brainweb: Phase synchronization and large-scale integration, *Nat. Rev. Neurosci.* **2**, 229 (2001).
- [113] T. T. Hahn, B. Sakmann, and M. R. Mehta, Phase-locking of hippocampal interneurons' membrane potential to neocortical up-down states, *Nat. Neurosci.* **9**, 1359 (2006).
- [114] E. D. Gireesh and D. Plenz, Neuronal avalanches organize as nested theta- and beta/gamma-oscillations during development of cortical layer 2/3, *Proc. Natl. Acad. Sci. U. S. A.* **105**, 7576 (2008).
- [115] B. J. He, J. M. Zempel, A. Z. Snyder, and M. E. Raichle, The temporal structures and functional significance of scale-free brain activity, *Neuron* **66**, 353 (2010).
- [116] A. C. Yu and D. Margoliash, Temporal hierarchical control of singing in birds, *Science (80-.)*. **273**, 1871 (1996).
- [117] M.-M. Mesulam, From sensation to cognition, *Brain* **121**, 1013 (1998).
- [118] U. Hasson, E. Yang, I. Vallines, D. J. Heeger, and N. Rubin, A Hierarchy of Temporal

- Receptive Windows in Human Cortex, *J. Neurosci.* **28**, 2539 (2008).
- [119] U. Hasson, J. Chen, and C. J. Honey, Hierarchical process memory: Memory as an integral component of information processing (2015).
- [120] S. M. Sherman and R. W. Guillery, On the actions that one nerve cell can have on another: Distinguishing "drivers" from "modulators", *Proc. Natl. Acad. Sci.* **95**, 7121 (1998).
- [121] A. C. Huk and M. N. Shadlen, Neural Activity in Macaque Parietal Cortex Reflects Temporal Integration of Visual Motion Signals during Perceptual Decision Making, *J. Neurosci.* **25**, 10420 (2005).
- [122] D. Poeppel, W. J. Idsardi, and V. Van Wassenhove, Speech perception at the interface of neurobiology and linguistics (2008).
- [123] R. Quiñones Quiroga, L. Reddy, G. Kreiman, C. Koch, I. Fried, R. Q. Quiroga, L. Reddy, G. Kreiman, C. Koch, and I. Fried, Invariant visual representation by single neurons in the human brain, *Nature* **435**, 1102 (2005).
- [124] K. J. Friston, The free-energy principle: a unified brain theory?, *Nat. Rev. Neurosci.* **11**, 127 (2010).
- [125] M. J. West and H. J. Gundersen, Unbiased stereological estimation of the number of neurons in the human hippocampus, *J. Comp. Neurol.* **296**, 1 (1990).
- [126] G. Buzsáki, *The hippocampo-neocortical dialogue* (1996).
- [127] K. Friston and G. Buzsáki, *The Functional Anatomy of Time: What and When in the Brain* (2016).
- [128] R. F. Thompson and J. J. Kim, Memory systems in the brain and localization of a memory, *Proc. Natl. Acad. Sci. U. S. A.* **93**, 13438 (1996).
- [129] C. J. Honey, T. Thesen, T. H. Donner, L. J. Silbert, C. E. Carlson, O. Devinsky, W. K. Doyle, N. Rubin, D. J. Heeger, and U. Hasson, Slow Cortical Dynamics and the Accumulation of Information over Long Timescales, *Neuron* **76**, 423 (2012).
- [130] J. D. Murray, A. Bernacchia, D. J. Freedman, R. Romo, J. D. Wallis, X. Cai, C. Padoa-Schioppa, T. Pasternak, H. Seo, D. Lee, and X. J. Wang, A hierarchy of intrinsic timescales across primate cortex, *Nat. Neurosci.* **17**, 1661 (2014).
- [131] D. R. Chialvo, Psychophysics: Are our senses critical?, *Nat. Phys.* **2**, 301 (2006).
- [132] M. Paczuski, S. Maslov, and P. Bak, Avalanche dynamics in evolution, growth, and depinning models, *Phys. Rev. E - Stat. Physics, Plasmas, Fluids, Relat. Interdiscip. Top.* **53**, 414 (1996),

- arXiv:9510002 [adap-org].
- [133] D. W. Dong and J. J. Atick, Statistics of natural time-varying images, *Netw. Comput. Neural Syst.* **6**, 345 (1995).
- [134] V. A. Billock, G. C. De Guzman, and J. A. Scott Kelso, Fractal time and 1/f spectra in dynamic images and human vision, *Phys. D Nonlinear Phenom.* **148**, 136 (2001).
- [135] M. G. Kitzbichler, M. L. Smith, S. R. Christensen, and E. Bullmore, Broadband criticality of human brain network synchronization, *PLoS Comput. Biol.* **5**, e1000314 (2009).
- [136] V. Priesemann, M. Wibral, M. Valderrama, R. Pröpper, M. Le Van Quyen, T. Geisel, J. Triesch, D. Nikolić, and M. H. Munk, Spike avalanches in vivo suggest a driven, slightly subcritical brain state, *Front. Syst. Neurosci.* **8**, 108 (2014).
- [137] L. L. Gollo, Coexistence of critical sensitivity and subcritical specificity can yield optimal population coding, *J. R. Soc. Interface* **14**, 10.1098/rsif.2017.0207 (2017), arXiv:1707.04484.
- [138] W. J. Freeman, Simulation of chaotic EEG patterns with a dynamic model of the olfactory system, *Biol. Cybern.* **56**, 139 (1987).
- [139] W. L. Shew, W. P. Clawson, J. Pobst, Y. Karimipannah, N. C. Wright, and R. Wessel, Adaptation to sensory input tunes visual cortex to criticality, *Nat. Phys.* **11**, 659 (2015).
- [140] J. M. Beggs, The criticality hypothesis: How local cortical networks might optimize information processing, *Philos. Trans. R. Soc. A Math. Phys. Eng. Sci.* **366**, 329 (2008).
- [141] J. M. Beggs and N. Timme, Being critical of criticality in the brain, *Front. Physiol.* **3 JUN**, 163 (2012).
- [142] L. Cocchi, L. L. Gollo, A. Zalesky, and M. Breakspear, Criticality in the brain: A synthesis of neurobiology, models and cognition (2017), arXiv:1707.05952.
- [143] O. Shriki, J. Alstott, F. Carver, T. Holroyd, R. N. A. Henson, M. L. Smith, R. Coppola, E. Bullmore, and D. Plenz, Neuronal Avalanches in the Resting MEG of the Human Brain, *J. Neurosci.* **33**, 7079 (2013).
- [144] G. Scott, E. D. Fagerholm, H. Mutoh, R. Leech, D. J. Sharp, W. L. Shew, and T. Knöpfel, Voltage imaging of waking mouse cortex reveals emergence of critical neuronal dynamics, *J. Neurosci.* **34**, 16611 (2014).
- [145] E. Tagliazucchi, P. Balenzuela, D. Fraiman, and D. R. Chialvo, Criticality in large-scale brain fMRI dynamics unveiled by a novel point process analysis, *Front. Physiol.* **3 FEB**, 15 (2012).
- [146] T. Petermann, T. C. Thiagarajan, M. A. Lebedev, M. A. Nicolelis, D. R. Chialvo, and

- D. Plenz, Spontaneous cortical activity in awake monkeys composed of neuronal avalanches., Proc. Natl. Acad. Sci. U. S. A. **106**, 15921 (2009).
- [147] A. McWhorter, 1/f noise and related surface effects in germanium., in *Semicond. Surf. Phys.* (MIT Lincoln Laboratory, 1957) pp. 207–228.
- [148] A. M. Bastos, W. M. Usrey, R. A. Adams, G. R. Mangun, P. Fries, and K. J. Friston, Canonical Microcircuits for Predictive Coding (2012).
- [149] C. V. Stewart and D. Plenz, Inverted-U profile of dopamine-NMDA-mediated spontaneous avalanche recurrence in superficial layers of rat prefrontal cortex, J. Neurosci. **26**, 8148 (2006).
- [150] R. Srinivasan, D. P. Russell, G. M. Edelman, and G. Tononi, Increased synchronization of neuromagnetic responses during conscious perception, J. Neurosci. **19**, 5435 (1999).
- [151] D. A. Blythe and V. V. Nikulin, Long-range temporal correlations in neural narrowband time-series arise due to critical dynamics, PLoS One **12**, e0175628 (2017).
- [152] S. Zapperi, K. B. Lauritsen, and H. E. Stanley, Self-organized branching processes: Mean-field theory for avalanches, Phys. Rev. Lett. **75**, 4071 (1995), arXiv:9509161 [cond-mat].
- [153] M. C. Kuntz and J. P. Sethna, Noise in disordered systems: The power spectrum and dynamic exponents in avalanche models, Phys. Rev. B - Condens. Matter Mater. Phys. **62**, 11699 (2000), arXiv:9911207 [cond-mat].
- [154] M. A. Muñoz, R. Dickman, A. Vespignani, and S. Zapperi, Avalanche and spreading exponents in systems with absorbing states, Phys. Rev. E - Stat. Physics, Plasmas, Fluids, Relat. Interdiscip. Top. **59**, 6175 (1999), arXiv:9811287 [cond-mat].
- [155] D. Plenz and T. C. Thiagarajan, The organizing principles of neuronal avalanches: cell assemblies in the cortex?, Trends Neurosci. **30**, 101 (2007).
- [156] J. I. Gold and M. N. Shadlen, The Neural Basis of Decision Making, Annu. Rev. Neurosci. **30**, 535 (2007).
- [157] R. L. Cowan and C. J. Wilson, Spontaneous firing patterns and axonal projections of single corticostriatal neurons in the rat medial agranular cortex, J. Neurophysiol. **71**, 17 (1994).
- [158] C. J. Wilson and Y. Kawaguchi, The origins of two-state spontaneous membrane potential fluctuations of neostriatal spiny neurons, J. Neurosci. **16**, 2397 (1996).
- [159] D. Paré, E. Shink, H. Gaudreau, A. Destexhe, and E. J. Lang, Impact of spontaneous synaptic activity on the resting properties of cat neocortical pyramidal neurons in vivo, J. Neurophysiol. **79**, 1450 (1998).

- [160] R. Cossart, D. Aronov, and R. Yuste, Attractor dynamics of network UP states in the neocortex, *Nature* **423**, 283 (2003).
- [161] C. Wilson, Up and down states, *Scholarpedia* **3**, 1410 (2008).
- [162] F. Lombardi, H. J. Herrmann, C. Perrone-Capano, D. Plenz, and L. De Arcangelis, Balance between excitation and inhibition controls the temporal organization of neuronal avalanches, *Phys. Rev. Lett.* **108**, 228703 (2012).
- [163] F. Freyer, J. A. Roberts, R. Becker, P. A. Robinson, P. Ritter, and M. Breakspear, Biophysical mechanisms of multistability in resting-state cortical rhythms, *J. Neurosci.* **31**, 6353 (2011).
- [164] B. B. Mandelbrot, Intermittent turbulence in self-similar cascades: Divergence of high moments and dimension of the carrier, *J. Fluid Mech.* **62**, 331 (1974).
- [165] E. A. Ihlen and B. Vereijken, Interaction-dominant dynamics in human cognition: Beyond 1/f fluctuation, *J. Exp. Psychol. Gen.* **139**, 436 (2010).
- [166] K. J. Friston, Another neural code?, *Neuroimage* **5**, 213 (1997).
- [167] M. Rabinovich, R. Huerta, and G. Laurent, Transient Dynamics for Neural Processing, *Science (80-.)*. **321**, 48 (2008).
- [168] F. J. Varela, The specious present: A neurophenomenology of time consciousness, *Nat. Phenomenol. Issues Contemp. Phenomenol. Cogn. Sci.* **LXIV**, 266 (1999).
- [169] D. M. Eagleman and T. J. Sejnowski, Motion Integration and Postdiction in Visual Awareness, *Science (80-.)*. **287**, 2036 (2000).
- [170] M. H. Herzog, T. Kammer, and F. Scharnowski, Time Slices: What Is the Duration of a Percept?, *PLoS Biol* **14**, e1002433+ (2016).
- [171] D. M. Wolpert and M. Kawato, Multiple paired forward and inverse models for motor control., *Neural Networks* **11**, 1317 (1998).
- [172] D. M. Wolpert, S. J. Goodbody, and M. Husain, Maintaining internal representations: the role of the human superior parietal lobe, *Nat. Neurosci.* **1**, 529 (1998).
- [173] R. Leech, R. Braga, and D. J. Sharp, Echoes of the brain within the posterior cingulate cortex, *J. Neurosci.* **32**, 215 (2012).
- [174] B. Biswal, F. Zerrin Yetkin, V. M. Haughton, and J. S. Hyde, Functional connectivity in the motor cortex of resting human brain using echo-planar mri, *Magn. Reson. Med.* **34**, 537 (1995).
- [175] S. Achard, R. Salvador, B. Whitcher, J. Suckling, and E. Bullmore, A resilient, low-frequency,

- small-world human brain functional network with highly connected association cortical hubs., J. Neurosci. **26**, 63 (2006).
- [176] M. D. Fox and M. E. Raichle, Spontaneous fluctuations in brain activity observed with functional magnetic resonance imaging, Nat Rev Neurosci **8**, 700 (2007).
- [177] A. Haimovici, E. Tagliazucchi, P. Balenzuela, and D. R. Chialvo, Brain organization into resting state networks emerges at criticality on a model of the human connectome, Phys. Rev. Lett. **110**, 178101 (2013), arXiv:1209.5353.
- [178] L. L. Gollo, A. Zalesky, R. Matthew Hutchison, M. Van Den Heuvel, and M. Breakspear, Dwelling quietly in the rich club: Brain network determinants of slow cortical fluctuations, Philos. Trans. R. Soc. B Biol. Sci. **370**, 10.1098/rstb.2014.0165 (2015).
- [179] Alternatively to A2, f_{A_i} can be calculated as $f_{A_i} = B_{\theta_i}[f_{\tilde{A}_i}]q_i^{(0)} + (1 - q_i^{(0)})(B_{\theta_i}[f_{\tilde{A}_i^{(1)}}]q_i^{(1)} + (1 - q_i^{(1)})(\dots))$, with $f_{\tilde{A}_i^{(t)}} = B_{\theta_i}[f_{\tilde{A}_i^{(t-1)}}] * I$, $f_{\tilde{A}_i^{(0)}} = f_{\mathcal{E}_{i-1}}$, and $f_{\tilde{A}_i^{(0)}} = I$.
- [180] L. Pietronero, A. Erzan, and C. Evertsz, Theory of Laplacian fractals: Diffusion limited aggregation and dielectric breakdown model, Phys. A Stat. Mech. its Appl. **151**, 207 (1988).
- [181] R. B. Stein, A Theoretical Analysis of Neuronal Variability, Biophys. J. **5**, 173 (1965).
- [182] S. Ditlevsen and P. Lansky, Estimation of the input parameters in the Ornstein-Uhlenbeck neuronal model, Phys. Rev. E. Stat. Nonlin. Soft Matter Phys. **71**, 10.1103/PHYSREVE.71.011907 (2005).
- [183] D. Sornette, F. Deschâtres, T. Gilbert, and Y. Ageon, Endogenous Versus Exogenous Shocks in Complex Networks: An Empirical Test Using Book Sale Rankings, Phys. Rev. Lett. **93**, 228701 (2004).
- [184] H. M. Taylor and S. Karlin, *An Introduction to Stochastic Modeling, 3rd ed.* (Academic Press Limited, 1998).
- [185] Notice this implies that for fixed t , the distribution of RBM coincides with the running maximum distribution for Brownian motion $f_{|B^{(t)}|}(x) = f_{\max_{0 \leq u \leq t} W^{(u)}}(x)$.
- [186] This is a common procedure in finance for pricing double barrier options.
- [187] O. Faulhaber, Analytic methods for pricing double barrier options in the presence of stochastic volatility (2002).
- [188] A. I. Markushevich, *Theory of analytic functions* (1950).
- [189] R. H. Shumway and D. S. Stoffer, *Time Series Analysis and Its Applications: With R Examples (Springer Texts in Statistics)*, 2nd ed. (Springer, 2006).

- [190] The expected mean $\langle \theta^{(t+n)} | \theta^{(t)} \rangle$ and variance $\text{var}(\theta^{(t+n)} | \theta^{(t)})$ after n iterations can be derived explicitly by iterated application of Eq. C1 $\langle \theta^{(t+n)} | \theta^{(t)} \rangle = \langle \Theta \rangle (1 - (1 - w)^n) + \theta^{(t)} (1 - w)^n$ and $\text{var}(\theta^{(t+n)} | \theta^{(t)}) \approx (1 - (1 - w)^{2n}) \frac{w}{2} \text{var} |\tilde{a}^{(t)}|$.
- [191] Specifically, the non-unitary Fourier transform, in ordinary frequency units.
- [192] Cf. variance of pulses $\sigma_{\mathcal{E}} = 0.35 \langle \Theta_l \rangle$.
- [193] D. B. Percival, Spectral Analysis of Univariate and Bivariate Time Series, in *Methods Exp. Phys.*, Vol. 28 (Academic Press, 1994) pp. 313–348.
- [194] M. R. Evans and S. N. Majumdar, Diffusion with stochastic resetting, *Phys. Rev. Lett.* **106**, 160601 (2011), arXiv:1102.2704.
- [195] S. N. Majumdar and G. Oshanin, Spectral content of fractional Brownian motion with stochastic reset, *J. Phys. A Math. Theor.* **51**, 435001 (2018).
- [196] S. Coles, *An Introduction to Statistical Modeling of Extreme Values*, Springer Series in Statistics (Springer London, London, 2001).
- [197] J. M. Ginoux and C. Letellier, Van der Pol and the history of relaxation oscillations: Toward the emergence of a concept, *Chaos* **22**, 023120 (2012), arXiv:1408.4890.
- [198] R. Efron, The relationship between the duration of a stimulus and the duration of a perception, *Neuropsychologia* **8**, 37 (1970).
- [199] D. Burr, Motion smear, *Nature* **284**, 164 (1980).